

FRINGE PROJECTION IN THE DYNAMIC TESTING OF COMPOSITE MATERIALS

By

Daniel Connell Schleh

A THESIS

Submitted to

Michigan State University

In partial fulfillment of the requirements

for the degree of

Mechanical Engineering – Master of Science

2013

## **ABSTRACT**

### **FRINGE PROJECTION IN THE DYNAMIC TESTING OF COMPOSITE MATERIALS**

By

Daniel Connell Schleh

Understanding the response of composite materials subject to dynamic loading conditions is necessary for their safe and efficient application to many of the world's engineering problems where strength-to-weight ratios are vitally important. To examine the response of composite materials subject to dynamic out-of-plane impacts, an optical technique known as fringe projection was used to measure the resulting out-of-plane displacement from drop weight impact tower testing and horizontal impact testing using a gas accelerated projectile. The velocity histories as well as the strain rates can be identified through consideration of the measured displacement histories. The associated acceleration histories, force histories, and impact based bending stiffness can also be calculated, but achieving consistent and logical results for those parameters demonstrated a greater dependence on data resolution.

To ensure test results gained from small specimens can be applied to large ones, consideration of potential size effects is required. Scaling factors of three, five and ten were used to scale composite materials subject to horizontal impact from scaled gas accelerated projectiles. The whole-field out-of-plane displacement histories of the non-impact surface of the test specimens were captured using fringe projection. Through consideration of the displacement histories at the point of impact on the non-impact surface, readjusted for scale, a size effect was not observed for displacement within the elastic region. Scaling was unable to account for the damage modes in test specimens across scales. The damage modes present and the delamination area in the test specimens were more advanced in larger specimens.

## **ACKNOWLEDGEMENTS**

I would like to thank my advisor Professor Dahsin Liu for his oversight, numerous contributions and providing a means for this work to occur. I would also like to extend my thanks to Dr. Guojing Li for his expertise and aide in making things happen. I am also grateful to Professor Al Loos and Professor Patrick Kwon for serving on my committee. Finally, the financial aspect for this work was supported by the Army Research Lab and is sincerely appreciated.

## TABLE OF CONTENTS

LIST OF TABLES .....	vi
LIST OF FIGURES .....	viii
KEY TO SYMBOLS AND ABBREVIATIONS .....	x
Organizational Overview .....	1
Section 1: Fringe Projection in the Dynamic Testing of Composites.....	2
Abstract .....	2
1. Importance of Out-of-Plane Deformation measurements .....	2
2. Out-of-Plane Deformation Measurements .....	3
2.1 Out-of-Plane Deformation Measurements.....	3
2.2 Reflection Moiré.....	4
2.3 Shadow Moiré.....	5
2.4 Projection Moiré.....	6
2.5 Fringe Projection .....	7
2.6 Moiré and Fringe Method Comparison .....	7
2.7 Objective of Out-of-Plane Deformation Measurements.....	8
3. Fringe Projection.....	9
3.1 Fringe Projection .....	9
3.2 Computing Out-of-Plane Deformation from Fringe Projection .....	12
3.3 Fringe Projection Calibration .....	14
4. Fringe Projection Applied to DWIT.....	15
4.1 Fringe Projection Applied to DWIT .....	15
4.2 DWIT Calibration.....	17
4.3 DWIT Data Processing.....	20
4.4 DWIT Results .....	21
5. Fringe Projection Applied to the Gas Assisted Horizontal Impactor (GAHI) .....	25
5.1. Fringe Projection Applied to the Gas Assisted Horizontal Impactor (GAHI) .....	25
5.2 Accuracy of Fringe Projection Applied to the GAHI.....	28
5.3 GAHI Test Results.....	30
5.4 Double Peak Investigation.....	31
5.5 Fringe Projection Lighting.....	36
6. Conclusion.....	38
APPENDICES .....	40
Appendix A: GAHI Experimentation Procedural Information .....	41
Appendix B: Accuracy and Frame Rate .....	44
REFERENCES.....	47

Section 2: Scaling of Composite Materials Subject to Horizontal Impact .....	50
Abstract .....	50
1. Introduction .....	51
2. Scaling.....	52
2.1 Scaling Relations .....	52
2.2 Scaling Limitations.....	55
3. Experimental Techniques.....	56
4. Experimental Results.....	60
4.1 Displacement Histories.....	60
4.2 Damage Modes .....	64
4.3 Strain Rates.....	65
4.4 Impact Based Bending Stiffness.....	68
5. Discussions.....	68
5.1 Pi Terms.....	68
5.2 Overall Displacement Histories.....	70
5.3 Evaluation of the Projectile Loading Sequence Data .....	73
5.4 Scaling of Force Displacement Relations.....	77
5.5 Damage.....	79
6. Conclusion.....	80
APPENDICIES .....	82
Appendix C: Buckingham Pi Scaling.....	83
Appendix D: Fringe Projection and Strain Rate Evaluation.....	87
REFERENCES.....	90

Section 3: Evaluation of the Impact Based Bending Stiffness from Fringe Projection Applied to the GAHI.....	93
Abstract .....	93
1. Introduction .....	93
2. Drop Weight Impact Tower (DWIT) Test Data.....	94
2.1 Drop Weight Impact Tower (DWIT) Test Data .....	94
2.2 Load Cell Impact Based Bending Stiffness.....	94
2.3 Fringe Projection Impact Based Bending Stiffness.....	94
3. Gas Assisted Horizontal Impactor (GAHI) Test Data .....	96
3.1 Gas Assisted Horizontal Impactor (GAHI) Test Data.....	96
3.2 Finite Difference.....	97
3.3 Curve Fitting.....	97
3.4 Curve Fitting with Third Order Polynomials .....	99
3.5 Consistency with the Application of Curve Fitting (Methods A, B and C) .....	103
3.6 Curve Fitting Third Order Polynomials: Method D .....	106
4. Conclusion.....	111

## LIST OF TABLES

Table 1. Measurements of object using fringe projection in the DWIT setup.....	19
Table 2. Deviation in peak displacement.....	21
Table 3. Test condition correlation with optical parameters.....	28
Table 4. Accuracy Measurements and Quantification.....	29
Table 5. Accuracy Measurements for Configuration A* (Spatial Res~3.47 pixels/mm,K~0.49). .....	44
Table 6. Accuracy Measurements for Configuration B* (Spatial Res~3.57 pixels/mm,K~0.486). .....	45
Table 7. Accuracy Measurements for Configuration C* (Spatial Res~3.67 pixels/mm,K~0.55).	46
Table 8. Important scaling parameters and their associated scaling.....	54
Table 9. Scaled test parameters and associated testing information.....	58
Table 10. Accuracy measurements and quantification for the three GAHI testing configurations of Table 9.....	59
Table 11. Damage modes in test specimens.....	64
Table 12. Delamination area (cm <sup>2</sup> ) and the ratio of the delamination areas across scales.....	65
Table 13. Strain rates of the composite plates as obtained by fringe projection without and with an attempted account for scale.....	67
Table 14. Scaled impact based bending stiffness (kN/mm) values.....	68
Table 15. Computation of Pi-Terms across scales associated with 65 m/s projectile impacts.....	69
Table 16. Additional testing information for the three sizes of specimens.....	89
Table 17. Impact based bending stiffness (kN/mm) from DWIT Testing.....	96

Table 18. Velocity, acceleration, and force data calculated using the finite difference method for a 50 m/s impact on a 5 ply specimen. ....	97
Table 19. Impact based bending stiffness (IBBS) values from GAHI test results using curve fit second order trigonometric polynomials. ....	98
Table 20. Description of the points included from the displacement histories when generating a curve-fit polynomial.....	100
Table 21. Initial velocities ( $V_o$ (m/s)) and the impact based bending stiffness (IBBS(kN/mm)) resulting from curve fitting of the raw displacement histories for 5 ply GAHI tests. ....	101
Table 22. Initial Velocities ( $V_o$ (m/s)) and the impact based bending stiffness (IBBS(kN/mm)) resulting from curve fitting of curve fit displacement histories for 5 ply GAHI tests.....	102
Table 23. Initial velocities ( $V_o$ (m/s)) and the impact based bending stiffness (IBBS(kN/mm)) resulting from curve fitting of curve fit displacement histories for testing conducted with 5ply specimens.....	103
Table 24. Percentage variation in magnitude of select points between Tests 1 and 2 of Figure 24. ....	104
Table 25. Impact based bending stiffness (kN/mm) for two 50 m/s impacts of 5 ply specimens. ....	105
Table 26. Percentage variation in magnitude of select points between Tests 1 and 2 of Figure 22. ....	106
Table 27. Impact based bending stiffness (kN/mm) for two 65 m/s impacts of 5 ply specimens. ....	106
Table 28. Impact based bending stiffness values from 3 ply GAHI test specimens.....	108
Table 29. Impact based bending stiffness values from 5 ply GAHI test specimens.....	108
Table 30. Impact based bending stiffness values from 10 ply GAHI test specimens.....	108
Table 31. Unscaled Impact based bending stiffness (kN/mm) from GAHI Testing. ....	109

## LIST OF FIGURES

Figure 1. A generalized depiction of a reflection moiré setup. (For interpretation of the references to the color in this and all other figures, the reader is referred to the electronic version of this thesis.) .....	5
Figure 2. A generalized depiction of the components involved in a shadow moiré setup. ....	6
Figure 3. A generalized depiction of a projection moiré experimental setup.....	7
Figure 4. A general depiction of the projected fringes interacting with the surface of interest. The parameters defined are (1) $\theta$ , the angle between the projection and viewing axes, (2) $p$ , pitch of projected fringes (3) $d$ , fringe spacing as perceived along the viewing axis and(4) $C$ , contour fringe interval.....	11
Figure 5. Viewed from the side, a schematic the DWIT specimen fixture and impactor with projection moiré incorporated. Note: Figure 5 not drawn to scale. ....	16
Figure 6. Reference plane and cone images with projected fringes while resting on the circular boundaries of the DWIT fixture.....	18
Figure 7. The contour plot showing the results of the calibration procedure with profiles across the peak of the cone displayed as well.....	18
Figure 8. Displacement histories from a DWIT test gathered from numerical integrations of load cell data and fringe projection. The impactor mass of 5.01 kg was released from a height of 152.4 mm (6”) above the 75.6 mm (3”) diameter specimen with clamped boundaries. The test specimen was a composite composed of 3 plies of woven E-glass fibers with a SC-15 matrix. The thickness of the specimen was 2.01 mm (0.079”). .....	22
Figure 9. A plot of the percentage difference between load cell and fringe projection peak displacements as a function of specimen thickness. ....	24
Figure 10. Viewed from above, schematic of the GAHI to which fringe projection was applied. ....	26
Figure 11. Displacement histories for the impact point from GAHI testing using GAHI Test Configuration B with specimens made of woven E-glass fibers and a SC-15 matrix.....	31

Figure 12. Fringe projection displacement history (bottom) correlated with the high-speed video of the projectile striking the impact surface and the horizontal displacement profiles (top). The case documented is for Configuration B of Table 3 with the projectile striking a composite plate at 80 m/s composed of woven E-glass fibers with a SC-15 matrix. ....	32
Figure 13. Extended deformation history for the 80 m/s test case featured in Figures 11 and 12.. .....	35
Figure 14. Image of the GAHI experimental setup.....	57
Figure 15. Unscaled displacement histories from 65 m/s projectile impacts for $\lambda = 3, 5,$ and $10$ .. .....	60
Figure 16. Scaled displacement histories for 65 m/s impact tests. ....	62
Figure 18. Strain rates as a function of gage length for the $\lambda = 10$ test cases. ....	67
Figure 19. Scaled displacement, velocity, and force histories up to the initial peak displacement from 65 m/s tests.....	76
Figure 20. Scaled force displacement relations from 65 m/s tests.....	78
Figure 21. Enhanced image of the non-impact surface of a test specimen for the $\lambda = 10, 95$ m/s test configuration with fringes captured at 0.038 ms into the impact event. ....	87
Figure 22. Out-of-plane displacement as a function of position across the specimen surface for the $\lambda = 10, 95$ m/s test configuration. ....	88
Figure 23. Abbreviated strain history for a $\lambda = 10, 95$ m/s impact test. ....	89
Figure 24. Displacement histories from two GAHI tests at 50 m/s involving the 0.25” projectile and 5 ply specimens. ....	104
Figure 25. Displacement histories from two GAHI tests at 65 m/s involving the 0.25” projectile and 5 ply specimens. ....	105

## KEY TO SYMBOLS AND ABBREVIATIONS

$\theta$  = angle between viewing and projection axis

$\lambda$  = scale factor

$\rho$  = density of the specimen

$\rho_{imp}$  = density of the impactor

$\nu$  = Poisson's ratio of the test specimen

$\nu_{imp}$  = Poisson's ratio of the impactor

$\Phi^*$  = phase estimator

" = inches

C = contour interval

cm<sup>2</sup> = square centimeters

$d$  = fringe spacing as perceived along the viewing axis

dl = delamination

$D_{imp}$  = impactor diameter

DWIT = drop weight impact tower

$E$  = Young's modulus

$E_{imp}$  = Young's modulus of the impactor

$f_0$  = carrier frequency

FP = fringe projection

fps = frames per second

GAHI = gas assisted horizontal impactor

h = specimen thickness

imc = internal matrix cracking

ismc = impact surface matrix cracking

isfb = impact surface fiber breakage

$k$  = calibration constant

kg = kilogram

kN = kilonewton

$l$  = specimen length

m = meters

s = seconds

mm = millimeter

IBBS = Impact based bending stiffness

ms = millisecond

nsmc = non-impact surface matrix cracking

nsfb = non-impact surface fiber breakage

$p$  = fringe pitch

$\pi_x$  = the  $x$ th pi term

$V_{imp}$  = velocity of the impactor/projectile

$V_o$  = velocity of the impactor/projectile

$t$  = time

$w$  = specimen width

$z$  = out-of-plane displacement

## **Organizational Overview**

This thesis pertains to the measurement of out-of-plane deformation of composite materials subject to loads from the out-of-plane direction using fringe projection.

In Section 1, several techniques to measure out-of-plane displacement using a single point of view are discussed. Fringe projection is then introduced and its function as well as its general application is explained. Moving to specific applications, fringe projection is applied to a drop weight impact tower (DWIT). The load cell of the DWIT is used to validate and understand the use of fringe projection in dynamic testing. Finally in Section 1, the application of fringe projection to the gas assisted horizontal impactor (GAHI) is presented with sample results.

The focus of Section 2 is on experimentally testing the scalability of composite materials using the GAHI in conjunction with fringe projection. A review of the literature is presented with a scaling scheme and it is applied to the GAHI setup and woven fiber reinforced composite specimens. Testing is conducted to evaluate the presence of size effects. Experimental results are provided and analyzed in the form of displacement histories and damage. Strain rate data is also featured as well as impact based bending stiffness values, despite inconsistencies in the data of the later.

The final section is focused on the evaluation of the impact based bending stiffness values of Section 2, which were derived from the displacement histories that are the direct output of the fringe projection method. The impact based bending stiffness provides a means of characterizing the elastic response of the test specimen albeit a geometrically dependent one. Thus the ability to generate impact based bending stiffness values from a measurement method applicable to rates of loading beyond what a DWIT can provide would be advantageous. Methodologies attempted to calculate consistent impact based bending stiffness values are presented with little success.

## **Section 1: Fringe Projection in the Dynamic Testing of Composites**

### **Abstract**

To examine the response of composite materials subject to dynamic out-of-plane impacts, an optical technique known as fringe projection was used to measure the resulting out-of-plane displacement. Fringe projection was used to measure out-of-plane deformation from drop weight impact tower (DWIT) testing and the results were compared to the displacement history generated from the load cell of the DWIT. Fringe projection was then used and evaluated as means to measure the out-of-plane displacement from projectile impact loading involving a projectile accelerated horizontally through the use of gas. Fringe projection is capable of providing out-of-plane deformation measurements for horizontal impacts which are commonly performed without any measurement other than projectile velocity. However, the duration and energy of the impact events to which fringe projection can be applied is not without limits.

### **1. Importance of Out-of-Plane Deformation measurements**

One prong on the multi-tiered continuous movement to develop more advanced and efficient technologies is that of materials. The development of advanced materials has always played a vital role to technological advancement and the development of materials for use in mobile technologies is no different. Composite materials are most widely known for their use in aerospace structures; structures where strength-to-weight ratios are vital. Composites are becoming an increasing popular consideration for applications beyond aerospace structures such as ground vehicle structures, marine vehicle structures and personal protection kits. In many of the aforementioned cases composite materials are being considered for use as the primary structural component. Given that composites have been and will be continued to be integrated

into mobile apparatuses that are used in military and civilian applications, accurate characterization of the materials under a variety of loading conditions becomes an even more pressing endeavor. Since vehicles are one of the primary applications of composite materials, it is reasonable to expect that the loading conditions to which they are subject are and will be highly dynamic. As the material composing the body of a vehicle, a common loading scenario would include an impact from the out-of-plane direction to the composite surface. This out-of-plane impact could occur across a vast span of loading rates. The behavior of certain composite materials has previously demonstrated a dependence on the loading rate [1]. The reaction of composites subject to various rates of out-of-plane loading needs to be carefully considered for the continued integration of composite materials into ever more advanced applications.

## **2. Out-of-Plane Deformation Measurements**

### **2.1 Out-of-Plane Deformation Measurements**

The characterization process of composite materials subject to out-of-plane loadings requires methods for quantifying the composite response. DWITs have been used for low-velocity out-of-plane impact on composites [2]. DWITs best simulate accidental impacts on composite structures due to gravity. Many DWITs consist of a mass that is free to fall with the constriction of guide rails. An impactor usually leads the mass into the specimen at impact. A load cell attached to the impactor allows for the measurement of the force history at the point of impact. A velocity flag is also a mainstay on DWITs as it allows for the measurement of the velocity of the mass immediately prior to impact. The displacement history can then be computed at the point of impact throughout the duration of the impact event. DWITs offer a

good start for characterizing composites subject to low-velocity impacts as strain gage based load cells provide a relatively direct means of measurement.

Composites need to be evaluated at loading rates beyond those a DWIT can provide. To do this, additional experimental setups will be required along with a means of dynamic measurement that can capture high rates of out-of-plane loadings. An experimental means considered to capture out-of-plane displacement for dynamic experimental setups involve the use of high-speed photography. Moiré and fringe methods have been used in static and dynamic applications to collect contour information in a vast array of fields including aerospace [3, 4], health sciences [5, 6], and MEMS [7]. Moiré and fringe analysis methods used include reflection moiré, shadow moiré, projection moiré, and fringe projection.

## **2.2 Reflection Moiré**

Reflection moiré [8, 9] outputs out-of-plane slope information without the need for differentiation; a unique feature among the moiré and fringe methods. The moiré in the reflection moiré technique is generated through the superimposition of gratings reflected from the mirror-like surface finish of the specimen at differing stages of specimen deformation. A considerable limitation of reflection moiré is the requirement on the surface finish of the object of interest. Figure 1 provides a description of the configuration of components in reflection moiré.

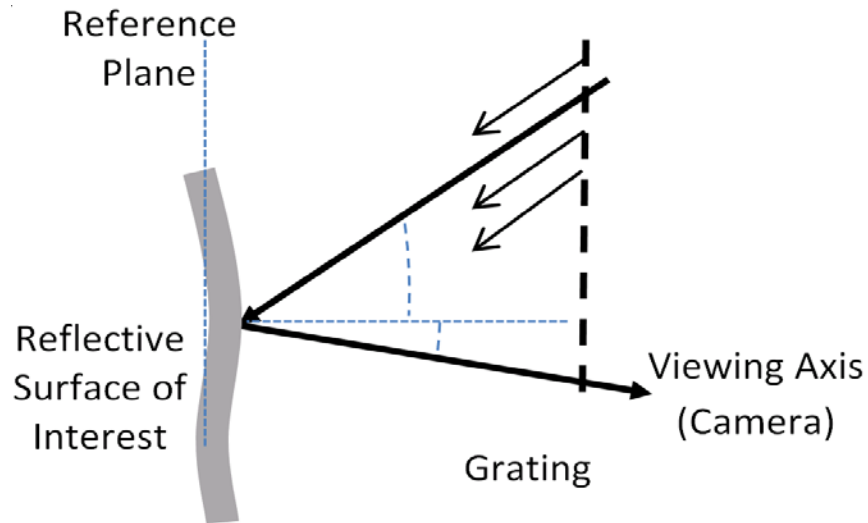


Figure 1. A generalized depiction of a reflection moiré setup. (For interpretation of the references to the color in this and all other figures, the reader is referred to the electronic version of this thesis.)

### 2.3 Shadow Moiré

Shadow moiré [5, 8, 9] involves the placement of a single master grating near the surface of an object of interest (Figure 2). The setup is illuminated obliquely, which casts a shadow from the grating immediately in front of the object of interest. Viewing the setup from a position away from the light source reveals a moiré pattern created from the actual master grating and the shadow cast from the obliquely placed light source.

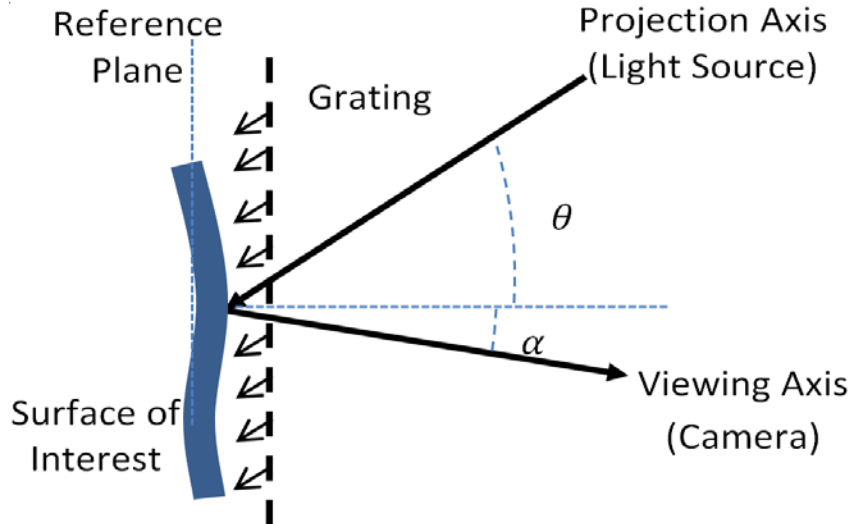


Figure 2. A generalized depiction of the components involved in a shadow moiré setup.

## 2.4 Projection Moiré

A method that is very similar to shadow moiré is projection moiré [10]. Two configurations exist for projection moiré. In one, two gratings are used, one is placed in front of the light source and the other is placed directly in front of the camera used to capture images of the setup (Figure 3). The grating placed in front of the light source casts fringes onto the object of interest. The grating placed directly in front of the camera serves to physically create the interference fringes that compose a moiré pattern used for analysis. In the second configuration, a grating is only placed in front of the light source and the fringes are cast upon the object of interest. The camera, without a grating located in front of it, captures images of a reference plane with fringes and an object of interest with fringes cast over its surface. The images are then digitally superimposed over one another to generate a moiré pattern that reveals contour information.

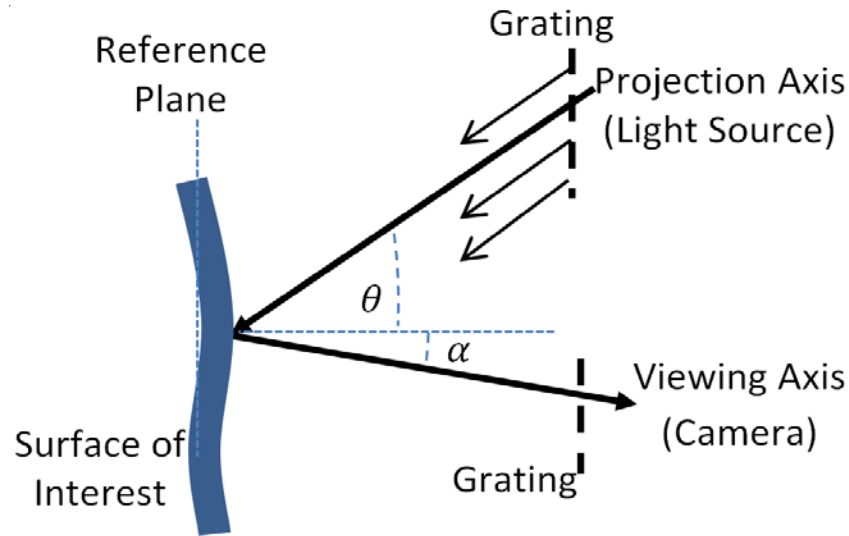


Figure 3. A generalized depiction of a projection moiré experimental setup.

## 2.5 Fringe Projection

The experimental setup for fringe projection is very much like the setup for projection moiré with a single grating [10]. In fringe projection, a single grating is placed directly in front of a dedicated light source. The dedicated light source then projects fringes onto an object of interest. A camera, positioned elsewhere from the dedicated light source captures images of fringes cast onto a reference plane and an object of interest. This is identical to the projection moiré technique where a single grating is used. Processing of the digitized images in fringe projection examines the deviation from straight lines by the fringes in the images of the object of interest to determine shape information [11]. With projection moiré, a moiré pattern is used to arrive at the shape information.

## 2.6 Moiré and Fringe Method Comparison

Reflection moiré is limited in its applications due to the surface finish requirements. Shadow moiré offers a method for contour measurement using a relatively coarse grating, but the grating must be constructed very near the specimen surface to reduce diffraction and penumbra

effects [12]. Shadow moiré also necessitates that the grating be the size of the object for the collection of contour information across the specimen surface [13]. This does negatively affect the usefulness of the method when working with a range of specimen geometries and experimental setups. Projection moiré and shadow moiré share similar modes of operation (contour information from moirés) and sensitivity limits of approximately 0.1 mm [12]. Projection moiré requires a finer grating than shadow moiré and it can be more challenging to achieve proper system alignment considering when two independent gratings are used to physically generate a moiré. Fringe projection can be a more congenial system to apply, but this comes with a loss in sensitivity. This is due to the lack of a moiré pattern in the physical system. When a moiré pattern is physically present, the camera used to record images must only be able to resolve the moiré fringes and thus finer gratings can be applied to the system resulting in higher sensitivities. When the moiré pattern is not physically present the camera must be capable of resolving the fringes alone. The moiré pattern also provides better sensitivity as moiré patterns shift more drastically in response to out-of-plane deformation as compared to fringes [10].

For this investigation into measuring deformation of composite materials subject to dynamic out-of-plane loadings, fringe projection was used due to the availability of processing software and the ease through which the method can be applied to specimens of varying geometry.

## **2.7 Objective of Out-of-Plane Deformation Measurements**

Measuring the out-of-plane displacement history for various loading rates is a beneficial step in characterization of composite materials. The moiré and fringe methods for gathering surface contour information are full-field methods which allow for the collection of out-of-plane

displacement histories across the spatial coordinates of composite materials. The displacement history of the impact point can prove beneficial in the validation of numerical simulations. Looking beyond the raw contour data set, that information can be analyzed and transformed into velocity, acceleration and force histories through a series of differentiations. Once the force history is attained, the impact-based bending stiffness of the particular specimen of interest can be calculated based upon the linear loading region of the subsequent force-displacement plot. The bending stiffness would in turn provide insight into the response of composites stemming from various rates of dynamic loading.

### **3. Fringe Projection**

#### **3.1 Fringe Projection**

The fringe projection technique is a rather adaptable means through which out-of-plane deformations can be measured. In order to extract meaningful information from the fringe projection technique a relationship between the geometric parameters of the optical setup and specimen deformation needs to be established. In the establishment of these relationships the infinite optics assumption is made. Loosely stated, the infinite optics assumption requires that distances between the pieces of the optical setup are large compared to the specimen and the expected deformation. This allows for the assumption to be made that light traveling between elements in the system is collimated, resulting in constant fringe spacing ( $p$ ). According to Breque and company [6], the specific criteria for application of the infinite optics assumption are:

- (1) The distance between the light source projecting the fringes and the reference plane is close to equal with the distance between the camera viewing position and the reference plane.
- (2) The plane containing the light source and the camera viewing position is parallel to the reference plane.
- (3) The magnitude of the out-of-plane deformation is small compared to the distance between the camera viewing position and the reference plane.
- (4) The size of the surface of interest is small when compared to the distance between the projection and camera viewing positions

In this study, the “small” mentioned in items (3) and (4) is taken to be a difference in the order of magnitude (10 times). Breque and company [6] report measurement errors to be within 1% if small is taken to be an order of two magnitudes (100 times). In place of the infinite optics assumption, a collimator may be used to ensure incoming light is parallel or the analysis for the determination of contour depth can be made without the infinite optics assumption [13].

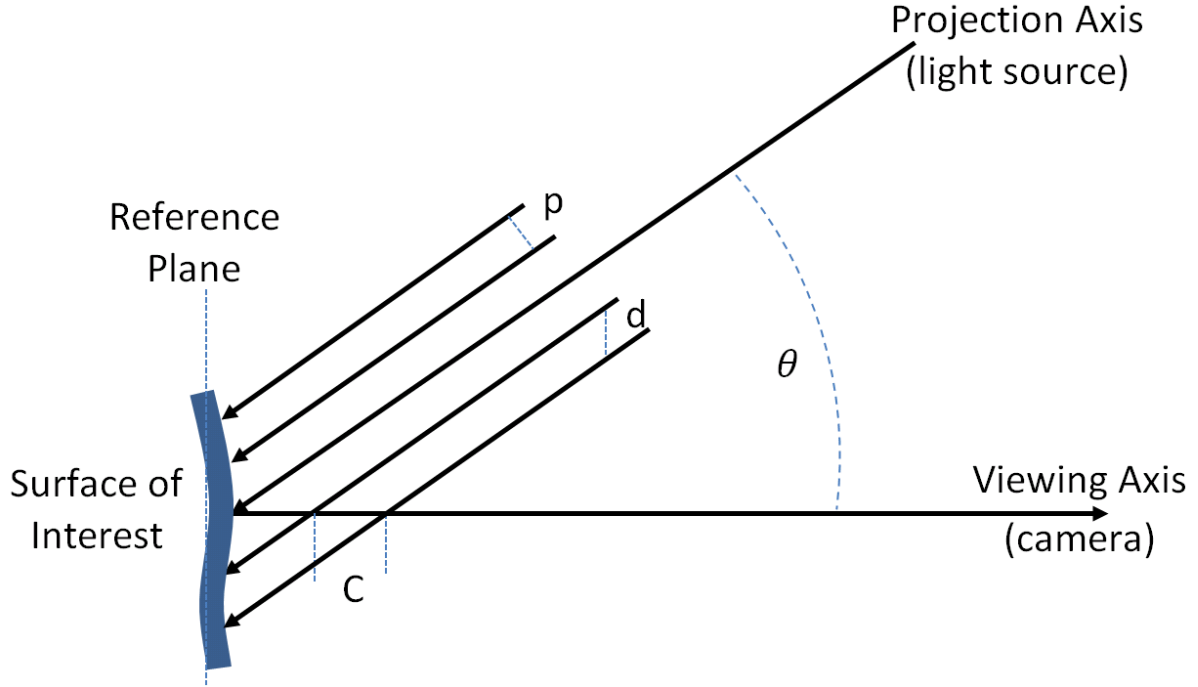


Figure 4. A general depiction of the projected fringes interacting with the surface of interest. The parameters defined are (1)  $\theta$ , the angle between the projection and viewing axes, (2)  $p$ , pitch of projected fringes (3)  $d$ , fringe spacing as perceived along the viewing axis and (4)  $C$ , contour fringe interval.

In Figure 4, the contour interval,  $C$ , is the distance between fringes along the viewing axis. Geometric analysis of a fringe projection setup can be used to relate  $C$  to the known  $p$ , pitch of the projected fringes,  $\theta$ , the angle between the projecting and viewing axes and  $d$ , the fringe spacing on the reference surface [14]. The viewing axis does not necessarily have to be normal to the reference surface, but a normal viewing perspective does make images more readily interpretable [10].

$$C = \frac{p}{\sin \theta} = \frac{d}{\tan \theta} \quad (1.1)$$

From Equation (1.1), it becomes evident that the sensitivity (which increases as values of  $C$  decrease) of an experimental setup can be increased by decreasing  $p$  through the use of a finer grating or increasing  $\theta$ . The value for  $\theta$  that will maximize the sensitivity of the setup is  $90^\circ$ .

Although a value of  $90^\circ$  for  $\theta$  would theoretically maximize sensitivity, practically this is not an ideal choice. A large angle between the viewing and projection axis would cast shadows across the surface of interest and leave regions lacking fringes and subsequently deformation information. The angle between the projection and viewing axis should not exceed the angles expected in the deformed surface of interest otherwise regions lacking fringes will be created. There are also very important practical limitations on the value of the fringe pitch. Theoretically the finer the grating, the higher the sensitivity of the system, but in practice, a low value for the fringe pitch does not equate to a better optical setup. The projected fringes must be resolvable by the camera used in the optical setup since too fine a grating will result in poor results due to the resolution limits of the camera in capturing images.

### **3.2 Computing Out-of-Plane Deformation from Fringe Projection**

In the testing performed, images of the surface of interest were captured by a high-speed camera throughout the impact process so that an out-of-plane displacement history could be recorded. This will generate a wealth of images that will require analysis. There are two general approaches to digital fringe pattern analysis, intensity and phase shift based. Intensity based methods measure fringe patterns based upon the intensity distribution alone. Intensity based methods are sensitive to noise and cannot distinguish between hills and valleys in contour data. Phase shift methods extract phase information from the intensity distribution. There are spatial and temporal phase shift methods. Spatial phase shift methods are particularly well suited for dynamics applications [10] as they allow for the collection of data from a single image where temporal phase shift methods require several images of static deformation for data collection.

An automated analysis process was adapted based upon the algorithm resulting from the work in Ref. [10] and applied through MATLAB. The fringe projection processing algorithms

are based upon a phase shifting method and assume an infinite optics experimental setup. The algorithm uses a reference and an object image to infer the deviation of the fringes from a straight line. In the reference image, the fringes are assumed to be vertically oriented. The intensity distribution of vertically oriented fringes is given by

$$I(i, j) = A(i, j) \left( 1 + \gamma(i, j) \cos(2\pi f_0 j + \Phi(i, j)) \right) \quad (1.2)$$

In Equation (1.2),  $A$  and  $\gamma$  serve as the background illumination and modulation terms,  $f_0$  as the carrier frequency, and  $\Phi$  represents the phase. Prior to the recent advances in computers and digitization of images, in order to determine depth information, several images of a surface of interest were required with the grating shifted by small, known amounts between images. Currently, this phase shifting can be performed digitally, thus allowing depth information to be extracted from a reference image and a single object of interest image. Five intensity terms are created through phase shifting of a single image. A phase estimator term  $\Phi^*$ , is generated from the five intensity terms for one image. The measured phase estimator term is proportional to the depth of the surface of interest. By subtracting the phase estimator terms from a surface of interest and a reference surface, changes in surface contour can be determined (Heredia-Ortiz and Patterson, [11]).

$$\Delta Z = \frac{(\Phi_{interst}^* - \Phi_{reference}^*)}{2\pi} * C = \Delta \Phi^* * K \quad (1.3)$$

From Equations (1.1) and (1.3), it is clear that  $C$  acts as constant proportionally factor. The calibration constant,  $K$  in Equation (1.3) includes the constants for quantifying  $\Delta Z$  for a given optical configuration.

The methodology for calculating contour information described above should also be considered when considering the geometry of a fringe projection setup. The algorithms work

well on smooth surfaces with small slopes (less variability in  $p$ ) when a fine grating is projected ( $p$  should be smaller than the features of interest) and when the angle between the projection and viewing axis is small. Values for  $\theta$  that have produced good results in previous work [7,11] were between 10 and 20°.

### **3.3 Fringe Projection Calibration**

A calibration procedure is required in the application of fringe projection using the algorithm developed by Heredia-Ortiz [10]. The calibration procedure serves to identify two primary parameters. The first is to identify the proportionality constant,  $K$ , from Equation (3). The second parameter is a magnification factor that becomes inherent in the optical setup as a result of the infinite optics assumption [11].

To perform the calibration, first, a flat reference surface is placed roughly at the depth from the viewing position that the object of interest would lay. Fringes are projected onto the reference surface and an image is captured. Secondly, a cone adhered to a flat surface is placed in lieu of the flat reference surface. The diameter and height of the cone are known. The size of the cone should be on the same order of magnitude as the expected height variations in the surface of interest. With respect to impact testing, the cone height should be slightly larger than the expected specimen surface deformation. Fringes are projected onto the cone and an image is captured. The flat reference surface and the cone are then processed through the calibration portion of the fringe projection algorithm to arrive at  $K$  and the magnification factor for the setup.

## **4. Fringe Projection Applied to DWIT**

### **4.1 Fringe Projection Applied to DWIT**

Fringe projection was first applied to relatively low-velocity dynamic impact events. This was accomplished by integrating the fringe projection setup with a DWIT as seen in Figure 2. DWITs are used for low-speed impact events as they use gravity to accelerate a mass. For this investigation, a Dynatup 8250 DWIT was used to impact circularly clamped 76.2 mm (3") diameter specimens with a 12.7 mm (0.5") diameter hemispherical impactor. A strain gage based load cell connected to the impactor provided a load history for the impact event. A dedicated 270 watt halogen light source was used to project fringes from a 20 lines/mm Ronchi ruling through a 12.5-75 mm zoom TV lens and onto the non-impact surface of the specimen secured in the DWIT through the use of a mirror placed beneath the specimen. A Vision Research Phantom v12.1 high-speed camera was used to record images during the impact event. The camera was equipped with a Carl Zeiss Planar T\* 1.4/85 mm ZF.2 lens. The high speed camera observed the non-impact surface of the specimen through the use of a second mirror placed at a 45° angle beneath the DWIT specimen. This resulted in the viewing axis of the camera being normal to the non-impact surface of the specimen. Frame rates applied to the DWIT that have yielded sufficient data range from 7,000 to 25,000 fps. The duration the impactor is in contact with the composite specimens typical used was between 7-12 ms. The majority of DWIT testing was conducted at a frame rate of 15,000 fps for drop heights ranging from 1-18". The number of images documenting the initial loading and unloading of a specimen was typically around 150. A depiction of the DWIT with fringe projection can be seen in Figure 5.

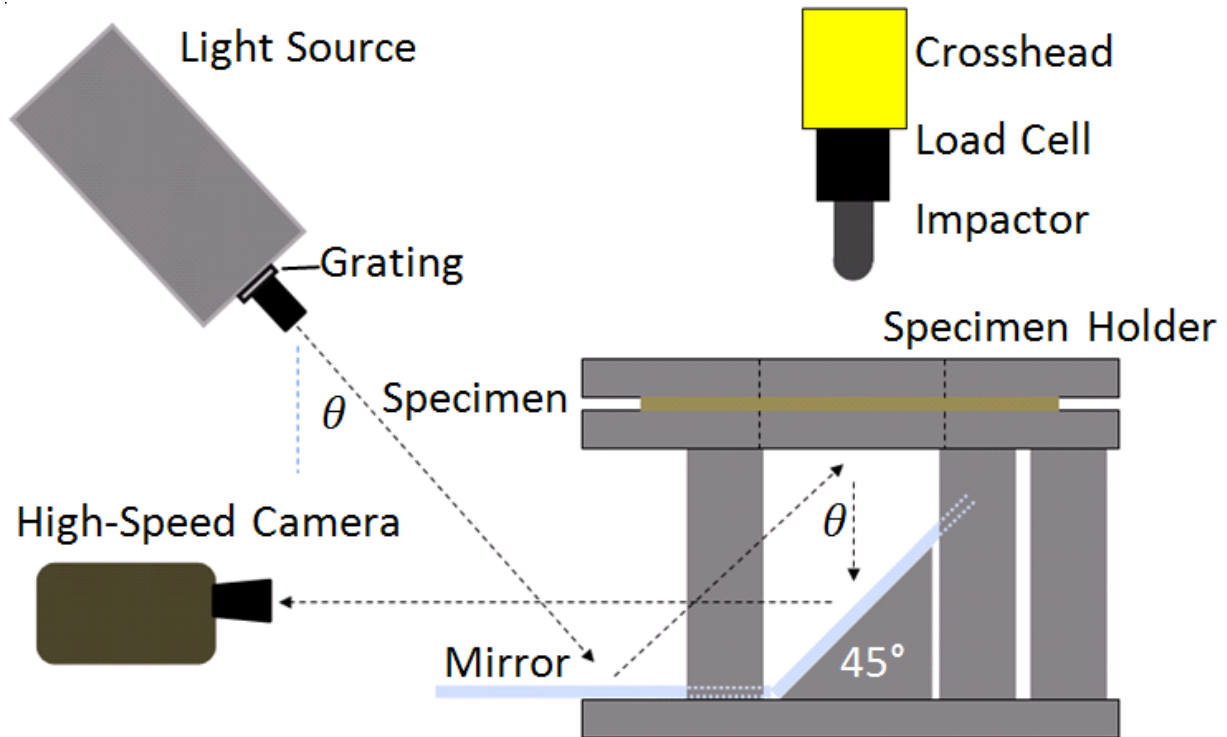


Figure 5. Viewed from the side, a schematic the DWIT specimen fixture and impactor with projection moiré incorporated. Note: Figure 5 not drawn to scale.

The high-speed camera and the light source were positioned such that the projected fringes from the light source would have to travel the same distance to the non-impact surface of the specimen as the light traveling from the non-impact surface of the specimen to the high-speed camera. This distance was roughly 1016 mm (40"). This distance was required as the minimum focusing distance of the Zeiss lens used was one meter and due to the infinite optics assumption. The angle  $\theta$  was approximately 26°. During testing, composite specimens were clamped between the two 15.9 mm (5/8") thick steel plates of the DWIT fixture and secured using eight equally spaced bolts that formed a 101.6 mm (4") diameter circle. The portion of the specimen subject to test was a 76.2 mm (3") diameter circle. The boundaries of the specimen were assumed to be fully clamped with this configuration.

There will be some amount of variation in the fringe pitch over a surface regardless of how ideal a physical test setup is for application of the infinite optics assumption. This will add curvature to the surface. Recalling the recommended criteria for the infinite optics assumption

- (1) The distance between the light source projecting the fringes and the reference plane is close to equal with the distance between the camera viewing position and the reference plane. *Both distances are roughly 1016 mm (40").*
- (2) The plane containing the light source and the camera viewing position is parallel to the reference plane. *This condition was not strictly adhered to due to the geometry of the test setup (Figure 5).*
- (3) The magnitude of the out-of-plane deformation is small compared to the distance between the camera viewing position and the reference plane.  $7 \text{ mm} < 1016 \text{ mm}$
- (4) The size of the surface of interest is small when compared to the distance between the projection and camera viewing positions.  $76.2 \text{ mm} < 1016 \text{ mm}$

#### **4.2 DWIT Calibration**

The calibration procedure for the fringe projection algorithm developed by Heredia-Ortiz [10] was applied using a calibration cone with a diameter of 39.8 mm and a height of 9.81 mm. As the frame rate increases the exposure time for each image decreases. The consequence of this is that at high frame rates and short exposure time, the illumination present in the image decreases and the contrast suffers. With the given lighting conditions in the fringe projection setup, there is a point at which the projected fringes become indistinguishable.

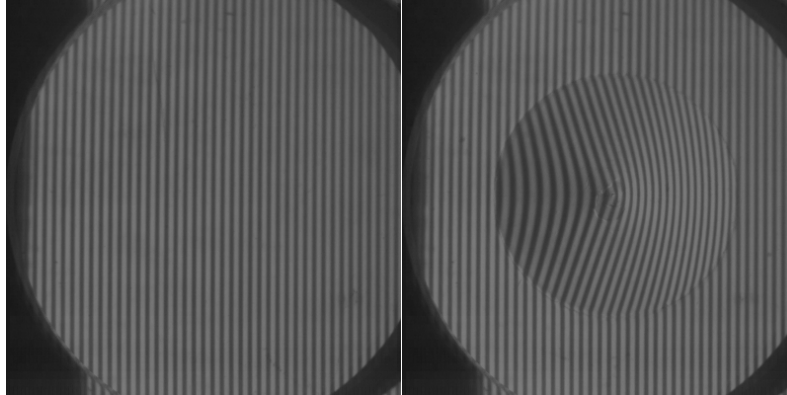


Figure 6. Reference plane and cone images with projected fringes while resting on the circular boundaries of the DWIT fixture.

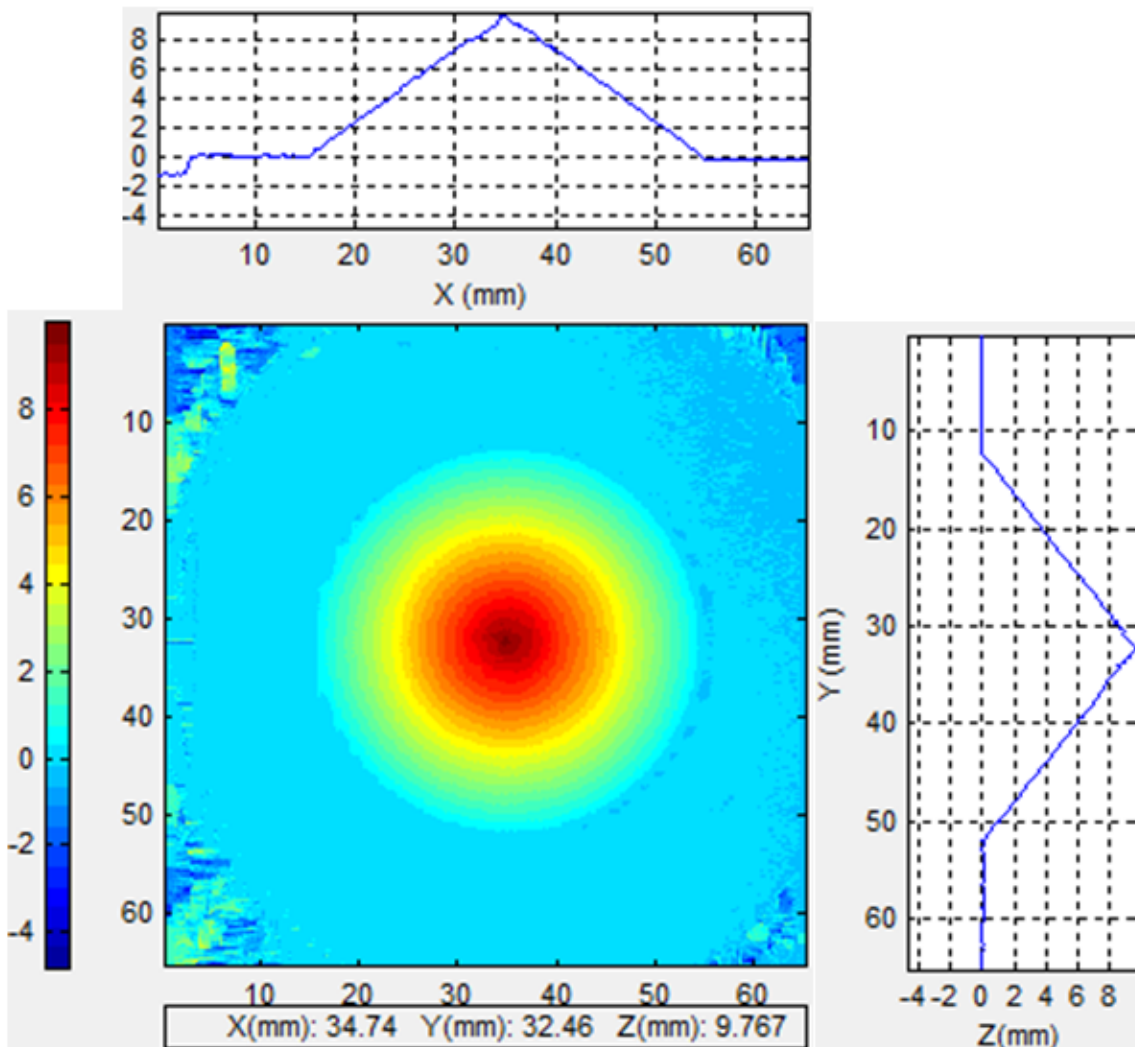


Figure 7. The contour plot showing the results of the calibration procedure with profiles across the peak of the cone displayed as well.

An important consideration during the calibration is the resolution of the fringes on the specimen. The accuracy of the fringe projection method is dependent not only on the contour interval of the fringes, but also on the number of pixels used to describe the pitch of the gratings. Gulker [15] conducted an investigation into the ideal pixel/pitch ratio. The results show the best accuracy in measurements taken with a ratio about 7 pixels/pitch. As the pixels/pitch ratio falls below 7, the accuracy of the fringe projection method decreases more significantly than the accuracy decreases when progressing from the 7-11 pixels/pitch range.

To evaluate the accuracy of the fringe projection setup applied to the DWIT, images of the calibration cone were taken and the dimensions of the calibration cone were measured using fringe projection. Table 1 suggests the fringe projection setup depicted in Figure 5 to be capable of performing measurements within 2%.

Table 1. Measurements of object using fringe projection in the DWIT setup.

	Known Dimension	Fringe Projection Cone Image 1	Percentage Difference	Fringe Projection Cone Image 2	Percentage Difference
Cone Height (mm)	9.81	9.94	-1.35	9.79	0.23
Cone Radius x - direction (mm)	19.90	19.57	1.68	19.58	1.61
Cone Radius y - direction (mm)	19.90	19.66	1.23	19.74	0.80

The pitch of the projected fringes upon the reference plane was 1.5208 mm (0.05987). The spatial resolution was 6.43 pixels/mm. The calibration constant was 0.398 mm/rad. Possible sources of error in the DWIT fringe projection setup include the infinite optics assumption, distortion effects of the lens and camera, sensitivity of the projected fringe configuration, sensitivity of the high-speed camera and errors associated with the processing of the data. Other parameters contributing to the Percentage Difference in Table 1 include the extraction of measured data through contour plots and measurements of the “Known Dimensions”.

It is important to note that selection of the pitch to use during testing is a compromise. Although projecting fringes with the smallest pitch possible seems ideal, the optics of the setup will prove otherwise. Using a pitch that is too small will result in too few pixels representing the fringes, compromising the accuracy of the projected fringes.

### **4.3 DWIT Data Processing**

Images of the impact event in the DWIT were captured at 15,000 fps. An image of the specimen with the light source on, but without projected fringes, was taken prior to impact. The image without projected fringes was used to normalize all of the test images. The normalization algorithm was also a result of the work by Heredia-Ortiz in Ref. [10]. The normalization algorithm adjusts the intensity values in the images to use the full range available, thus resulting in an enhanced image.

The fringe projection technique outputs a full-field contour map for each image processed. Each test on the DWIT generates 100-200 images. To generate a displacement history, the impact point (x,y-coordinates) is identified on a contour map through visual inspection. The displacement history from fringe projection is generated by extracting the displacement information from this point for each image. To determine the error potentially induced through visually inspection, several displacement histories were extracted on an ever increasing diameter ring around the point of impact. The deviation in Table 2 was determined by finding the difference between the selected peak point and four points around a ring that were averaged. The radii of the rings from which points were selected were one, two, and three millimeters. The rings were selected such that the peak displacement point occurred at their center.

Table 2. Deviation in peak displacement.

Distance from Peak (mm)	Deviation (mm)
1	0.015
2	0.209
3	0.467

The displacement history from the load cell was computed in addition to the fringe projection displacement history. A calibration constant was used to convert the voltage output of the load cell to force. To transform the force history into a displacement history, two numerical integrations were performed on the load cell data. The two pieces of information required to perform the numerical integration were the velocity of the impactor at the moment immediately prior to the time of impact and the initial displacement, which is zero. The initial velocity was calculated based upon ideal conditions using the conversion of potential energy to kinetic energy and then compared to an experimentally measured initial velocity. The initial velocity was measured through the use of a toothed velocity flag and an infrared emitter and collector. Small changes in the magnitude of the initial velocity used in the numerical integration have a magnified effect on the calculated displacement history (A 1% change in initial velocity has demonstrated a 1.5% change in displacement). Comparing the measured initial velocity with the theoretical initial velocity helps provide a point of reference and validity to the measured term.

#### **4.4 DWIT Results**

The displacement histories recorded from a DWIT test using the load cell and fringe projection are presented in Figure 8. The displacement history garnered from the load cell data is at the point of impact on the impact surface of the specimen. The displacement history from the fringe projection technique is at the point of impact on the non-impact surface of the specimen.

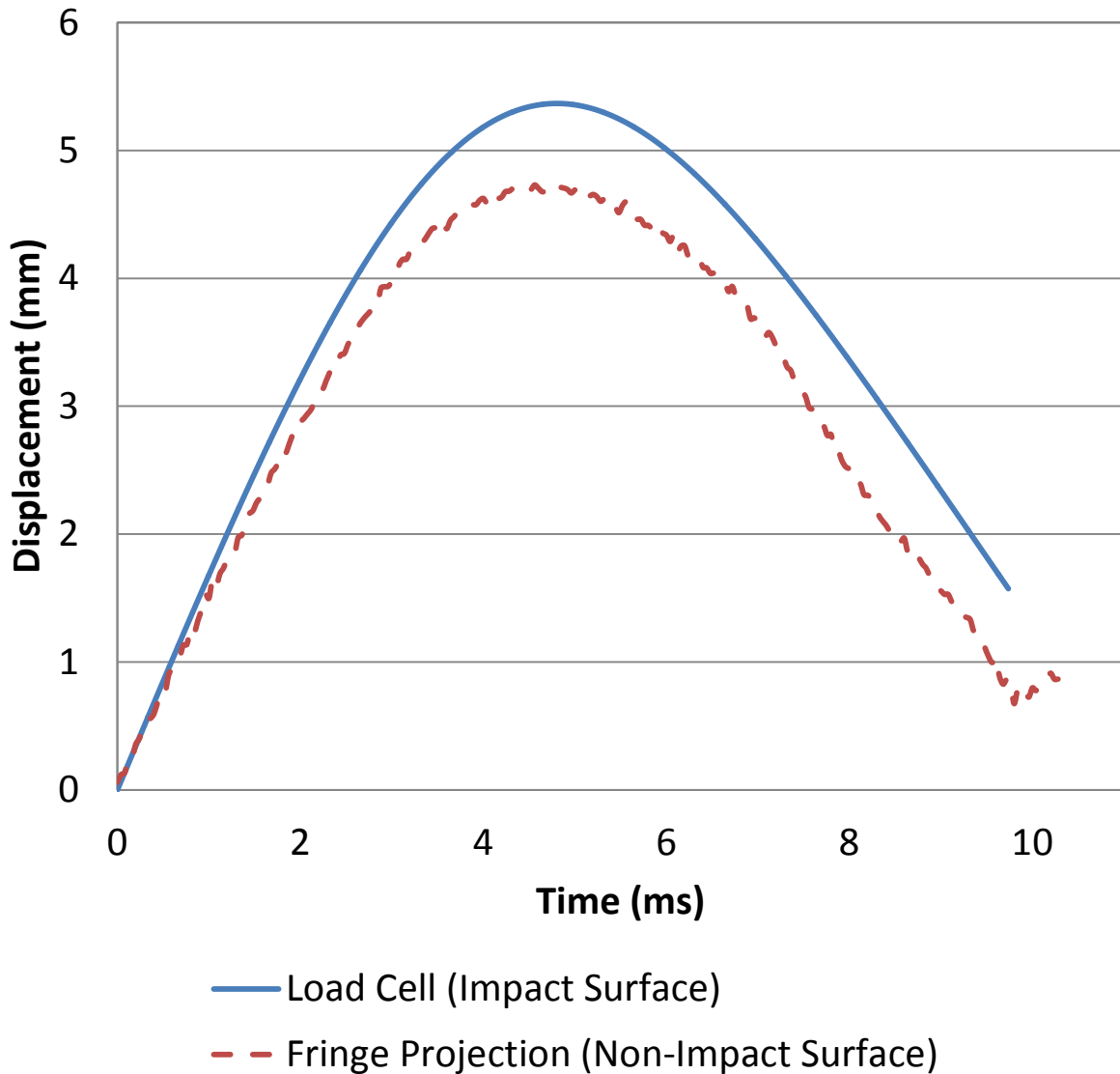


Figure 8. Displacement histories from a DWIT test gathered from numerical integrations of load cell data and fringe projection. The impactor mass of 5.01 kg was released from a height of 152.4 mm (6”) above the 75.6 mm (3”) diameter specimen with clamped boundaries. The test specimen was a composite composed of 3 plies of woven E-glass fibers with a SC-15 matrix. The thickness of the specimen was 2.01 mm (0.079”).

Figure 8 demonstrates that fringe projection is capable of documenting the overall trends associated with out-of-plane impact testing. Fringe projection has been shown to be accurate to within 2% of the measurement range used for a particular setup as indicated in Table 1. The difference between the two data sets is a result of the thickness change of the specimen used

during testing and potential experimental errors. The load cell captures displacement data on the surface of the specimen experiencing the impact. Fringe projection captures the displacement data on the surface opposite the impact or the rear surface of the specimen. The peak displacement recorded by the load cell for this case was 5.12 mm and the peak displacement captured fringe projection was 4.70 mm. This difference of 0.42 mm or 8.2% can, to a certain extent, be accounted for by the indentation the impact surface experiences during testing that the rear surface does not. Experimental errors accounting for the data discrepancy include proper calibration of the load cell, the measured impact velocity used during data processing, and errors associated with the fringe projection method previously outlined.

DWIT testing was conducted on composite specimens with various thicknesses. The percentage difference between peak displacements in data sets coming from the DWIT load cell and the fringe projection technique were considered. Percentage differences in composite specimens with the same structure and materials were averaged together and plotted as one data point in Figure 9. Figure 9 demonstrates that the percentage difference between load cell and fringe projection peak displacements increases with specimen thickness, indicating that the accuracy of fringe projection decreases with increasing specimen thickness.

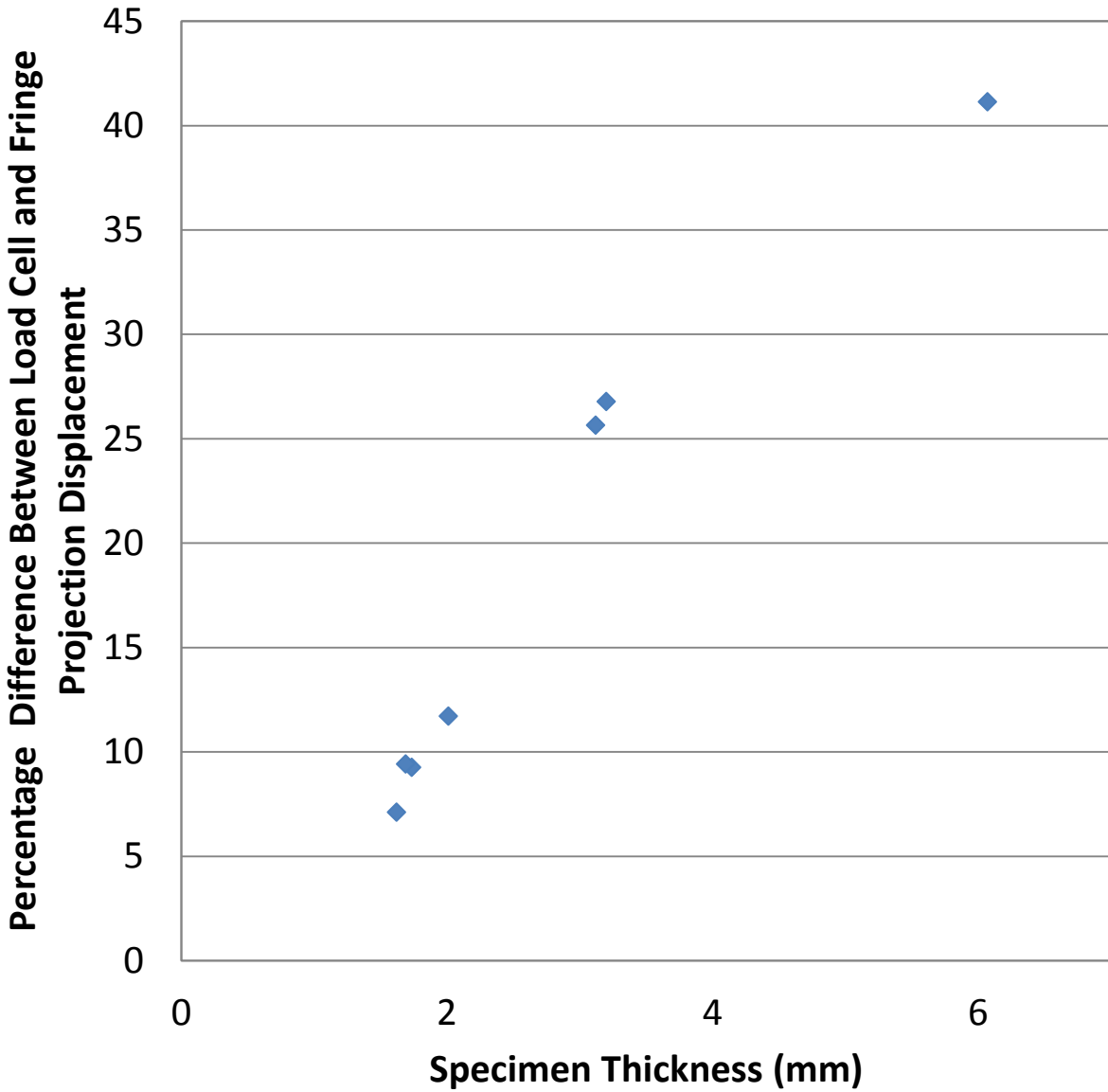


Figure 9. A plot of the percentage difference between load cell and fringe projection peak displacements as a function of specimen thickness.

## **5. Fringe Projection Applied to the Gas Assisted Horizontal Impactor (GAHI)**

### **5.1. Fringe Projection Applied to the Gas Assisted Horizontal Impactor (GAHI)**

The Gas Assisted Horizontal Impactor uses nitrogen gas to propel a projectile horizontally through a guide tube and into a vertically positioned specimen, resulting in out-of-plane deformation of the specimen. The specimen in its fully clamped boundary fixture is housed in a protective steel box with a shatter resistant viewing window. Fringe projection was integrating into the GAHI setup to measure the out-of-plane displacement during impact from the projectile. The fringes were projected directly onto the non-impacted specimen surface from the light source. The light source consisted of a 1000 watt halogen bulb. A 20 lines/mm Ronchi ruling was placed behind a 12.5-75 mm zoom TV lens. The TV lens was used to focus and adjust the fringe pitch on the specimen surface. To capture images for processing, a Vision Research Phantom v12.1 high-speed camera was used. The camera was outfitted with a Carl Zeiss Planar T\* 1.4/85 mm ZF.2 lens. A 254 mm x 254 mm (10" x 10") mirror was positioned vertically to facilitate high-speed camera viewing of the specimen surface. The mirror was oriented at  $45^{\circ}$  with respect to the normal of the specimen surface to provide a normal viewing perspective for the high-speed camera.

Various guide tubes and projectiles were used in testing. Different guide tubes were used to facilitate the different projectile diameters. Projectile velocities during testing were varied from 50 m/s to 110 m/s. Velocity measurements were taken using the high-speed camera at 100,000 fps by observing projectiles at the same distance from the guide tube exit that specimens would be clamped during testing. A known distance-reference was placed parallel and less than 12.7 mm (0.5") from the path of the projectile exiting the guide tube. These velocity

measurements were correlated with the pressure in the holding chamber prior to release.

Velocity measurements for a given pressure varied 3% or less.

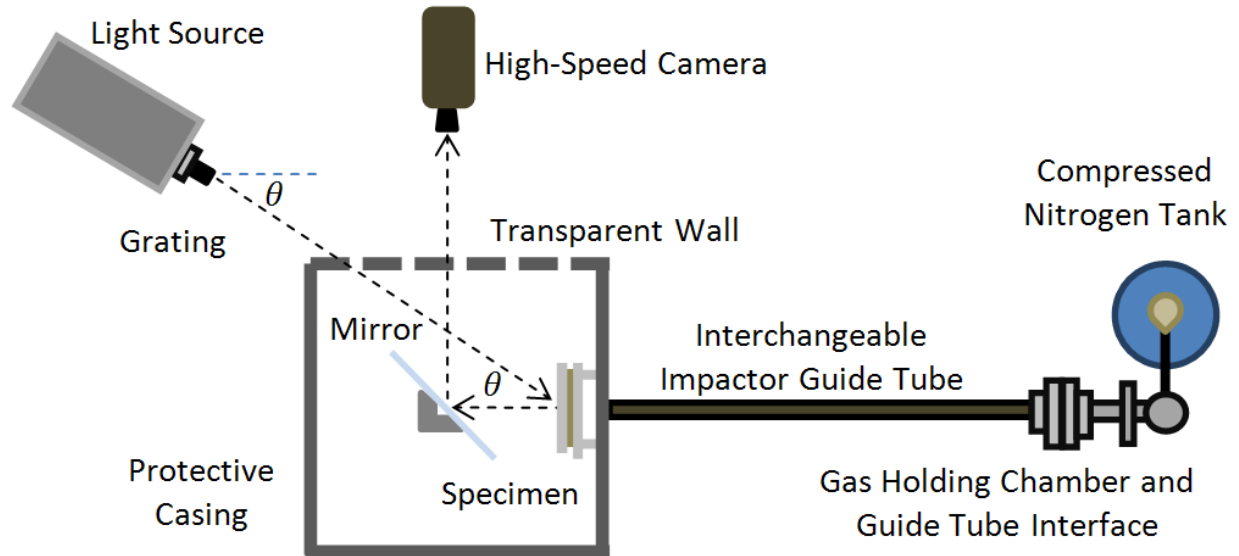


Figure 10. Viewed from above, schematic of the GAHI to which fringe projection was applied.

The distance light travels from the specimen to the high-speed camera and from the specimen to the light source was 1270 mm (50"). The angle between the viewing and the projected axis,  $\theta$ , was  $37^\circ$ . The distance between the light source and the camera was 1016 mm (40"). For the testing conducted, the out-of-plane displacement did not exceed 9 mm.

- (1) The distance between the light source projecting the fringes and the reference plane is close to equal with the distance between the camera viewing position and the reference plane.. *Both distances are approximately 1270 mm (50").*
- (2) The plane containing the light source and the camera viewing position is parallel to the reference plane. *This condition was not strictly adhered to due to the geometry of the test setup.*

- (3) The magnitude of the out-of-plane deformation is small compared to the distance between the camera viewing position and the reference plane.  $9 \text{ mm} < 1270 \text{ mm}$ , a sufficient ratio for the infinite optics assumption.
- (4) The size of the surface of interest is small when compared to the distance between the projection and camera viewing positions.  $152.4 \text{ mm} < 1016 \text{ mm}$  (for GAHI specimens only a section was filmed during impact,  $152.4 \text{ mm}$  (6") was the length of the longest section). The geometry of the setup and the desired pixel/fringe ratio placed limits on this ratio.

The calibration procedure previously described in conjunction with the DWIT was applied using a cone height of 9.81 mm and a radius of 19.9 mm. The TV zoom lens used to project fringes was adjusted to accommodate the different size specimens. Image resolution of the high-speed camera was also adjusted to accommodate specimen size. Due to the short duration of the impacts during GAHI tests and the size of the specimens used, the high-speed camera resolution was adjusted to include the impact point on the specimen and a portion of the accompanying fixture. Limiting the area of interest to a portion of the symmetrical deformation field allowed for the use of greater frame rates during testing and a reduction in fringe pitch. This resulted in an increase in data resolution and an increase in the sensitivity of the data.

The GAHI experimental setup involves a compromise between optical parameters, physical geometries, and impact durations. For the GAHI geometry, the lower limit of  $\theta$  is restricted due to the placement of the protective casing surrounding the specimen. The short loading durations (Table 3) necessitate the need for the frame rates. High frame rates come at the expensive of image resolution and illumination. One of the primary concerns during testing

was achieving a high testing frame rate with sufficient contrast in the image so that the images can be processed. Procedural information regarding GAHI testing can be found in Appendix A.

Table 3. Test condition correlation with optical parameters.

	GAHI Test Configuration A	GAHI Test Configuration B	GAHI Test Configuration C	DWIT
Specimen Diameter	76.2 mm (3")	127 mm (5")	254 mm (10")	76.2 mm (3")
Specimen Thickness	2.01 mm (0.79")	3.12 mm (0.123")	6.07 mm (0.239")	2.01 mm (0.79")
Impactor Diameter	3.81 mm (0.15")	6.3 5mm (0.25")	12.7 mm (0.50")	12.7 mm (0.50")
Impactor Mass	0.916 g	4.217 g	33.629 g	5.01 kg
Duration of Loading	<0.05 ms	<0.10 ms	<0.20 ms	<5 ms
Test Frame Rate	110,019 fps	88,050 fps	52,044 fps	15,000 fps
Images Captured During Loading	<7	<8	<11	75
Test Image Resolution	208 x 128	368 x 144	512 x 200	136 x 432
Test Area of Interest	60 mm x 40 mm	108 mm x 42 mm	160 mm x 63 mm	36 mm x 60 mm
Fringe Pitch on Reference Plane	2.20 mm	2.186 mm	2.716 mm	1.44 mm
Spatial Resolution	3.47 pixels/mm	3.42 pixels/mm	3.19 pixels/mm	6.43 pixels/mm
Calibration Constant	0.4780 mm/rad	0.46581 mm/rad	0.4535 mm/rad	0.398 mm/rad

## 5.2 Accuracy of Fringe Projection Applied to the GAHI

Dimensions of the calibration cone were measured using fringe projection for each configuration in Table 3. The images were captured at a frame rate of 10,000 fps. From Table 4, the accuracy of the measurements were within 4% for Configuration A, 2% for Configuration B, and 5% for Configuration C. The accuracy of the fringe projection setup for the GAHI is less

than that for the DWIT. The fringe projection sensitivity and spatial resolution are both reduced in the GAHI fringe projection setup. The light source and camera were placed at greater distances in the GAHI setup to better allow for use of the infinite optics assumption with the larger specimens used in the GAHI testing. Despite the increased distances between pieces of the optical arrangement, some of the ratios used when considering the application of the infinite optics assumption were less than the same ratio from the DWIT test configuration. The consequence in placing the optical pieces at greater distances from the test specimen is that spatial resolution is compromised and the intensity of the illumination from the light source decreases.

Table 4. Accuracy Measurements and Quantification.

		Cone Height	Cone Radius X-Direction	Cone Radius Y-Direction
GAHI Test Configuration	Established Value (mm)	9.81	19.90	19.90
A	Fringe Projection Measured Value (mm)	9.48	19.76	19.61
	Percentage Difference	3.36	0.70	1.46
B	Fringe Projection Measured Value (mm)	9.64	20.19	19.62
	Percentage Difference	1.73	-1.46	1.41
C	Fringe Projection Measured Value (mm)	9.36	20.20	19.60
	Percentage Difference	4.59	-1.51	1.51

The possibility of degradation of fringe projection accuracy with an increase in frame rate was considered. Images of the calibration cone used in the calibration procedures for the DWIT and GAHI and a smaller calibration cone were taken at 10,000 fps and the accompanying frame rate with each GAHI Test Configuration in Table 3. The results (Appendix B, Tables 5-7) did not show a consistent decrease in accuracy with an increasing frame rate. Processing of the images from test frame rates did require the use of a normalization algorithm to produce useful

results. Despite the quantitative measurements, from a qualitative standpoint, the quality of the out-of-plane contour plots decreased at higher frame rates. The contour plots were prone to portions lacking data, especially on the face of the cone away from the projection axis where fringe spacing and thickness decreases. The fringes in this area are represented by fewer pixels and are more susceptible to a lack of contrast in the captured images. Determination of the cone features from the contour plots proved more difficult at higher frame rates due to the decrease in feature distinction when compared to contour plots from lower frame rates.

### **5.3 GAHI Test Results**

The fringe projection method was used to measure out-of-plane displacement on the non-impact surface of specimens used in GAHI testing. The data points corresponding to the initial loading of the projectile strike were used to evaluate the impact-based bending stiffness of the material.

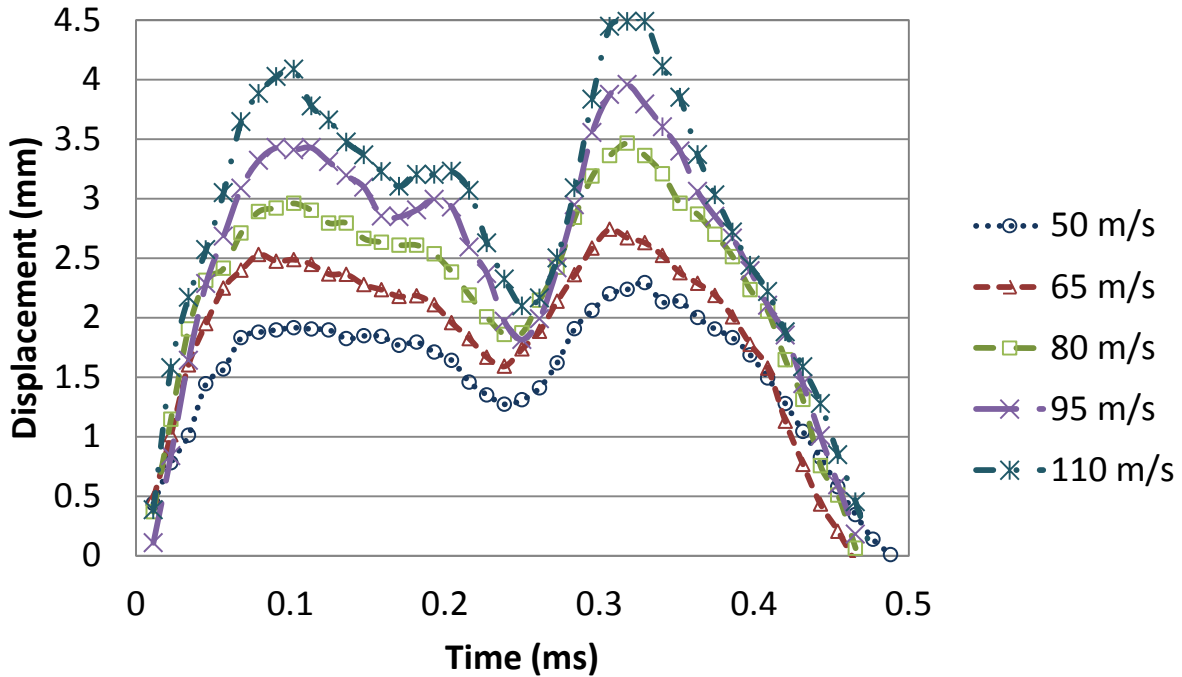


Figure 11. Displacement histories for the impact point from GAHI testing using GAHI Test Configuration B with specimens made of woven E-glass fibers and a SC-15 matrix.

#### 5.4 Double Peak Investigation

The sample results in Figure 11 show two distinct displacement peaks from a single projectile striking a composite specimen. To gain insight into the actual physical occurrences, a high-speed camera was used to film the projectile striking the impact surface of the composite plate with the impact conditions the same as those for the 80 m/s test seen in Figure 11. The Phantom v12.1 high-speed camera was used to record the event at 100,000 fps. The fringe projection video was recorded at 88,050 fps. Testing events can be filmed above the frame rate used to capture the fringe projection results because of the lighting restrictions imposed through the application of fringe projection are no longer present. Frames from the projectile striking the composite plate were correlated with the measured displacement from fringe projection applied to the non-impact surface of the plate and are featured in Figure 12.

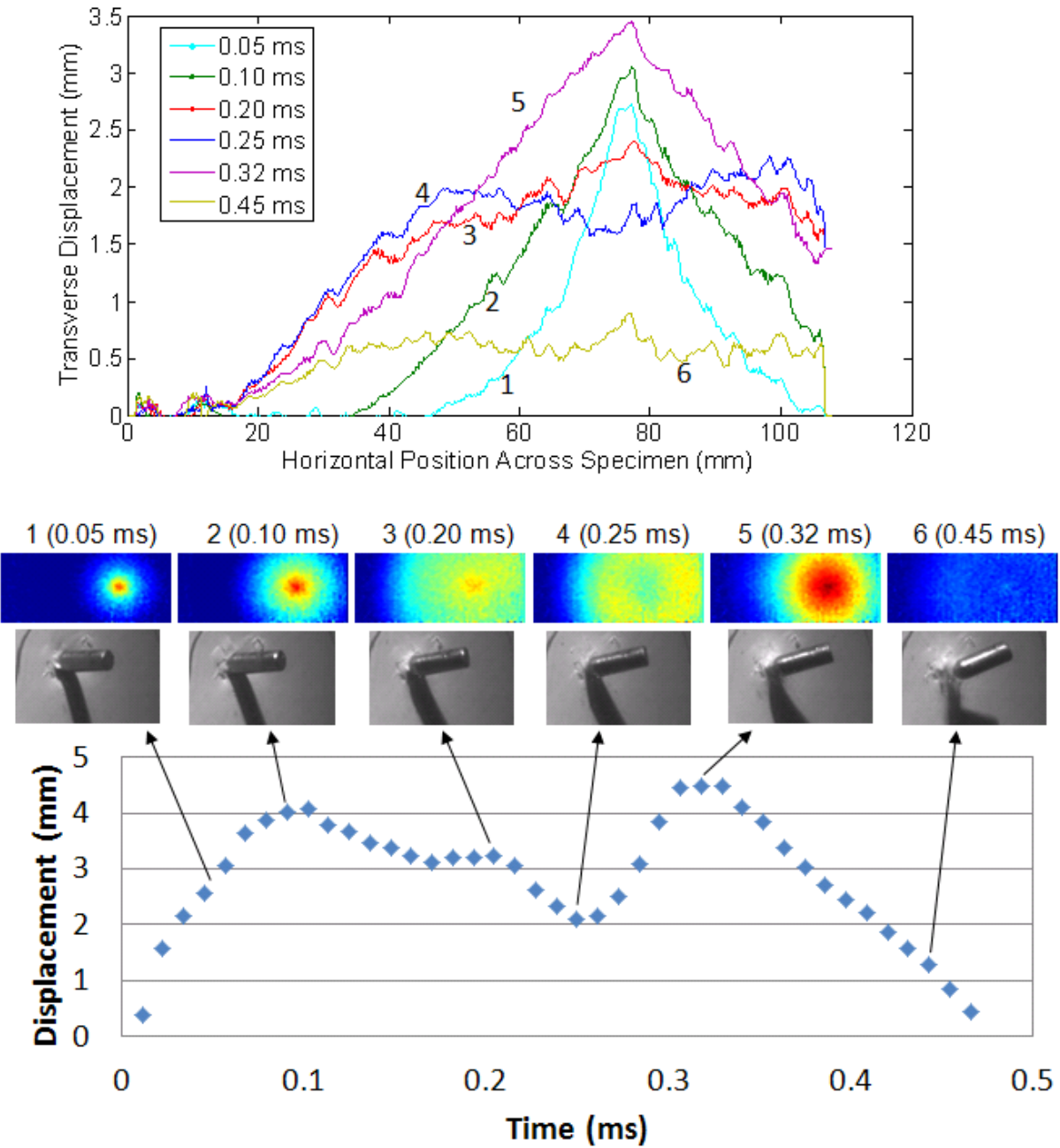


Figure 12. Fringe projection displacement history (bottom) correlated with the high-speed video of the projectile striking the impact surface and the horizontal displacement profiles (top). The case documented is for Configuration B of Table 3 with the projectile striking a composite plate at 80 m/s composed of woven E-glass fibers with a SC-15 matrix.

#### ***5.4.1 Fringe Projection Displacement History and High-Speed Video Correlation***

The video of the projectile impact shows that the projectile maintains a forward motion for the first 10 frames (0.10 ms) from the onset of impact. Comparing the images of the projectile impact with the fringe projection deformation history, motion of the projectile into the composite plate lasts for roughly 0.10 ms, which correlates well to the first peak seen in the deformation history of Figure 12. In the projectile impact video, the projectile reverses its original motion, moving away from the plate, while remaining in contact with the composite plate from 0.10 to 0.24 ms after the onset of impact. The exact point at which the projectile loses contact with the composite plate cannot be stated with certainty due to the recording angle of the video. At 0.24 ms after the onset of impact, the projectile appears to lose contact with the plate. The rebound motion of the projectile with the deformation history of Figure 12 correlates well up to 0.24 ms. After the 0.24 ms time point, the projectile does not regain contact with the composite plate. From Figure 12, the second peak in the deformation history is achieved at 0.32 ms. At this point in time, the projectile is moving away from the plate and beginning to rotate. Since the deformation history recorded by fringe projection occurs on the non-impact surface and the projectile impact video occurs on the impact surface, there is undoubtedly a time delay between the point in time at which the projectile first contacts the impact surface and the time at which deformation is detected by fringe projection on the opposite surface. Consequently, the events that occur in the projectile impact video cannot be correlated exactly with the deformation, but they correlate very well. Despite the potential for a time delay induced error, the projectile does not demonstrate motion into the composite plate beyond 0.10 ms after first contact. The second peak in Figure 12 is not the result of projectile motion into the plate occurring at the corresponding time as the second peak.

#### ***5.4.2 Non-Impact Surface Video***

A video of the non-impact surface during the projectile impact at 80 m/s was recorded without fringes at 100,000 fps. This video shows that the deformation trends reported through the fringe projection measurement are indeed accurate. From the non-impact surface video, the non-impact surface deforms for roughly 0.11 ms from the first sign of impact until the first deformation peak is reached. Following this period, the point of peak displacement begins to rebound until approximately 0.20 ms after initial contact. A brief pause in the displacement recovery is seen on the video and in Figure 10 at 0.20 ms. The bottom of the trough seen in Figure 12 is very difficult to identify in the non-impact surface video. The second peak displacement does appear to occur around 0.31 ms which is in agreement with the fringe projection measurements. Following this second peak, the composite plate begins to rebound significantly in the video, which corresponds with the complete rebound seen in Figure 13 after 0.50 ms. The non-impact surface video shows that the deformation history measured through fringe projection follows the physical happenings of the non-impact specimen surface.

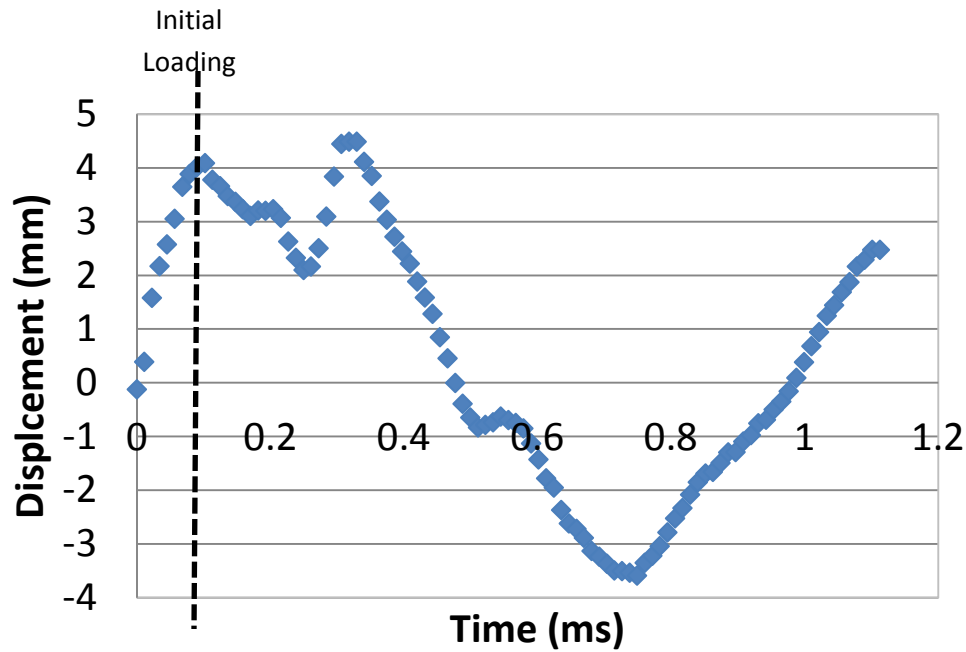


Figure 13. Extended deformation history for the 80 m/s test case featured in Figures 11 and 12.

### 5.4.3 Double Peak Mechanism

The double peak can be attributed to the passage of a wave through the plate prior to the composite plate recovering fully from the deformation from the projectile impact. There are two deformation behaviors that are observable in the videos with one (plate body) occurring much more slowly than the other (plate center). As the load is applied at the plate center, the entire composite plate experiences a certain degree of deformation. The plate center experiences the greatest displacement with plate body experiencing an ever decreasing degree of displacement as the distance from the center of the plate increases until the constrained boundaries with zero displacement are reached. This gradual displacement is seen in the observation videos discussed in sections 5.4.1 and 5.4.2 as the relatively gradual bending of the plate body. The plate body as a whole oscillates following impact. Similar to the way a musical drum moves after being struck. This oscillatory behavior is seen in Figure 13 as the point of impact experiences a positive displacement (0 to 0.5 ms), a negative displacement (0.5 to 1.0 ms), and a positive

displacement (beyond 1.0 ms). Review of fringe projection test video from other tests presented in Figure 11 can also confirm this behavior of the composite plate following impact.

The second component of the observed displacement occurs much more rapidly. This portion demonstrates itself in the manner in which the plate center seems to deform almost independently of the plate body. This is caused by the waves that propagate outward from the point of impact at the time of impact. These waves travel radially away from the center. The displacement resulting from these waves can be superimposed on to the relatively slow and gradual displacement of the plate body. These waves contribute to the mini-peak, trough and second major peak seen on the displacement history curves near 0.20 ms, 0.24 ms and 0.32 ms, respectively in Figure 12. The second peak is the result of a wave that had traveled radially outward from the specimen center, been reflected, and had reached the impact point prior to the movement of the plate body from its initial deformed state (0 to 0.5 ms).

## **5.5 Fringe Projection Lighting**

A significant factor to consider in the application of fringe projection to dynamic impacts is the duration of the impact event. The frame rate of the high-speed camera used to record the event is inversely correlated to exposure time. As the frame rate is increased, the exposure time or the time the camera collects light for each image decreases. At some point, the intensity of the light captured by the camera will be insufficient to generate an image with distinguishable features. For dynamic testing this can be problematic as a certain exposure time or frame rate will be required to achieve sufficient data resolution. One solution to this issue is to increase the light intensity and the contrast that exists in the object of which an image is desired. For fringe projection, increasing the lighting in the test setup cannot be achieved by simply adding additional light directly onto the specimen since applying lighting directly to the specimen will

drown out the projected fringes. Increases in lighting must originate from behind the projected grating. The light emitted from behind the gratings, must pass through the gratings and a focusing lens. The lens is used to focus the fringes on the object of interest and vary the pitch. Light intensity losses are sustained as the light travels through the grating and the focusing lens. Finding the brightest light source possible is recommended for high-speed tests, although it may be problematic due to cost, opportunity or applicability. The light/grating source could also be placed closer to the test specimen so that losses of light intensity are reduced. Performing this action also has its limits in that the closer the light source and camera are to the specimen, the less the idealization that fringe pitch is constant across the area of interest is applicable. Also, restricting this option is that the specimen may be large in size or the camera lens in use has a relevant minimum focusing distance. Another option for increasing data resolution is to redesign the experimental process so that the duration of the impact event is increased. This option has its limits as well as certain size and specimen requirements may not be amendable depending on the goals of the investigation.

From experimental investigations, the upper limit of the frame rates capable of producing processable fringe projection images is in the 120,000 to 130,000 fps range for the equipment used. The accuracy of the data gathered at the upper frame rate should be approached with skepticism. The application of higher frame rates to large test specimens such as those used in GAHI Test Configuration C is also limited by the achievable image resolution (size of the picture). Given that a portion of the specimen fixture (serves as a zero displacement reference) as well as the region of impact need to be contained in the camera field of view, larger test specimens require greater image resolution. Image resolution and frame rate were inversely

correlated for the high-speed camera used in this study, resulting in the use of lower frame rates to accommodate larger test specimens in the application of fringe projection.

## 6. Conclusion

Fringe projection is used to measure out-of-plane contour information. In this study it has been applied to two dynamic testing apparatus, a drop weight impact tower and the GAHI, to measure out-of-plane displacement. Fringe projection provides a full-field means through which the out-of-plane deformation of composite plates can be measured. The displacement history can potentially be used to calculate the impact-based bending stiffness of the impacted materials. This facilitates the study of composites under high and varying rates of loading.

When applying fringe projection, the following parameters need to be carefully considered

- 1) the interaction between lighting/frame rate/impact duration
- 2) the pixel/pitch ratio– the lower limit of the fringe pitch on the specimen surface will be restricted by the camera used for a given test configuration
- 3) the infinite optics assumption (viewing/projecting distances and specimen size/deformation)
- 4) the angle between projection and viewing angles (angles between  $10^\circ$  - $30^\circ$  have shown reasonable results)

Although fringe projection can be useful means to measure dynamic out-of-plane motion it is not without its limitations. Severe damage to the non-impact specimen surface is one of them as this corrupts the data. The lighting limitation is another, which stems from the need to project fringes on an object of interest from a significant distance. This places a limit on the impact duration of the dynamic events to which fringe projection should be applied. Fringe projection has been

applied to dynamic test setups in this study, but it is not without limitation. These limitations require attention when considering application of the method.

## **APPENDICIES**

## **Appendix A: GAHI Experimentation Procedural Information**

1. Place the desired specimen and clamping apparatus on the four guide rods in the protective casing of the gas assisted horizontal impactor.
2. Place a mirror in the protective casing at a  $45^\circ$  relative to the specimen surface such that the high-speed Phantom v12.1 camera can be used to observe the specimen surface from a normal perspective.
3. Place and orient the high-speed camera so that the mirror is at a  $45^\circ$  with respect to the camera. The high-speed camera should have a normal viewing perspective of the specimen surface.
4. Place and orient the light source so that the projection angle is between  $30^\circ$  and  $40^\circ$ . This angle is limited due to the GAHI protective casing.
5. The exact distance that light travels from the specimen to the high-speed camera and from the specimen to the light source will vary depending on the experimental equipment use.
6. Adjust the lens and position of the light source so that fringes are cast upon the specimen center and outward towards the edge of the fixture. The fixture is assumed to experience zero displacement during the test event and as such it is used as a zero-displacement reference.
7. Continue to adjust the lens and position of the light source as well as the position of the high-speed camera so that the fringe density is around 7 pixels/pitch (recall that the pitch is the distance between the fringes). Achieving this fringe density may not be feasible depending on the equipment in play and the geometry of the test setup.

8. Adjust the camera position and frame rate so that the impact point on the specimen and a small portion of the test fixture is within the field of view of the camera. It is important that fringes are focused on the specimen across the portion of the specimen and fixture to be captured by the high-speed camera. Check that the desired image resolution can be achieved at the testing frame rate.
9. Remove the test specimen and its fixture from its position on the four threaded mounting rods.
10. Two calibration cone/reference plate holders were constructed, one for smaller specimens and one for test specimens 254 mm (10") test diameters. This was done as the threaded mounting rods inside the protective casing of the GAHI need to be reconfigured when testing of larger specimens occurs.
11. Place the calibration cone/reference plate such that the reference plane lies at the same depth in the protective casing that the non-impact surface of the test specimen will during testing. The height of the calibration cone should be slightly greater than the expected deformation of the test specimen.
12. Use the high-speed camera to capture images of the calibration cone and the reference plane. When considering the calibration cone in conjunction with the fringe density, errors in processing the images may arise when too few pixels are available to represent the fringes on the cone. The fringes on the cone away from the light source decrease in width as a result of the cone gradient. The number of pixels representing each frame will decrease as a result. There will be a point at which there are insufficient pixels available to represent the fringe.

13. Process the calibration images to determine the calibration parameters and to ensure proper alignment of the system.
14. Once calibration is complete, the test specimen and its fixture should be secured back onto the threaded mounting rods.
15. The activation button for the GAHI electronically activates a valve that releases nitrogen gas propelling the projectile in GAHI testing. This activation trigger for the high-speed camera is integrated into the GAHI activation button. This means that the high-speed camera begins recording as soon as the GAHI activation button is depressed. This should be taken into account when conducting testing as the high-speed camera will only record images for a finite amount of time and there will be a time lapse from trigger activation to the impact event.

## Appendix B: Accuracy and Frame Rate

Table 5. Accuracy Measurements for Configuration A\* (Spatial Res~3.47 pixels/mm,K~0.49).

	Cone Height (mm)	Cone Radius X-Direction (mm)	Cone Radius Y-Direction (mm)
Established Value	9.81	19.9	19.9
Fringe Projection Measured Value with Frame Rate at 10,000 fps	9.601	19.62	19.76
Percentage Difference	2.13	1.41	0.70
Fringe Projection Measured Value with Frame Rate at 110,019 fps	9.48	19.47	-
Percentage Difference	3.32	2.16	-
	Cone Height (mm)	Cone Radius X-Direction (mm)	Cone Radius Y-Direction (mm)
Established Value	4.91	19.83	19.83
Fringe Projection Measured Value with Frame Rate at 10,000 fps	4.656	19.9	19.475
Percentage Difference	5.17	-0.35	1.79
Fringe Projection Measured Value with Frame Rate at 110,019 fps	4.694	20.75	-
Percentage Difference	4.40	-4.64	-

Table 6. Accuracy Measurements for Configuration B\* (Spatial Res~3.57 pixels/mm,K~0.486).

	Cone Height (mm)	Cone Radius X-Direction (mm)	Cone Radius Y-Direction (mm)
Established Value	9.81	19.9	19.9
Fringe Projection Measured Value with Frame Rate at 10,000 fps	9.168	20.04	19.62
Percentage Difference	6.54	-0.70	1.41
Fringe Projection Measured Value with Frame Rate at 88,050 fps	9.324	19.9	19.34
Percentage Difference	4.95	0.00	2.81
	Cone Height (mm)	Cone Radius X-Direction (mm)	Cone Radius Y-Direction (mm)
Established Value	4.91	19.83	19.83
Fringe Projection Measured Value with Frame Rate at 10,000 fps	4.63875	19.76	19.48
Percentage Difference	5.52	0.35	1.77
Fringe Projection Measured Value with Frame Rate at 88,050 fps	4.80225	20.04	19.2
Percentage Difference	2.19	-1.06	3.18

Table 7. Accuracy Measurements for Configuration C\* (Spatial Res~3.67 pixels/mm,K~0.55).

	Cone Height (mm)	Cone Radius X-Direction (mm)	Cone Radius Y-Direction (mm)
Established Value	9.81	19.9	19.9
Fringe Projection Measured Value with Frame Rate at 10,000 fps	9.1835	19.76	19.085
Percentage Difference	6.39	0.70	4.10
Fringe Projection Measured Value with Frame Rate at 52,044 fps	9.3035	19.36	19.36
Percentage Difference	5.16	2.71	2.71
	Cone Height (mm)	Cone Radius X-Direction (mm)	Cone Radius Y-Direction (mm)
Established Value	4.91	19.83	19.83
Fringe Projection Measured Value with Frame Rate at 10,000 fps	4.52	19.77	19.08
Percentage Difference	7.94	0.30	3.78
Fringe Projection Measured Value with Frame Rate at 52,044 fps	4.4933	20.035	19.22
Percentage Difference	8.49	-1.03	3.08

## REFERENCES

## REFERENCES

1. Weeks, C.A., Sun, C.T., “Modeling non-linear rate-dependent behavior in fiber-reinforced composites”. *Compos Science Technology*, 58, 603–611, (1998).
2. Abrate, S., Impact on Composite Structures. Cambridge University Press., Cambridge, (1998).
3. Heredia-Ortiz, M., and Patterson, E.A., ‘On the Industrial Applications of Moiré and Fringe Projection Techniques’, *Strain*, 39, 95-100, (2003).
4. Fleming, G. A., and Gorton, S. A., “Measurement of rotorcraft blade deformation using Projection Moiré Interferometry”, *Journal of Shock and Vibration*, Vol. 7, No. 3, (2000).
5. Takasaki, H., “Moiré Topography,” *Applied Optics*. 9, 1467-1472, (1970).
6. Breque, C., Dupre, J.C., Bremand, F., “Calibration of a system of projection-moiré for relief measuring: biomechanical applications”, *Optics and Lasers Engineering*, 41, 241–260, (2004).
7. Gorthi, S.S., and Rastogi, P, “Fringe Projection Techniques: Whiter we are?”, *Optics and Lasers Engineering*, 48(2), 133-140, (2010).
8. Sciammarella, C.A., “The moiré method –A review”, *Experimental Mechanics*, 22(11), 418-433 (1972).
9. Cloud, G.L., Creath K. Optical Methods of Engineering Analysis. Cambridge University Press, Cambridge University Press, Cambridge, (1998).
10. Heredia-Ortiz , M., “Novel Developments of Moiré Techniques for Industrial Applications”, Doctoral Thesis, Sheffield, UK, University of Sheffield, (2004).
11. Heredia-Ortiz, M., and Patterson, E.A., “Location and Shape Measurement Using a Portable Fringe Projection System”, *Experimental Mechanics*, 45(3), 197-204, (2005).
12. Pirodda, L., “Shadow and projection moiré techniques for absolute or relative mapping of surface shapes”, *Optical Engineering*. 21(4), 640-649, (1982).
13. Doty, J.L., “Projection moiré for remote contour analysis”, *Journal of the Optical Society of America* ,73(3), 366-372 (1983).

14. Creath, K., Wyant, J., "Moiré and Fringe Projection Techniques," in. Optical Shop Testing, 2nd Ed., Ed. by D. Malacara, New York: Wiley, 653-685 (1992).
15. Gulker, B., "Techniques for Enhancing Impact Testing", Master's Thesis, East Lansing, MI, Michigan State University, (2009).
16. Kokidko, D., Gee, L., Chou, S.C., and Chiang, F.P., "Method for measuring transient out of plane-deformation during impact," *International Journal of Impact Engineering*, 19, 127-133, (1996).

## **Section 2: Scaling of Composite Materials Subject to Horizontal Impact**

### **Abstract**

Composite materials are being adapted in an ever increasing range of applications. The widespread application of composite materials requires that the behavior of the material be well understood. This understanding is gained in large part through testing on small laboratory specimens. The results attained from laboratory size specimens need to be applicable to service size components. This requires that consideration be paid to potential size effects. In this study, a scaling scheme was applied to an experimental setup and the accompanying composite test specimens. Scaling factors of 3, 5 and 10 were used to scale composite materials subject to horizontal impact from proportionally scaled gas accelerated projectiles at 50, 65, 80, 95 and 110 m/s. The whole-field out-of-plane displacement histories of the non-impact surface of the impacted test specimens were measured using fringe projection. Through consideration of the displacement histories at the point of impact on the non-impact surface, readjusted for scale, a size effect was not observed in the elastic range. Scaling was unable to account for the damage modes in test specimens across scales. The damage modes present and the delamination area in the test specimens were however more advanced in larger specimens and beyond what could be accounted for through scaling. With respect to damage, smaller specimens were stronger.

## **1. Introduction**

Composite materials are used in a variety of life-critical applications. These applications include vehicle structures such as airplanes where the margin for error in design and application is non-existent. To incorporate composite materials into life-critical applications, it is necessary to characterize and understand their material properties and behavior under a variety of loading conditions. This characterization process is performed through experimental testing. Testing on composite components with sizes smaller than the desired prototype is highly advantageous both financially and practically. The transition of these test results and conclusions to the intended application is not always a smooth one. Considering that a laboratory test may involve a test specimen a fraction of the size of the implemented component, there is potential for error in the application of laboratory testing results to the actual size structures. A change in behavior based upon the specimen size considered is known as a size effect. The change in material behavior could present itself in changes in elastic material properties or failure strengths. Composite materials naturally lend themselves to further scrutiny when considering size effects because of their heterogeneous nature.

Composite materials are designed for high-performance structures which are exposed to dynamic loading from time to time. In investigating the behavior of composite materials under intermediate velocity impact, parameters associated with the dynamic behavior of the composite are fundamentally important. Based on fringe projection, this study investigates histories of specimen deformation, damage, impactor force, and strain rate for size effect analysis.

## 2. Scaling

### 2.1 Scaling Relations

Scaling of structures subject to dynamic loading was considered in metals before composites. Duffey *et al* [1] considered the scaling of low-velocity impact of steel plates through analytical and experimental means. Morton [2,3] developed scaling rules using principles of similitude for laminated carbon-fiber composite beams subject to drop weight impact loading. Morton created physically similar impact events based on Buckingham's Pi theorem. The Buckingham Pi theorem is used to create comparable systems independent of scale through the generation of a set of non-dimensional Pi terms [4]. The Pi terms are generated through consideration of influential experimental parameters and are held constant from one system to the other, regardless of scale. Morton first selected relevant experimental parameters and then developed the non-dimensional Pi terms. By assuming geometric similarity between two systems and by assuming the use of homogeneous materials in both systems, Morton arrived at a set of scaling relations. It was shown that strain rate effects cannot be scaled. Morton's experimental work demonstrated that the scaling relations (Table 8) used were valid for elastic deformation. Once plastic deformation occurs, a size effect correlated with absolute specimen size was observed: smaller specimens are stronger. Morton also observed that the duration of impact scaled to within  $\pm 10\%$  with the impact duration of smaller specimens being shorter.

Qian *et al* [5] also considered the scaling of composite materials subject to dynamic loading, but used a different approach. To create a set of scaling relations, they examined the differential equations governing the dynamic impact event assuming geometric similarity. The scaling relations that they arrived at were the same as those Morton arrived at using the Buckingham Pi theorem. To validate their set of scaling relations, Qian *et al* used a gas gun to conduct an

experimental study using laminated carbon epoxy plates with strain gages attached. Impactor speeds used by Qian *et al* on their laminated specimens were 4.57, 12.2, 18.3 and 24.4 m/s. Their experimental study showed that the scaling relations (Table 8) generated and implemented were valid for elastic deformation. Once plastic deformation is present, the scaling relations do not hold. Swanson [6, 7] also concluded that scaling with plastic deformation was damage mode dependent. Delamination showed a size dependence that was consistent with fracture mechanics, with smaller specimens being stronger. Fiber breakage did not show a dependence on size, only a dependence on the applied stress.

Several studies into composite scaling have been conducted. Sutherland *et al* [8] conducted drop weight impact testing using the scaling laws from Morton applied to low fiber volume glass polyester composites. The scaling relations worked well for the elastic deformation, but did not apply for plastic deformation as a size effect was observed with smaller specimens being stronger. Sutherland *et al* also concluded that the onset of delamination followed a fracture mechanics model and it scales well with specimen size [9]. Simitses [10, 11] applied the governing equation similitude approach to cylindrical bending of orthotropic composite plates subject to elastic loads with success. Jackson *et al* [12] applied the Buckingham Pi theorem to flexural and tensile testing of composite beams. They found that the elastic response did not exhibit a scaling effect, but that a significant strength scale effect exists with larger specimens being weaker. Viot *et al* [13] applied the scaling relations to drop weight impact testing on composite plates and concluded that the scaling relations from the similitude approach did indeed work well for elastic loading, but cannot be used to predict sudden material failure from delamination. Carillo *et al* [14] applied the scaling relations from geometric similitude to fiber metal laminates subject to low velocity impacts and found the scaling relations apply well for

elastic impacts, meaning a scaling effect was not present. Christoforou and coworkers [15] proposed that similar systems subject to low-velocity impact could be created by ensuring three non-dimensional parameters to be constant between systems. They argued that the scaling relations used by others in the past involving geometric similarity were merely a special case of their proposed scheme.

From the two approaches used by Morton and by Qian *et al*, it is generally possible to scale the displacements, forces and strains during impact, but not the damage that may result [16]. Based upon the work performed by Morton [2] using dimensional analysis (Buckingham’s Pi theorem) and Qian *et al* [5] using governing equations, a set of relevant scaling parameters and their relation to the scale factor ( $\lambda$ ) exist for impact loaded fiber reinforced composites. Those parameters and their relation to the scale factor are presented in Table 8. Derivation of the Table 8 results based upon Morton’s work is in Appendix C.

Table 8. Important scaling parameters and their associated scaling.

<b>Parameter</b>	<b>Scaling Applied</b>
Specimen Length	$\lambda$
Specimen Width	$\lambda$
Specimen Thickness	$\lambda$
Specimen Deflection	$\lambda$
Impactor Velocity	Constant
Impactor Diameter	$\lambda$
Impactor Mass	$\lambda^3$
Impact Energy	$\lambda^3$
Time	$\lambda$
Force	$\lambda^2$
Strain Rate	$1/\lambda$
Bending Stiffness	$\lambda$

## 2.2 Scaling Limitations

Fiber reinforced composites are heterogeneous in their nature as fibers with high stiffness along their length are bonded with a less stiff matrix material. Complete scaling of composite materials would involve the scaling of the microstructure as well as the macrostructure. Due to the cost and impracticality of scaling the microstructure of composite materials, it is often not included in scaling schemes. Scaling of the macrostructure however, is practical in some respects, but not all. Scaling of fiber reinforced composites through the thickness direction is not as straight forward as scaling in the in-plane directions [17]. With in-plane geometric scaling, the specimen is simply cut to size and/or the test area of the fixture used is adjusted to accommodate the scaling scheme. This approach does not work well for the thickness direction as it is difficult to uniformly alter the thickness without affecting some of the remaining specimen structure and performance [18]. Scaling could be attempted prior to the fiber-matrix fusion by altering the thickness of each ply. Attempting to control the thickness of each ply is not practical as each ply is made up of individual fibers. For laminated composites, there are two approaches for scaling specimen thickness by changing the number of fiber plies used: (1) ply-level scaling and (2) laminar scaling. Ply-level scaling involves stacking plies of like orientations next to one another as the scale factor increases. For example, consider the composite laminate  $[0/45/90]$ . To scale in the thickness direction using ply-level scaling, the new configuration would be  $[0_\lambda/45_\lambda/90_\lambda]$ . In laminar scaling, the base configuration is repeated, i.e.  $[(0/45/90)_\lambda]$ . Though there is a difference, neither of the two can be claimed to be the true scaling.

Beyond scaling of the composite specimen structure, scaling of the strain rate dependence is problematic. The Buckingham Pi scheme used to develop the impact scaling relations of

Table 8 does not account for material changes that are strain rate dependent. Several composite materials have demonstrated that the material properties change as a result of the loading rate [2,19]. The scaling scheme presented here cannot account for the strain rate sensitivity of composite materials across scales as the strain rate sensitivity generates a new Pi term in the Buckingham Pi scheme. In order to satisfy the new condition across scales, the previously established relation that time scales with  $\lambda$  would be conflicted. As a result, strain rate sensitivity cannot be accounted for through scaling based on the Buckingham Pi theory. Although the effects of strain rate on material properties cannot be scaled the strain rate itself can be scaled by  $1/\lambda$ .

### **3. Experimental Techniques**

The relationships outlined in Table 8 were applied to the Gas Assisted Horizontal Impactor (GAHI), which uses gas to propel a projectile through a guide tube and into a steel enclosure housing a test specimen to be impacted from the out-of-plane direction. The GAHI experimental setup with fringe projection applied as described in Section 1, was used to capture the out-of-plane displacement during loading. The experimental setup is displayed in Figure 14. An algorithm in MATLAB developed by Heredia and Patterson [20,21] and described in Section 1 was used to extract the out-of-plane deformation information from the images.

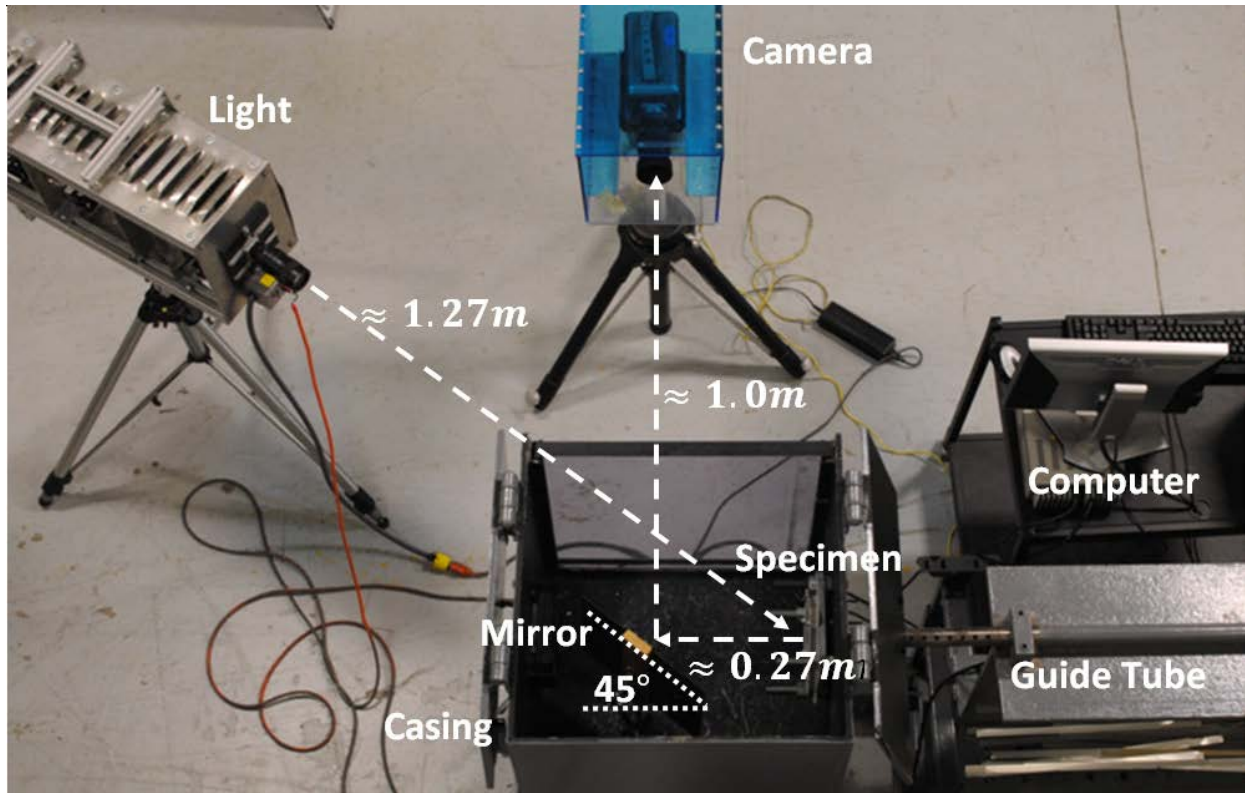


Figure 14. Image of the GAHI experimental setup.

The GAHI in conjunction with fringe projection to measure out-of-plane displacement was used to experimentally consider size effects that may be associated with composite plates composed of orthogonal woven E-glass fabrics with an SC-15 matrix. Scaling factors of  $\lambda = 3, 5$  and 10 were used to scale specimens and the associated experimental setup in this study. To accommodate the scaling relations outlined in Table 8, projectiles of differing mass and diameter were used. For each scale factor, a different testing configuration was used and the details of those configurations are outlined in Table 9. (The test configurations for  $\lambda = 3, 5$  and 10 correspond to the GAHI test configurations A, B, and C from Table 3 of Section 1.) To scale the specimen thickness, the number of woven E-glass plies used in each specimen was matched with the scale factor. Additional experimental details are in Table 16 of Appendix C.

Table 9. Scaled test parameters and associated testing information.

<b>Scale Factor (<math>\lambda</math>)</b>	<b>3</b>	<b>5</b>	<b>10</b>
<b>Specimen Test Diameter</b>	76.2 mm (3")	127 mm (5")	254 mm (10")
<b>Specimen Thickness</b>	3 plies 2.01 mm (0.0793")	5 plies 3.12 mm (0.1229")	10 plies 6.07 mm (0.239")
<b>Projectile Diameter</b>	3.81 mm (0.15")	6.35 mm (0.25")	12.7 mm (0.5")
<b>Projectile Mass</b>	0.916 g	4.116 g	33.629 g
<b>Test Frame Rate</b>	110,019 fps	88,050 fps	52,044 fps
<b>Images Captured During Projectile Loading Sequence</b>	<7	<8	<11

For each of the three scales,  $\lambda = 3, 5$  and  $10$ , tests were performed at five separate projectile velocities, 50, 65, 80, 95 and 110 m/s. Projectile velocities were selected for testing based upon the physical limitations of the experimental setup. The minimum velocity was determined based upon the minimum pressure required to drive the  $\lambda = 3$  projectile from its resting position and through the guide tube. The upper limit of the projectile velocity range was restricted by the amount of damage generated in test specimens. Severe damage to the non-impact surface of the test specimen will cause the projected fringes on the non-impact surface to be obscured from debris and severe damage during testing. When this occurs, out-of-plane deformation information is not extractable from the recorded images. In trials, sufficient damage to obscure fringe projection measurements occurred for impacts from projectiles traveling above 120 m/s. To examine scaling effects, test results conducted at different scales, but at the same projectile velocity were compared as according to Table 8.

Test specimens were placed in test fixtures with circular boundaries that were assumed to be fully clamped. The test fixtures associated with  $\lambda = 3$  and  $5$  have eight equally spaced clamping bolts securing the specimen between two 15.9 mm (5/8") steel plates. The clamping

bolts are arranged in a 101.6 mm (4”) and 165.1 mm (6.5”) diameter circles for the respective  $\lambda = 3$  and 5 test fixtures. The  $\lambda = 10$  test fixture includes 12 equally spaced clamping bolts arranged in a 292.1 mm (11.5”) circle around the test area. Four of the clamping bolts were 19.1 mm (3/4”) in diameter while the remaining bolts were 6.35 mm (1/4”) diameter. All of the bolts used in the  $\lambda = 3$  and 5 test fixtures were 6.35 mm (1/4”) diameter bolts.

The accuracy of each of the three test configurations for  $\lambda = 3, 5$  and 10 outlined in Table 9 was evaluated. This was performed by measuring the dimensions of cone of known dimensions. The dimensions of the cone as measured by fringe projection are compared against established values for the dimensions of the cone in Table 10.

Table 10. Accuracy measurements and quantification for the three GAHI testing configurations of Table 9.

		Cone Height	Cone Radius X-Direction	Cone Radius Y-Direction
GAHI Test Configuration	Established Value (mm)	9.81	19.90	19.90
$\lambda = 3$	Fringe Projection Measured Value (mm)	9.48	19.76	19.61
	Percentage Difference	3.36	0.70	1.46
$\lambda = 5$	Fringe Projection Measured Value (mm)	9.64	20.19	19.62
	Percentage Difference	1.73	-1.46	1.41
$\lambda = 10$	Fringe Projection Measured Value (mm)	9.36	20.20	19.60
	Percentage Difference	4.59	-1.51	1.51

## 4. Experimental Results

### 4.1 Displacement Histories

Fringe projection was used to measure the out-of-plane displacement histories from impact testing with the GAHI. The displacement histories at the impact point were extracted from the full-field out-of-plane contour maps from each image of the impact event. Figure 15 shows the unscaled peak displacement histories measured on the non-impact surface for the 65 m/s test cases. All of the displacement histories from GAHI testing for  $\lambda = 3, 5,$  and  $10$  show two peaks. The first peak is associated with the impact of the projectile on the specimen. The second peak is attributed to the effect due to subsequent wave propagation and vibration prior to the composite plate rebounding from the projectile loading (see Section 1, 5.4 for details).

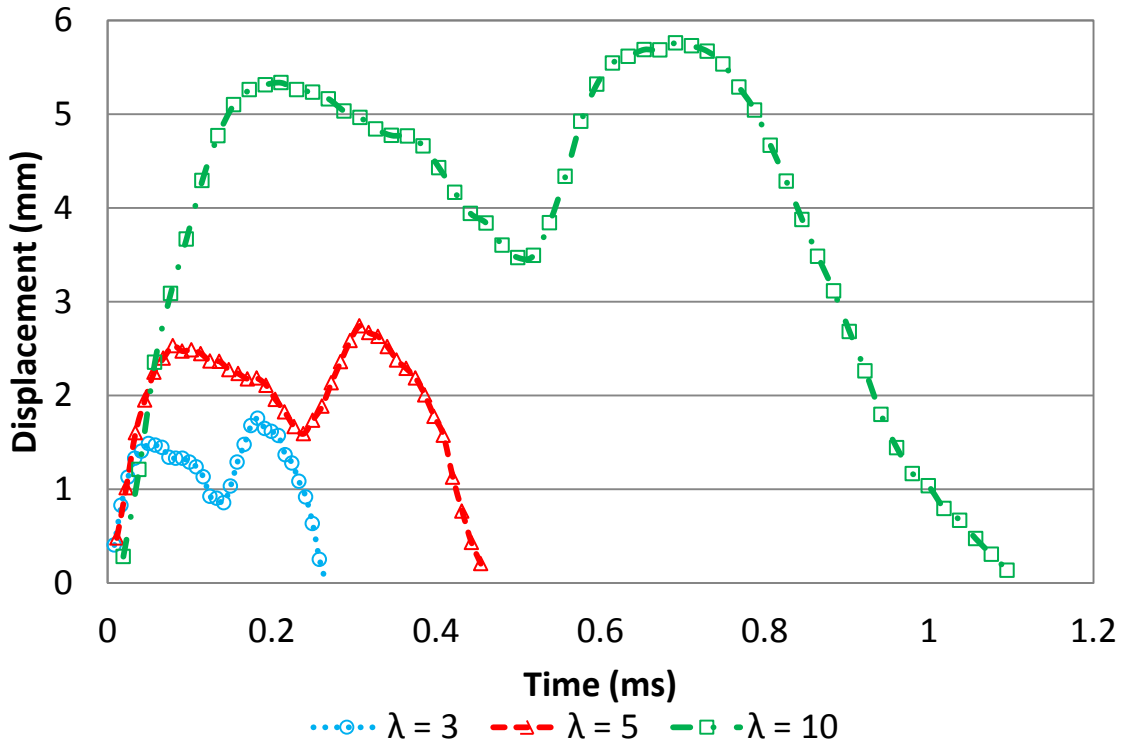


Figure 15. Unscaled displacement histories from 65 m/s projectile impacts for  $\lambda = 3, 5,$  and  $10$ .

To scale the displacement histories, the displacement and the time values for the impact event were divided by the associated scaling factor. For the scaling featured in Figure 16,  $\lambda = 3$  was taken as the base scale, thus no computations were applied to the  $\lambda = 3$  data sets. The time and displacement values for the  $\lambda = 5$  data set were divided by  $(5/3)$  to arrive at a scaled data set with respect to the  $\lambda = 3$  data. The  $\lambda = 10$  data points were divided by  $(10/3)$  to obtain a scaled data set with respect to the  $\lambda = 3$  data. Figure 13 shows good agreement among the three scales in the early stages of impact, likely within the elastic range. As time elapses, the discrepancy among the three scales increases. By the time the out-of-plane displacements for each of the three scales reaches zero again, the differences become more obvious with  $\lambda = 3$  having the shortest duration of displacement followed by  $\lambda = 5$  and then by  $\lambda = 10$ . Similar observations can also be concluded for all other velocities.

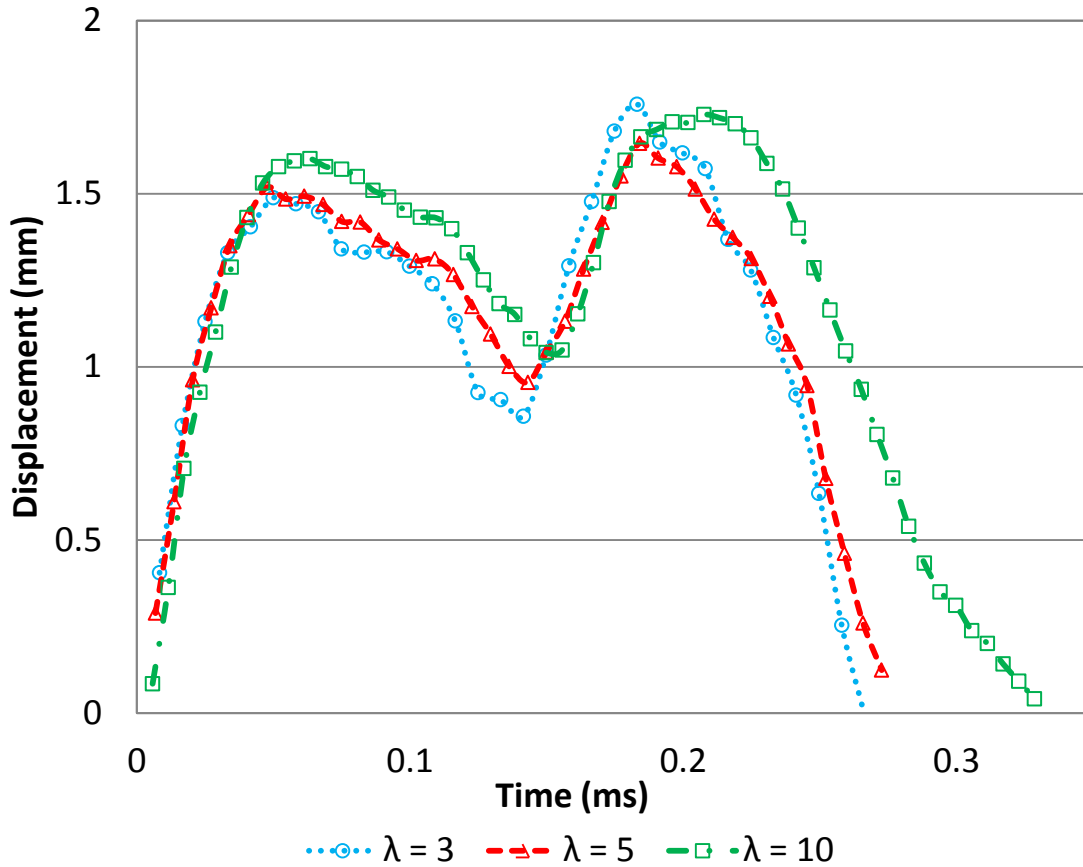


Figure 16. Scaled displacement histories for 65 m/s impact tests.

As shown in Figure 17, the three scaled displacement histories under the same impact velocity tend to group together. As the impact velocity increases, the magnitude of the displacements associated with each grouping increase and the differences among the the three scales for a given projectile velocity increases. This is especially true when the time approaches the end of out-of-plane displacement in the direction of loading. All the  $\lambda = 10$  cases, represented by squares, end on the far right of the diagram, all the  $\lambda = 5$  cases, represented by triangles, end left to squares while all the  $\lambda = 3$  cases, represented by circles, end even further left.

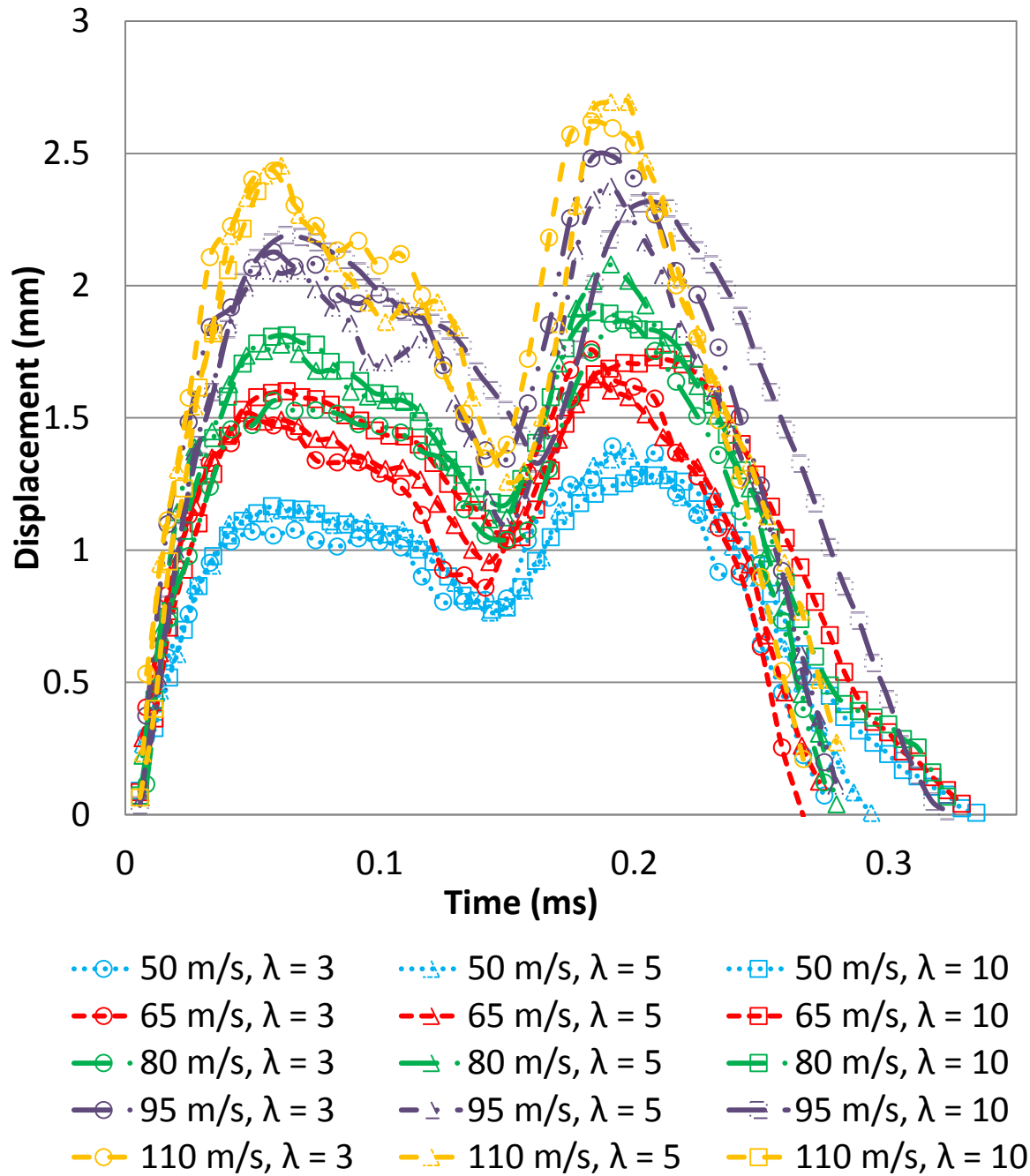


Figure 17. Scaled out-of-plane displacement histories as measured from the non-impact surface.  
 \*Significant damage to the non-impact specimen surface resulting in debris interference with the measurement for the 110 m/s,  $\lambda = 10$  test case.

## 4.2 Damage Modes

Although the displacement histories compare well when considering scaling, the damage to the specimens does not. The damage modes present include delamination (dl), internal matrix cracking (imc), impact surface matrix cracking (ismc), non-impact surface matrix cracking (nsmc) and at higher test velocities, impact surface fiber breakage (isfb) and non-impact surface fiber breakage (nsfb). Based upon the scaling scheme utilized, for a given projectile velocity, the behavior of the composite specimen subject to impact should be similar between the scales with differences being in terms of magnitude. With respect to damage, larger specimens exhibited more advanced modes for a given projectile velocity, a factor for which scaling utilized does not account.

Table 11 summarizes the damage modes in tested specimens. Under the same scale, the number of damage modes increases with the impact velocity. Similarly, under the same impact velocity, the number of damage modes increases with scale. The increase in damage modes with impact velocity seems to result from the increase in impact energy that accompanies an increase in impact velocity. The advancement of the degree of damage with increasing size demonstrates the presence of a size effect.

Table 11. Damage modes in test specimens.

<b>Projectile Velocity (m/s)</b>	<b>50</b>	<b>65</b>	<b>80</b>	<b>95</b>	<b>110</b>
<b><math>\lambda = 3</math></b>	dl	dl, imc	dl, imc	dl, imc, smc	dl, imc, ismc
<b><math>\lambda = 5</math></b>	dl, imc	dl, imc	dl,imc, ismc	dl, imc, ismc	dl, imc, ismc, isfb
<b><math>\lambda = 10</math></b>	dl, imc	dl,imc, ismc	dl,imc, ismc	dl, imc, ismc, isfb	dl, imc, ismc, isfb, nsmc, nsfb

dl = delamination, imc = internal matrix cracking, ismc = impact surface matrix cracking, isfb = impact surface fiber breakage, nsmc = non-impact surface matrix cracking, nsfb = non-impact surface fiber breakage

### 4.2.1 Delamination Area

For the specific damage mode of delamination, the delamination area was measured and compared across scales in Table 12. The areas in Table 12 indicate that the delamination area does not coincide with the scaling used. Smaller specimens have smaller delamination areas than their larger contour parts. The ratio of the delamination area across scales does not coincide with the scaling of the test specimen area,  $\lambda^2$ . The ratios of the delamination area for the  $\lambda=5$  and  $\lambda=10$  tests compared to the  $\lambda=3$  tests (Table 12) are higher than 2.78,  $(5/3)^2$  for  $\lambda=5$  and 11.11,  $(10/3)^2$  for  $\lambda=10$  with the  $\lambda=10$  tests having a greater degree of discrepancy, indicating that the larger specimens have disproportionately larger delamination areas.

Table 12. Delamination area ( $\text{cm}^2$ ) and the ratio of the delamination areas across scales.

<b>Projectile Velocity (m/s)</b>	<b><math>\lambda = 3</math></b>	<b><math>\lambda = 5</math></b>	<b><math>\lambda = 10</math></b>	<b><math>\lambda = 5 / \lambda = 3</math></b>	<b><math>\lambda = 10 / \lambda = 3</math></b>
<b>50</b>	0.24	1.25	3.39	5.17	14.01
<b>65</b>	0.35	2.52	11.90	7.13	33.74
<b>80</b>	0.63	3.19	14.42	5.06	22.91
<b>95</b>	1.02	4.32	25.77	4.24	25.31
<b>110</b>	1.85	5.73	39.22	3.10	21.18

### 4.3 Strain Rates

Fringe projection was also used to evaluate the strain rate of the non-impact surface of the composite specimen. This was performed by evaluating the length of the non-deformed and deformed viewing surfaces with the progression of time. Fringe projection is only capable of detecting out-of-plane deformation information. Points along the specimen surface cannot be specifically tracked with respect to their motion in the in-plane direction. To try and mitigate the discrepancies between actual strain and the measurable strain due to changes in the gage length in the in-plane direction that cannot be detected by fringe projection, the radius of the plate was used as the gage length. The fixed plate boundary conditions ideally restricts motion on one end

of the gage while in-plane motion at the other end of the gage should be minimal as the other end corresponds to the impact point on the non-impact specimen surface.

To determine the strain rate from fringe projection, strains associated with the first three to four images of impact were used to generate a strain history. After the first three to four data points, the strain history becomes increasingly non-linear. A linear least squares curve fit was applied to the points of the strain history with the slope of the curve fit line being the strain rate. The results are given in Table 13. Additional information concerning the evaluation of the strain rates is contained in Appendix D. The differences in strain rate exhibited in Table 13 for the same projectile velocity can be attributed to increases in specimen thickness influencing the measurements of the strain rates taken from the non-impact surface.

The strain rate values calculated are gage length dependent as would be the strain since the loading is in the out-of-plane direction and a deformation gradient is present. As with a strain gage, the strain from fringe projection is being averaged over the length of the gage. Averaging the strain over a more inclusive field of strain values will drive down the measured strain compared to measurements occurring over a small segment near the region of greatest out-of-plane loading. The effect of gage length on the measured strain was considered for the  $\lambda = 10$  test cases. The decreasing strain rates associated with increasing gage lengths are portrayed in Figure 18.

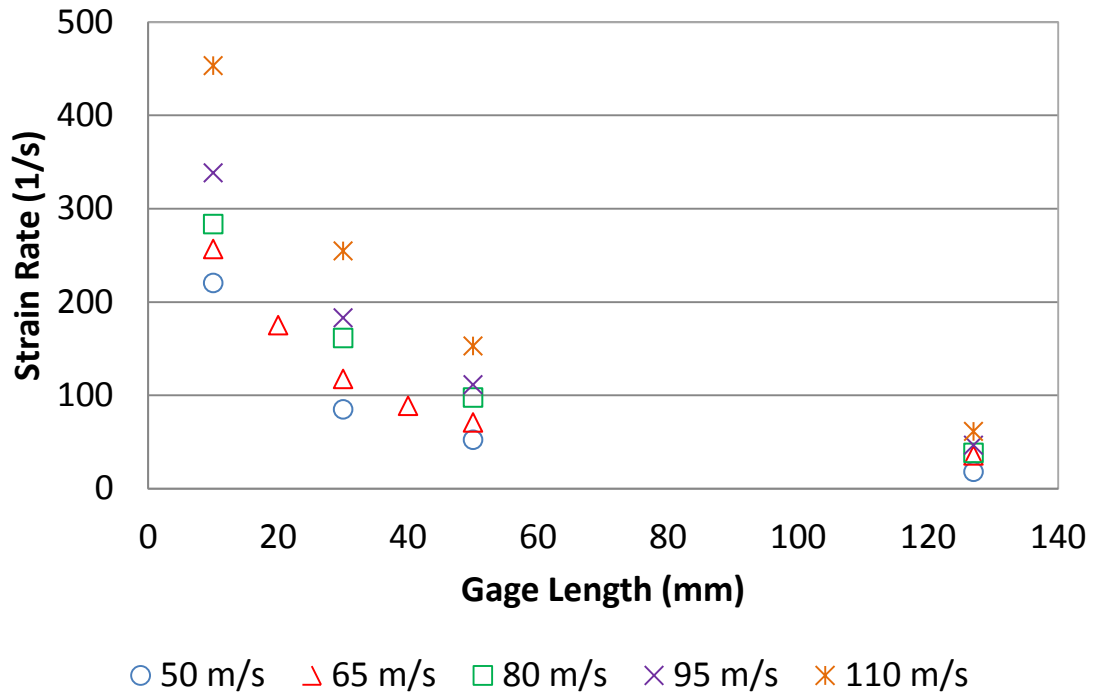


Figure 18. Strain rates as a function of gage length for the  $\lambda = 10$  test cases.

As previously noted, the effects of strain rate sensitivity of materials cannot be accounted for in the scaling scheme utilized, but the magnitude of the strain rate can be. The base units of the strain rate are  $s^{-1}$ . Given that the time parameter varies with  $\lambda$ , the strain rates should be multiplied by  $\lambda$  to account for the scales based upon the scaling employed. Multiplying the  $\lambda = 5$  set by  $(5/3)$  and the  $\lambda = 10$  set by  $(10/3)$ .

Table 13. Strain rates of the composite plates as obtained by fringe projection without and with an attempted account for scale.

Strain Rates ( $s^{-1}$ )	Unscaled			Scaled	
Projectile Velocity (m/s)	$\lambda = 3$	$\lambda = 5$	$\lambda = 10$	$(\lambda = 5) \times (5/3)$	$(\lambda = 10) \times (10/3)$
50	38.3	28.3	17.9	47.2	59.7
65	62.9	69.8	35.4	116.3	118
80	99.5	90.9	38.1	151.5	127
95	140	141.9	49.5	236.5	155.3
110	174.8	164.2	61.3	273.7	204.3

#### 4.4 Impact Based Bending Stiffness

A load-displacement relation of each impact test was generated from the measurements by fringe projection. The impact based bending stiffness was then evaluated for each test case by curve fitting the sequence of the displacement history from the onset of impact to the initial peak displacement using a third order polynomial. Second derivatives of the curve fit generated polynomial were evaluated to obtain the force-displacement relation for each test. The impact based bending stiffness would then be obtained from the first derivative of the curve fit force-displacement relation. To arrive at the scaled impact based bending stiffness, the calculated impact based bending stiffness values were divided by the associated scaling factor. Since the data set for  $\lambda = 3$  was selected to be the base, the impact based bending stiffness values for  $\lambda = 5$  were divided by  $(5/3)$  and the values for  $\lambda = 10$  were divided by  $(10/3)$ . (Section 3 of this thesis takes a closer look at the evaluation of the impact based bending stiffness).

Table 14. Scaled impact based bending stiffness (kN/mm) values.

	50 m/s	65 m/s	80 m/s	95 m/s	110 m/s
$\lambda = 3$	0.218	0.067	0.940	0.148	0.128
$\lambda = 5$	0.525	0.215	0.447	0.260	0.390
$\lambda = 10$	0.789	0.753	0.622	0.102	0.132

## 5. Discussions

### 5.1 Pi Terms

The scaling scheme applied in this experimental investigation is based on the relations outlined in Table 8, which come from the application of dimensional analysis to impact events. In the application of the Buckingham Pi theorem, Pi terms must be selected and held constant

across scales through the use of scaling factors. The Pi terms are composed of the parameters that construct the event that is being considered across scales. The Pi terms are arranged such that the units of the selected parameters eliminate one another, resulting in non-dimensional Pi terms. Additional information on the use of Buckingham Pi theorem can be found in Appendix C.

Table 15. Computation of Pi-Terms across scales associated with 65 m/s projectile impacts.

Pi Term	$\lambda = 3$	$\lambda = 5$	$\lambda = 10$
$\pi_1 = z\lambda/h\lambda$	$\pi_1 = \frac{1.48}{2.01} = 0.74$	$\pi_1 = \frac{2.53}{3.12} = 0.81$	$\pi_1 = \frac{5.34}{6.07} = 0.88$
$\pi_2 = l\lambda/h\lambda$	$\pi_2 = \frac{76.2}{2.01} = 37.91$	$\pi_2 = \frac{127}{3.12} = 40.71$	$\pi_2 = \frac{254}{6.07} = 41.85$
$\pi_3 = w\lambda/h\lambda$	$\pi_3 = \frac{76.2}{2.01} = 37.91$	$\pi_3 = \frac{127}{3.12} = 40.71$	$\pi_3 = \frac{254}{6.07} = 41.85$
$\pi_4 = D_{imp}\lambda/h\lambda$	$\pi_4 = \frac{3.81}{2.01} = 1.90$	$\pi_4 = \frac{6.35}{3.12} = 2.04$	$\pi_4 = \frac{12.70}{6.07} = 2.09$
$\pi_5 = E_{imp}/E$	$\pi_5 = \frac{140}{23.62} = 5.93$	$\pi_5 = \frac{140}{23.62} = 5.93$	$\pi_5 = \frac{140}{23.62} = 5.93$
$\pi_6 = v$	$\pi_6 = 0.10$	$\pi_6 = 0.10$	$\pi_6 = 0.10$
$\pi_7 = v_{imp}$	$\pi_7 = 0.26$	$\pi_7 = 0.26$	$\pi_7 = 0.26$
$\pi_8 = \rho_{imp}/\rho$	$\pi_8 = \frac{7850}{1892} = 4.15$	$\pi_8 = \frac{7850}{1892} = 4.15$	$\pi_8 = \frac{7850}{1892} = 4.15$
$\pi_9 = \rho_{imp}V_{imp}^2/E$	$\pi_9 = \frac{7850(65^2)}{23.62 * 10^9} = 1.4 * 10^{-3}$	$\pi_9 = \frac{7850(65^2)}{23.62 * 10^9} = 1.4 * 10^{-3}$	$\pi_9 = \frac{7850(65^2)}{23.62 * 10^9} = 1.4 * 10^{-3}$
$\pi_{10} = tV_{imp}/h$	$\pi_{10} = \frac{(0.26)(65)}{2.01} = 8.41$	$\pi_{10} = \frac{(0.47)(65)}{3.12} = 9.79$	$\pi_{10} = \frac{(1.09)(65)}{6.07} = 11.67$

Table 15 presents the ten Pi terms selected by Morton [2] and their numerical values across the scales considered in this experimental study. Keeping each Pi term constant across the scales considered allows for the physical systems at each scale to be considered similar and thus a basis for comparison is generated. However, not all of the Pi terms in Table 15 remain constant across

scales despite attempts to make this occur. The calculation of  $\pi_1$  and  $\pi_{10}$  of Table 15 are based on the experimental results, not solely on the parameters where an attempt of control was made prior to conducting the impact test, thus the variation of  $\pi_1$  and  $\pi_{10}$  across scales can not be attributed exclusively to a an inability to control the scaling setup. The Pi terms that include  $\pi_2$ ,  $\pi_3$ , and  $\pi_4$  are a function of parameters controlled prior to testing with the common parameter being the specimen thickness. These Pi terms vary across the scales considered due to the limitations associated with scaling the specimen thickness. Given the specimen thickness of 2.01 mm for  $\lambda = 3$  scale, properly scaled thickness values for  $\lambda = 5$  and 10 would be 3.35 mm and 6.70 mm. The actual thickness values achieved for the  $\lambda = 5$  and  $\lambda = 10$  scales were 3.12 mm and 6.07 mm with the percentage differences from the properly scaled thickness values being 6.87 and 9.40 respectively. By scaling the specimen thickness through the alteration of the number of orthogonal woven roving plies used, the absolute thickness of the specimen is less than the desired scaled thickness values (in this case 3.35 and 6.70 mm) with differences between the actual and desired absolute thickness values increasing with increasing scale. Under loading, the underscaled value of the thickness will contribute to increases in stress with specimen size. In spite of efforts to hold all of the Pi terms constant for the three scales ( $\lambda = 3, 5,$  and 10), the adherence to the theoretical scaling outline was not strictly achieved and this contributes, however slightly, to the increased damage seen in specimens of increasing size.

## **5.2 Overall Displacement Histories**

From Figure 16, the three scaled displacement histories for impact velocity of 65 m/s are very similar to one another in terms of magnitude and trend in the very beginning of deformation. This observation is applicable to other experimental result for a given velocity as shown in Figure 17. The slight variability between scaled displacement histories for a given

projectile velocity can, to some degree, be attributed to variability between test specimens and the experimental means employed. Such variability may be due to specimen defects causing variation in the magnitude of displacement, variation of the impact point with respect to the fiber weave of the specimen, selection of the impact point when extracting displacement histories, time shifts due to the first frame from fringe projection not corresponding exactly with the onset of deformation, small changes in projectile impact velocity from test to test, changes in the optical arrangement for fringe projection to accommodate the different size specimens, non-scaled microstructure, and inexact scaling of specimen thickness.

In light of the potential for variability between tests, a consistent trend is that the overall duration of deformation in the out-of-plane direction for the scaled  $\lambda = 10$  test cases is consistently longer than the durations for the scaled  $\lambda = 3$  and  $\lambda = 5$  test cases as demonstrated in Figures 16 and 17. The deformation histories of the scaled  $\lambda = 10$  test cases become out of synch with the scaled  $\lambda = 3$  and  $\lambda = 5$  test cases following the initial or first peak. The extended deformation duration with larger specimens was noted by Morton [2] as well. The longer impact durations for  $\lambda = 10$  specimens (approximately 0.05 ms) for a given projectile velocity are due to the greater degree of damage (Tables 11 and 12) in larger specimens, resulting in a decrease in stiffness of the specimen with time, which translates into an increase in impact duration beyond which scaling can account. The increase in total deformation duration with scale is not as pronounced in the comparison between the  $\lambda = 5$  and  $\lambda = 3$  durations, although it is present, but typically in the 0.01 ms range. This is due to the relatively greater increase in scale associated when comparing the  $\lambda = 10$  and  $\lambda = 3$  tests. Total durations for which the composite plate is displaced in the direction of loading exhibited a dependence on size with displaced durations

being 14-23.5% longer in the  $\lambda = 10$  tests and up to 6.5% longer in the  $\lambda = 5$  case, than in the  $\lambda = 3$  case.

The percentage difference among the magnitudes of the initial peaks of the scaled displacement histories is 16% or less. The difference is 10% or less for tests conducted at four of the five test velocities. Considering that the accuracy of the fringe projection method used to measure the peak displacements range from 3-5% depending on the GAHI configuration (Table 10) and the sources for variability and scaling limitations previously outlined, the aforementioned percentage differences are understandable, although the exact cause for their existence is difficult to determine. The scaled magnitudes of the initial peak displacements achieved by the  $\lambda = 10$  specimens are consistently greater than the magnitudes associated with the  $\lambda = 3$  or 5 specimens. The percentage differences between the initial peak displacements is within the realm of experimental variation, but the consistent trend of the  $\lambda = 10$  specimens having the greatest scaled magnitude is not consistent with that notion. The greater values achieved for the scaled initial peak displacements from the  $\lambda = 10$  tests can be attributed to: (1) inexact scaling (Table 15) with a bias towards thinner scaled specimens which in turn causes a reduction in stiffness with size and/or (2) the presence of a size effect with larger specimens being weaker stemming from a reduction in stiffness associated with the formation of damage. When comparing the initial peak displacements for the  $\lambda = 5$  and  $\lambda = 3$  tests for a given projectile velocity, the  $\lambda = 5$  displacements are often greater than the  $\lambda = 3$  results, but not consistently and not significantly when greater. As demonstrated through the comparison of the duration of the deformation histories, the lack of trend between the  $\lambda = 5$  and  $\lambda = 3$  results may simply be due to relatively small increase in scale as compared to  $\lambda = 10$  and  $\lambda = 3$ .

Two other points that define the double peak displacement histories are the trough and the second peak. The trough and the second peak are related to wave behavior, but the expectation would be that the magnitude of the trough and second peak would exhibit patterned behavior. The scaled data corresponding to the trough and the second peak, shown in Figures 15-17, do not demonstrate patterned behavior that would support the presence of a clear size effect with respect to the magnitude of the displacement of those two features.

### **5.3 Evaluation of the Projectile Loading Sequence Data**

Curve fitting the displacement history points beginning at the onset of impact to the first peak depicted in Figures 15-17 with a third order polynomial allows for the velocity, acceleration, and force histories associated with the plate to be calculated by taking the first and second derivatives of the curve fit derived function for the initial displacement history. Evaluating the second derivative of the curve fit polynomial results in the acceleration history and multiplying the acceleration history by the mass of the projectile results in the force history. For the 65 m/s test cases specifically, Figure 19 contains the scaled initial displacement history points, the scaled initial velocity history, and the scaled initial force histories. The frequency for which data is available is greater for the scaled  $\lambda = 10$  data sets than for the  $\lambda = 5$  and 3 data sets. This is due to the speed at which the unscaled test events occur, with the  $\lambda = 10$  tests being the longest in real-time duration and the  $\lambda = 3$  sets the shortest. The very first points in the three displacement histories in Figure 19 are all at slightly different times and levels of displacement. This is due to the moment the projectile impacts the specimen not corresponding exactly with the time at which the high-speed camera captures an image.

The scaled displacement histories depicted in Figure 19 generally agree across the three scales. The displacement of the  $\lambda = 10$  data set does have a slightly higher initial peak

displacement after scaling. The velocity histories for the initial loading sequence are portrayed in Figure 19 as well. No computations were required to arrive at the “scaled” velocity histories as the impact velocities were held constant as indicated in Table 8 for each scale considered. The velocity histories portrayed in Figure 19 are of the non-impact surface of the composite plate experiencing impact. For the  $\lambda = 3$  and 5 tests, the plate velocity is a little over 50 m/s near the onset of impact and decreases almost linearly to zero although a second order polynomial is being used to describe the velocity histories. For the  $\lambda = 10$  test case the plate velocity near the onset of impact is around 42 m/s with the decrease in velocity associated with increasing time demonstrating more of a quadratic relationship. The lower initial plate velocity associated with the  $\lambda = 10$  case is due to its relatively higher thickness which creates more compaction during impact and a longer time delay between the moment of impact and the observation of the impact event. The measured velocities for each of the three scales are below the impactor velocity of 65 m/s. This is caused by a combination the measurement occurring on the non-impact surface and the fact energy is not perfectly transferred from the projectile into motion of the plate in the out-of-plane direction.

The final sets of data presented in Figure 19 are the scaled force histories for the three scales. Since the displacement histories were curve fit with a third order polynomial, the acceleration and subsequently the force histories have a linear relationship with time. The force histories for the  $\lambda = 3$  and 5 tests are similar in trend, but they indicate a highly non-zero force being present prior to impact, which is not physically possible. The  $\lambda = 10$  force history is more realistic in that a near zero force occurs near the onset of impact. The differing trends of the force histories in Figure 19 do not provide sound support that they were successfully scaled. The discrepancies in the force histories can be attributed to the difficulties and errors associated with

curve fitting displacement histories with relatively few data points rather than the failure of the force histories to agree due to a size effect. Evaluating the second derivative of the non-perfect curve fits perpetuates the error present in applying a curve fit to the displacement histories. The force histories may or may not compare well to one another once scaled, but the perpetuation of the minor differences among the curve fit displacement histories with the computation of the force histories do not allow for such conclusions to be reached.

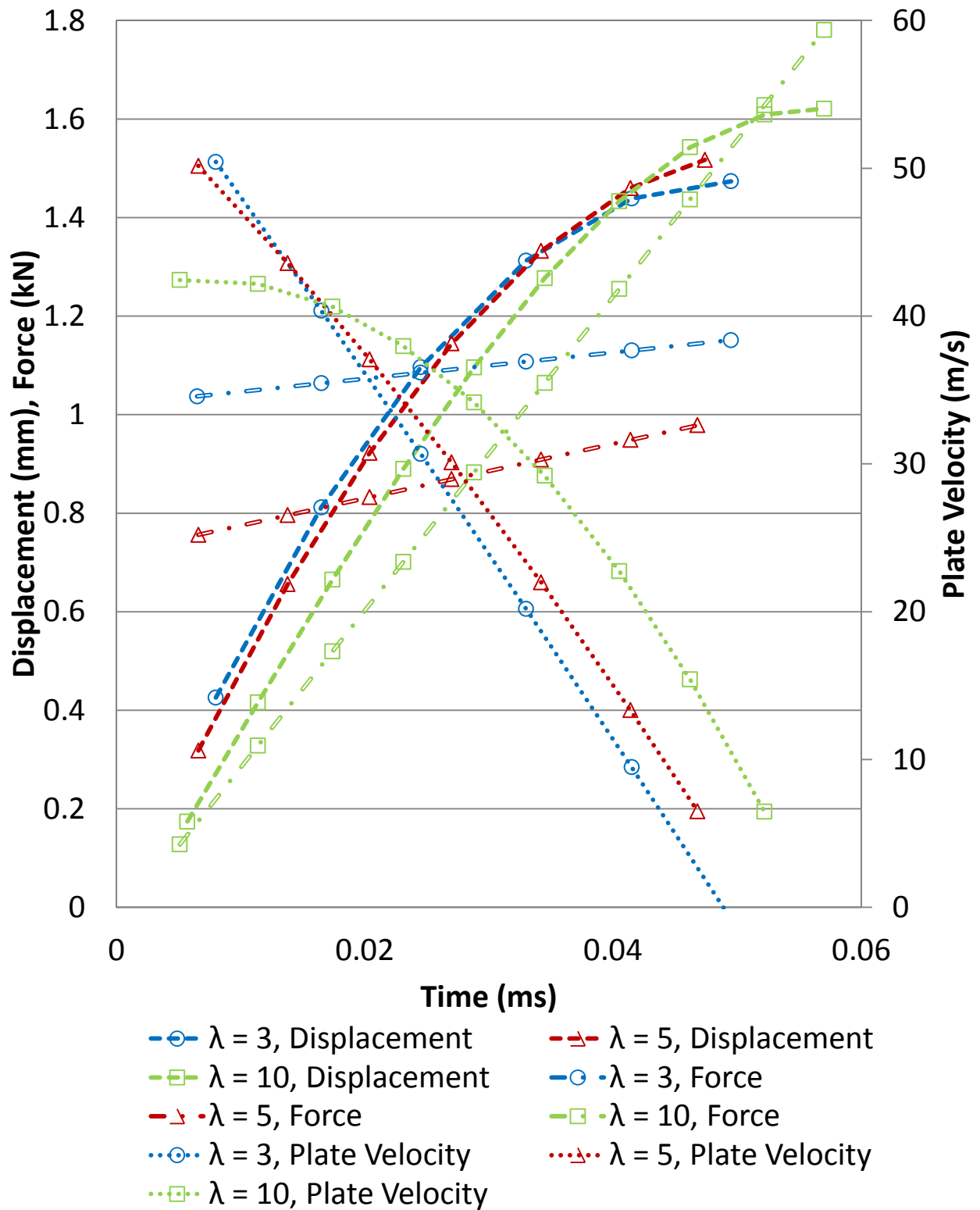


Figure 19. Scaled displacement, velocity, and force histories up to the initial peak displacement from 65 m/s tests.

#### 5.4 Scaling of Force Displacement Relations

The force displacement relations in Figure 20 contain the differences seen in the force histories of Figure 19, but are presented in a different form. From the slope of the linear portions of the three data sets in Figure 20, the scaled impact based bending stiffness values are 0.067, 0.2154, and 0.753 kN/mm for  $\lambda = 3, 5,$  and 10 respectively. For a given test velocity the scaled impact-based bending stiffness values should be the same, presuming a strain rate effect is not present. The inconsistencies between the computed data and the physical happenings are further illustrated in Figure 20, with the projected magnitude of the force associated with zero displacement being near 1.0 and 0.7 kN for the  $\lambda = 3$  and 5 test cases.

The scaled displacement histories, where the parameters output directly by the fringe projection method were merely divided by a constant, correlate well. The correlation among the data sets decreases when derivatives of a curve fit polynomial are used to generate the force history. This is not only illustrated in Figure 20, but in the variance among the impact based bending stiffness values of Table 14. The increase in the range of the results between the range of the scaled displacement histories and the scaled impact based bending stiffness results is due to the number of data points available during the initial loading sequence in conjunction with the method used to arrive at the impact based bending stiffness values. The number of data points available for the initial loading sequence is limited. The short initial loading duration limits the quality and quantity of the images captured from the high-speed camera. The number of attainable data points is limited as increases in the camera frame rate result in decreases in exposure time. At some point, the contrast in the image will become too low for the identification of the projected fringes, resulting in the quality of the images being poor. This places a limit on the achievable frame rate of the high-speed camera during testing.

The limited number of data points has a detrimental effect on the processing methodology used to compute the impact-based bending stiffness. Curve fitting can work quite well given a “sufficient number” of data points available to curve fit. In the application of fringe projection to drop weight impact testing, 80 data points were often available for the initial loading sequence of the test specimen and the variance in the impact based bending stiffness values was roughly 8%. For the  $\lambda = 3$  GAHI tests, roughly 5-6 data points were available for curve fitting. The result of having low data resolution is increased variability in the form of the curve fit polynomial from test to test. Changes in the form of the polynomial involve the magnitude and positivity of the leading coefficient for a term. Evaluating the derivatives of the curve fit polynomials amplifies the differences among the curve fit polynomials from test to test and contributes to the variance among the impact based bending stiffness values.

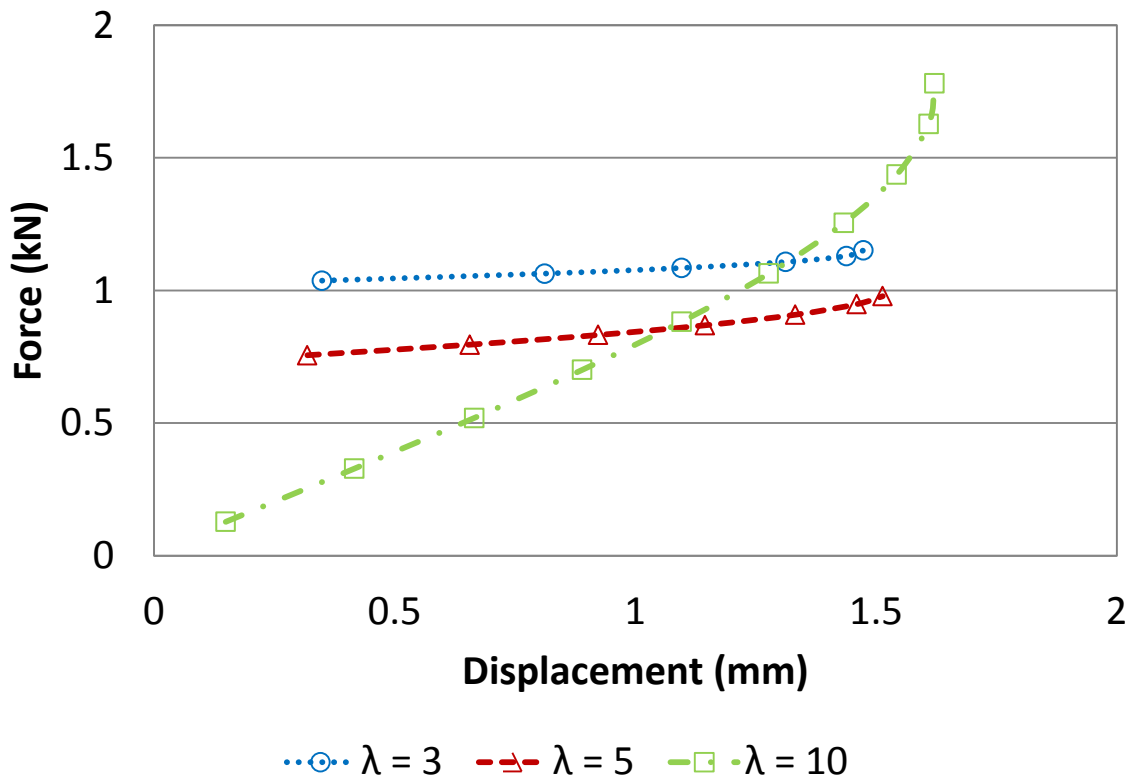


Figure 20. Scaled force displacement relations from 65 m/s tests.

## 5.5 Damage

Table 11 summarizes the damage modes in tested specimens. Under the same scale, the number of damage modes increases with the impact velocity. Considering size effects, under the same impact velocity, the number of damage modes increases with scale. The increase in damage modes with impact velocity is a result from the increase in impact energy that accompanies an increase in impact velocity. The increase in the degree of damage as the size increases suggests that a size effect is present, with specimens on smaller scales being more resistant to damage than their larger counterparts.

Quantitatively, the notion that smaller specimens are more damage resistant is supported in Table 12 as the delamination area increases with scale for every projectile velocity considered at a rate greater than the scaling associated with the test area of the specimen,  $\lambda^2$ . For the three scales of composite materials investigated, there are three layers with two interfaces for  $\lambda = 3$  specimens, there are five layers with four interfaces for  $\lambda = 5$  specimens and ten layers with nine interfaces for  $\lambda = 10$  specimens. Delamination can take place easily on the interfaces between layers and the ratio of the number of interfaces (1 : 2 : 4.5) is greater than the ratio of the scales (1 : 1.67 : 3.33). This indicates that increases in specimen thickness increase the surfaces with high potential for delamination beyond what scaling takes into account.

The specimen microstructure remained constant among the scales. The defects or weak points in the composite structure that serve as the catalyst for damage development were not scaled with  $\lambda$  because the underlying microstructure was not scaled. However, it is possible for the size of the defects to increase or decrease with  $\lambda$  despite the constant size of the microstructure, as the process (vacuum assisted resin transfer molding) to infuse the glass fibers with the matrix was altered minimally across scales. The advancement of damage modes with

specimen size suggests that the defects either increased or remained the same in size and their numbers increasing with scale.

As the damage modes evolve through delamination and matrix cracking during impact, more of the load must be supported by the fibers of the composite alone, resulting in the subsequent fiber breakage exhibited at larger scales for the 95 and 110 m/s impact velocities. The strength of fiber reinforced composites is largely based upon the strength of the fibers utilized and the fibers themselves are not immune from size effects. Glass fibers have demonstrated a size effect with longer fibers being weaker due to the greater potential for defects and damage in long fibers [22]. As noted, the diameter of the fibers was not scaled, but the number of fibers supporting the load should scale with  $\lambda$  because the thickness scaling applied is based upon the number of plies. Although fiber breakage is only present at larger scales it is not clear if this is a result of a size effect associated with the fibers themselves and/or the significant presence of damage in the form of delamination at larger scales requires the fibers of constant diameter across scales to be bear loads relatively greater than their counterparts at smaller scales. Based upon the damage modes and delamination area present in the composite test specimens, the scaling used cannot account for damage, thus a size effect is present with larger specimens being weaker.

## **6. Conclusion**

An experimental program was devised that incorporated and applied a set of scaling relations to composite materials for three scales,  $\lambda = 3, 5$  and  $10$ . The experimental program aimed to examine the existence of a size effect in fiber reinforced composites composed of woven E-glass fibers and an SC-15 matrix subject to out-of-plane impact. Out-of-plane impact was facilitated through the use of the gas assisted horizontal impactor and occurred at five

projectile velocities for each scale, 50, 65, 80, 95, and 110 m/s. The scaled test setup involved the use of fringe projection to measure out-of-plane displacements during impact. From the scaled displacement histories at the point of impact, no difference was observed in the elastic stage of impact-induced deformation. The displacement histories were used to calculate the velocity and force histories at the point of impact on the non-impact surface. Using the force displacement relation, scaled impact-based bending stiffness values were computed. Compared to the scaled displacement histories there was significant variation among the impact based bending stiffness values, demonstrating the limits of the applied measurement and data processing methods. The damage modes were more advanced in larger specimens. The delamination area demonstrated a size dependence on absolute size of the test specimen. Scaling can account for the elastic deformation experienced by the test specimens, but not the associated damage which indicates that smaller specimens are stronger.

## **APPENDICIES**

## Appendix C: Buckingham Pi Scaling

The Buckingham Pi theorem dictates that if a set of non-dimensional Pi terms that includes all of the influential system parameters are held constant from one system to the next, then the systems are physically similar. The influential parameters can be arranged in a physically meaningful mathematical expression describing the event, but the form of this expression need not be known. According to the Buckingham Pi theorem, the number of non-dimensional Pi terms ( $i$ ) required to describe a physical event is

$$i = n - k \quad (2.1)$$

Where  $n$  = number of influential parameters describing physical event  
 $k$  = number of fundamental units

The Pi terms are non-dimensionalized by considering the fundamental units of each of the influential experimental parameters. The selection of the influential parameters can be open to interpretation depending on the physical system in question. Using the fundamental units selected, it must be possible to equivocally rewrite the units of the influential parameters. Often times it is easiest to select the base units included in the system in question as the fundamental units. Base units typically include length,  $l$ , time,  $t$ , and mass,  $m$ . To illustrate the base units, consider the parameter force. Typically in the SI system force has the units of Newtons or (meters\*kilogram/(second<sup>2</sup>)), which in terms of the base units outlined is ( $m*l*(t^{-2})$ ). Often times many sets of Pi terms can be generated for a single physical system as there are many combinations of the influential parameters describing the event that can be used to non-dimensionalize the Pi terms.

Morton applied the Buckingham Pi theorem to carbon-epoxy beams subject to transverse low-velocity impact. He assumed that the test specimens were homogenous. The parameters of

interest or the output parameters were identified as transverse deflection ( $z$ ) and time ( $t$ ).

Considering the specimen, the parameters length ( $l$ ), width ( $w$ ), height( $h$ ), Young's Modulus ( $E$ ) Poisson's Ratio ( $\nu$ ), and density ( $\rho$ ) are influential to the impact response. With respect to the impactor, the parameters of influence include the impactor diameter ( $D_{imp}$ ), the impactor velocity ( $V_{imp}$ ), Poisson's Ratio of the impactor ( $\nu_{imp}$ ), Young's Modulus of the impactor ( $E_{imp}$ ), and the density ( $\rho_{imp}$ ) of the impactor. Together these were the 13 influential system parameters selected by Morton. The base units that the influential system parameters can be broken into are mass, length, and time. Recall that the number of Pi terms required is the difference between the number of influential system parameters and the fundamental units. Assuming the base units are the same as the fundamental units, as Morton did, then for Equation (2.1),  $n = 13$  and  $k = 3$ . Thus ( $i = 10$ ) ten Pi terms are needed to describe low-velocity impact of a beam. Morton selected the non-dimensional Pi terms to be

$$\begin{aligned}
 \pi_1 = z/h & \quad \pi_2 = l/h & \quad \pi_3 = w/h & \quad \pi_4 = D_{imp}/h & \quad \pi_{5j} = E_{imp}/E \\
 \pi_{6ji} = \nu & \quad \pi_7 = \nu_{imp} & \quad \pi_8 = \rho_{imp}/\rho & \quad \pi_9 = \rho_{imp}(V_{imp}^2)/E & \quad \pi_{10} = t(V_{imp})/h
 \end{aligned}
 \tag{2.2}$$

Let the experimental scale be denoted the model and the second scale be the prototype. For two systems to be similar, the Buckingham Pi Theorem requires that

$$(\pi_x)_{model} = (\pi_x)_{prototype}
 \tag{2.3}$$

If the linear geometric dimensions are scaled by  $\lambda$  from the model to the prototype, then

$$\begin{aligned}
 (\pi_1)_{model} &= z/h = (\pi_1)_{prototype} = z\lambda/h\lambda \\
 (\pi_2)_{model} &= l/h = (\pi_2)_{prototype} = l\lambda/h\lambda \\
 (\pi_3)_{model} &= w/h = (\pi_3)_{prototype} = w\lambda/h\lambda \\
 (\pi_4)_{model} &= D_{imp}/h = (\pi_4)_{prototype} = D_{imp}\lambda/h\lambda
 \end{aligned} \tag{2.4}$$

If the same materials are used for the test specimen and the impactor in the model and the prototype, then

$$\begin{aligned}
 (\pi_5)_{model} &= E_{imp}/E = (\pi_5)_{prototype} \\
 (\pi_6)_{model} &= \nu = (\pi_6)_{prototype} \\
 (\pi_7)_{model} &= \nu_{imp} = (\pi_7)_{prototype} \\
 (\pi_8)_{model} &= \rho_{imp}/\rho = (\pi_8)_{prototype}
 \end{aligned} \tag{2.5}$$

This accounts for eight of the ten Pi terms. Next examine

$$(\pi_9)_{model} = \rho_{imp} V_{imp}^2 / E = (\pi_9)_{prototype} = \rho_{imp} V_{imp}^2 / E \tag{2.6}$$

To satisfy the condition in Equation (2.6),  $V_{imp}$  must be constant between the model and prototype as  $\rho_{imp}$  and  $E$  are held constant between the model and prototype when the materials of the impactor and the specimen are the same between the systems.

The final condition comes from  $\pi_{10}$ , which is

$$(\pi_{10})_{model} = tV_{imp}/h \neq tV_{imp}/\lambda h = (\pi_{10})_{prototype} \tag{2.7}$$

To make  $(\pi_{10})_{model} = (\pi_{10})_{prototype}$ , time( $t$ ) must be multiplied by  $\lambda$  such that

$$(\pi_{10})_{model} = tV_{imp}/h = t\lambda V_{imp}/\lambda h = (\pi_{10})_{prototype} \tag{2.8}$$

Thus from Equation (2.8), time scales with  $\lambda$ .

To determine the scaling for the impactor mass let

$$mass_{imp} = \rho_{imp} * volume \quad (2.9)$$

Recall that  $\rho_{imp}$  is constant across the physical systems considered. Since the volume is comprised of three geometric parameters scaled by  $\lambda$ , the volume and subsequently the mass of the impactor for the prototype will be  $\lambda^3$  times greater than the mass of the projectile in the model.

$$(mass_{imp})_{prototype} = \rho_{imp} * (lengthparameter * \lambda)^3 \quad (2.10)$$

The impact energy ( $KE$ ) can be written as

$$KE = 1/2 * mass_{imp} * V_{imp}^2 \quad (2.11)$$

Since the impactor mass scales with  $\lambda^3$ , the impact energy will also scale with  $\lambda^3$  as  $V_{imp}$  is constant across scales.

For the force relation for the model, we have

$$(force)_{model} = mass_{imp} * acceleration_{imp} \quad (2.12)$$

Acceleration is the change in velocity per unit time. Using the fact that  $V_{imp}$  is constant between scales and that time scales with  $\lambda$  as established by Equations (2.7) and (2.8), the acceleration scales with  $1/\lambda$ . Thus from the relation of Equation (2.10) for the impactor mass and the relation that acceleration scales with  $1/\lambda$ , the result is

$$force_{prototype} = (\rho_{imp} * (lengthscale * \lambda)^3) * \left( acceleration_{imp} / \lambda \right) = force_{model} * \lambda^2 \quad (2.13)$$

From Equation (2.13), it is evident that the impact force varies with  $\lambda^2$  across scales.

## Appendix D: Fringe Projection and Strain Rate Evaluation

Fringe Projection is a full field measurement technique, therefore contour information about the composite plate subject to impact is available over the entire surface area included in the images captured during testing. This allows for plots to be developed that depict the out-of-plane displacement of the specimen surface as a function of position for a time step during the impact event. Combining several of these out-of-plane displacement plots for a given time step paints a picture of the plate behavior through the impact event. Charts that depict out-of-plane displacement as a function of position can be used to compute strain values experienced by the non-impact surface of the composite plate for a given time step as the necessary information (change in length of the plate and original length of the plate) are presented. Figure 21 provides an example of the fringe pattern on a test specimen during impact. Using several images like the one presented in Figure 21, an out-of-plane deformation vs. plate position chart can be constructed documenting the behavior of the plate through time as presented in Figure 22. The contour lines in Figure 22 run along the horizontal axis of the images captured during impact. The time duration for which the contour lines cover correspond to the time required to load the specimen to the peak displacement achieved from solely the projectile loading.

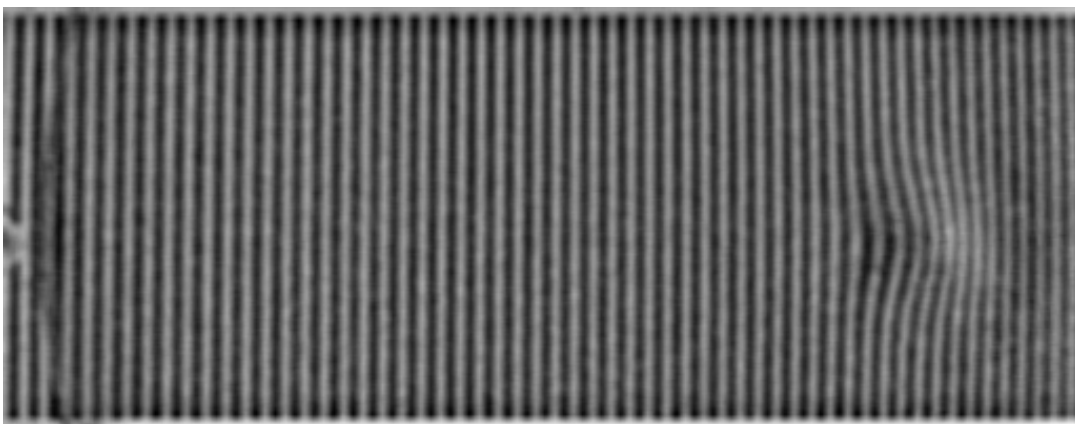


Figure 21. Enhanced image of the non-impact surface of a test specimen for the  $\lambda = 10, 95$  m/s test configuration with fringes captured at 0.038 ms into the impact event.

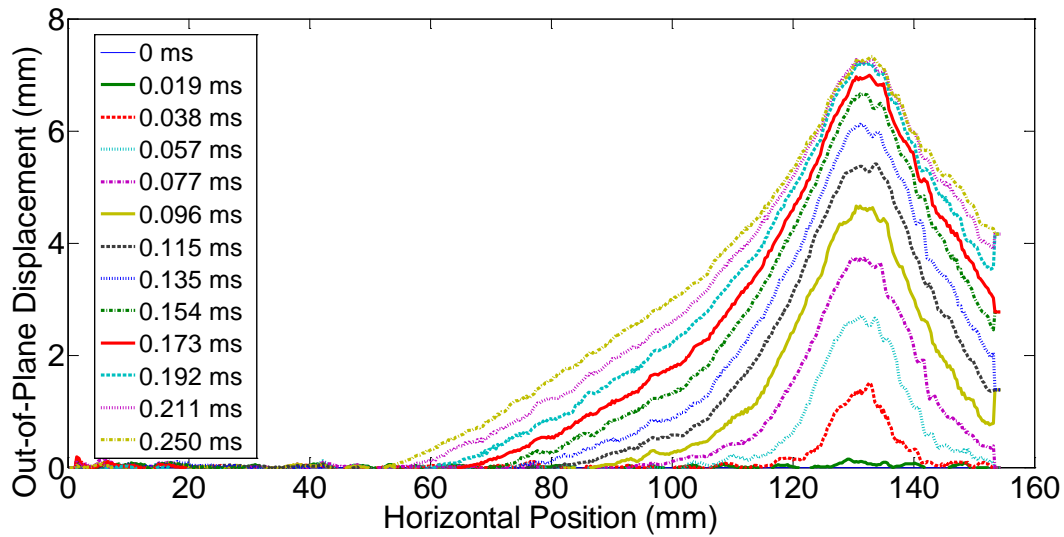


Figure 22. Out-of-plane displacement as a function of position across the specimen surface for the  $\lambda = 10, 95$  m/s test configuration.

To evaluate the strain, the undeformed length of the plate was measured from a chart such as Figure 22. Plate lengths were taken from the edge of the specimen to the point of impact, resulting in the radius of the test area being considered in the strain rate calculation. Only a portion of the specimen surface was captured during testing and the area captured was not varied with the scale factor. The point of impact and the fixture edge were captured at all scales. Table 16 provides information pertaining to the fringe projection setup, including the area captured across scales. To allow for comparison among the scales, the same relative portion of the plate should be considered. In essence, the idea is to scale the gage length across scales as if a strain gage were used. To measure the length of the composite plate as it experiences deformation, points were taken along a given curve and the distance between the points calculated to determine the deformed length of the plate.

Table 16. Additional testing information for the three sizes of specimens.

Scale Factor ( $\lambda$ )	3	5	10
Test Image Resolution	208 x 128	368 x 144	512 x 200
Test Area of Interest	60 mm x 40 mm	108 mm x 42 mm	160 mm x 63 mm
Fringe Pitch on Reference Plane	2.20 mm	2.186 mm	2.716 mm
Spatial Resolution	3.47 pixels/mm	3.42 pixels/mm	3.19 pixels/mm
Calibration Constant	0.4780 mm/rad	0.46581 mm/rad	0.4535 mm/rad

During the loading sequence the amount of strain accumulated between time steps is not constant. As the projectile impacts and deforms the specimen, the strain rate will decrease. The strain rate of interest occurs at the onset of loading. To provide a solid indication of the strain rate from test to test, the first three time steps were used in the calculation of the strain rate. The specific calculation of the strain rate was performed by generating a strain history and applying a linear curve fit to the data points with the slope of the line being the strain rate. This means that the strain rate is assumed to be constant over the first few time steps. An example of the curve fit strain points is Figure 23.

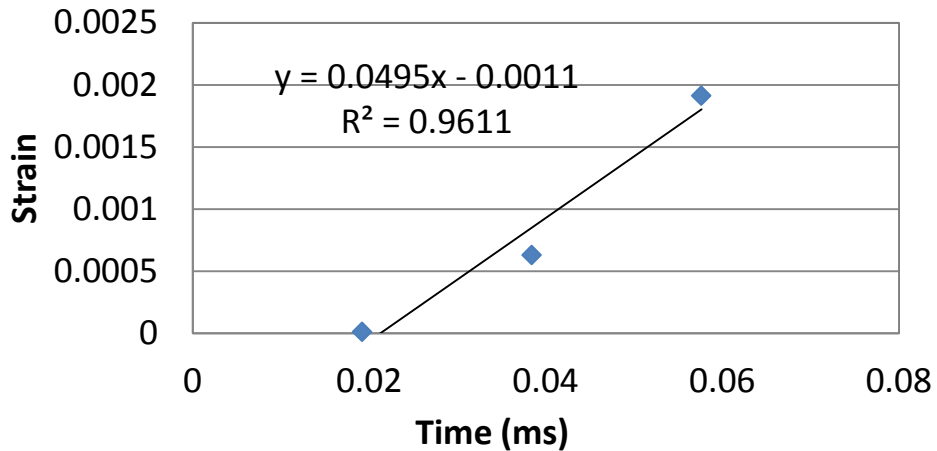


Figure 23. Abbreviated strain history for a  $\lambda = 10$ , 95 m/s impact test.

## **REFERENCES**

## REFERENCES

1. Duffy, T.A., Cheresh, M.C., Sutherland, S.H., “Experimental Verification of Scaling Laws for Punch-Impact-Loaded Structures, *International Journal of Impact Engineering*”, 2(1), 103-117, (1984).
2. Morton, J. , Scaling of Impact-Loaded Carbon-Fiber Composites, *AIAA J.*, 26(8), pp. 989–994. (1988)
3. Pintado, P., and Morton, J., “On the scaling of impact loaded composite beams”, *Compos Struct* 27 (4), pp. 357–365 (1994)
4. Buckingham, E., “On Physically similar systems; illustration of the use of dimensional equations”. *Phys Rev* 4 (1914)
5. Qian, Y., Swanson , S.R., Nuismer, R.J., and Bucinell, R.B. “An experimental study of scaling rules for impact damage in fiber composites”. *J. Composite Mater.* 24, pp. 559–570 (1990)
6. Swanson, S.R., “Scaling of Impact Damage in Fiber Composites from Laboratory Specimens to Structures”, *Comp. Struct.*, 25, pp. 249–255. (1993)
7. Swanson, S.R., “Mechanics of Transverse Impact in fiber Composite Plates and Cylinders”, *J. Reinforced Plastics and Comp.*, 12, pp.256-267, (1993)
8. Sutherland, L.S. and Soares, C.G., “Scaling of impact on low fibre-volume glass–polyester laminates”, *Compos Part A*, 38, pp. 307–317 (2007)
9. Sutherland, L.S. and Soares, C.G., “Impact characterisation of low fibre-volume glass reinforced polyester circular laminated plates”, *Int. J. Impact Eng.* 31, pp. 1–23. (2005)
10. Simitse , G.J., “Structural Similitude for Flat Laminated Surfaces”, *Composite Structures* 51, pp.191-194 (2001)
11. Simitse G.J., and Rezaeepazhand J., “Structural similitude for laminated structures”. *J. Composites Engng*, 3 7–8 (1993), pp. 751–765
12. Jackson, K.E., Kellas S., and Morton, J., “Scale Effects in the Response and Failure of Fiber Reinforced Composite Laminates Loaded in Tension and in Flexure”, *J. Comp. Mat.*, 26(18), pp. 2674–2705 (1992)
13. Viot, L. Ballere, L. Guillaumat and Lataillade, J. L., Scale effects on the response of composite structures under impact loading, *Eng Fract Mech* 75, pp. 2725–2736 (2008)

14. Carrillo, J.G., Cantwell, W.J., Scaling effects in the low velocity impact response of fiber-metal laminates, *Journal of Reinforced Plastics and Composites*, 27 (9), pp. 893-907 (2008)
15. Christoforou, A.P., and Yigit, A.S. Scaling of low-velocity impact response in composite structures. *Compos. Struct.* 91(3), pp.358–365 (2009)
16. Abrate, S., *Impact on Composite Structures*. Cambridge University Press. pp. 132-134 (1998)
17. Liu, D., Raju, D.D., and Dang, X., “Size Effects on Impact Response of Composite Laminates”, *International Journal of Impact Engineering*, 21(10), 837-854, 1998.
18. Liu, D., Raju, B.B., and You, J., “Thickness effects on Mechanical Joints of Composites”, *J. Composite Materials* 33 (1), 2-21, 1999
19. Weeks, C.A., Sun, C.T., “Modeling non-linear rate-dependent behavior in fiber-reinforced composites”. *Compos Science Technology*, 58, 603–611, (1998).
20. Heredia-Ortiz, M., “*Novel Developments of Moiré Techniques for Industrial Applications*”, *Doctoral Thesis, Sheffield, UK, University of Sheffield, (2004)*.
21. Heredia-Ortiz, M., and Patterson, E.A., “Location and Shape Measurement Using a Portable Fringe Projection System”, *Experimental Mechanics*, 45(3), 197-204, (2005).
22. Kies, J.A., “The strength of glass fibers and the failure of filament wound pressure vessels”, Naval Research Lab Report 6034, (1964)

## **Section 3: Evaluation of the Impact Based Bending Stiffness from Fringe Projection Applied to the GAHI**

### **Abstract**

Methods for evaluating the impact based bending stiffness from fringe project test results from DWIT and GAHI tests were considered. Results of the impact based bending stiffness from fringe projection for DWIT testing were compared to impact based bending stiffness values from the load cell. The impact based bending stiffness was evaluated from fringe projection displacement histories from GAHI testing using several methodologies. A single method was deemed better than the others considered and impact based bending stiffness values from GAHI testing are presented, but the results still lack the consistency desired.

### **1. Introduction**

The impact based bending stiffness from recent GAHI testing is desired. The impact based bending stiffness is evaluated by applying a linear curve fit to the linear portion of the force displacement plot. For fringe projection data, the generation of force displacement plots can attract inaccuracies from data processing methodologies as the direct output of fringe projection is displacement, and the force must be evaluated from the displacement data. To contrast, in testing involving the DWIT, where a load cell is present, force is the direct output and displacement must be computed. The application of numerical integration techniques required to generate a force history from a displacement history have demonstrated better consistency than those available to go from displacement to force.

Initial attempts to evaluate the impact based bending stiffness from test results did not yield consistent results. Those attempts highlighted that small changes in the curve fitting

technique result in significant changes in the resulting impact based bending stiffness values. The goal of this analysis is to determine possible methods for evaluating the impact based bending stiffness from GAHI testing, evaluate and analyze those methods, and provide a recommended methodology as well as justification.

## **2. Drop Weight Impact Tower (DWIT) Test Data**

### **2.1 Drop Weight Impact Tower (DWIT) Test Data**

It is advantageous to consider methods for computing the impact based bending stiffness with DWIT data as opposed to GAHI test data as DWIT testing is a slower impact event resulting in the availability of more data points. This helps reduce the effects of too few data points when considering a processing method. DWIT test data is also advantageous because of the two sets of data that exist for a single test, one from the load cell and the other from fringe projection.

### **2.2 Load Cell Impact Based Bending Stiffness**

The force displacement curves from the load cell were assumed to be more accurate than those from fringe projection due to the better data resolution and consistency of the results. The force history from the load cell was converted into a displacement history through numerical integration by means of the trapezoidal rule. The impact based bending stiffness values were taken from the linear portion of the loading sequence of the force displacement curves.

### **2.3 Fringe Projection Impact Based Bending Stiffness**

Curve fitting the displacement histories from fringe projection was used to calculate the impact based bending stiffness. Only the data points included up to the peak displacement were

included in the curve fit. This was done as the intent of the study is to extend the methods to GAHI data where a double peak phenomenon occurs and thus only displacement data up to the initial peak are available for curve fitting. Curve fitting was attempted using two types of functions: 1) Polynomials and 2) trigonometric polynomials

Polynomials: Polynomials of third, fourth and fifth degree were fitted to the displacement history from fringe projection using MS Excel and Mathematica. The second derivative of the polynomials was taken to arrive at the acceleration history. The acceleration history was converted to the force history through the multiplication of the impacting mass. Third degree polynomials worked best at depicting a velocity and force history that followed the physical events. Evaluating the derivatives of the fourth and fifth degree polynomials resulted in velocity and force histories that did not accurately represent the physical events.

Trigonometric Polynomials: These functions were of the form

$$P(t) = C + \sum_{n=1}^N A_n \cos\left(\frac{2\pi tn}{m}\right) + \sum_{n=1}^N B_n \sin\left(\frac{2\pi tn}{m}\right) \quad (3.1)$$

Where m refers to the number of intervals in the data set and n refers to the order. Fitting of the test data to functions of the form of Equation 3.1 were performed in Mathematica. For curve fitting with these functions, the force histories from first order (n = 1) fits of the fringe projection displacement histories did not provide sufficient variation in the magnitude of the force compared to the amount seen in the load cell data. For orders greater than 2 (n > 2), the trends of the velocity and force histories did not correspond well with the physical test event. Second order trigonometric polynomials worked best.

Table 17. Impact based bending stiffness (kN/mm) from DWIT Testing.

<b>Specimen</b>	<b>Load Cell</b>	<b>Fringe Projection (3rd Order Polynomial)</b>	<b>Fringe Projection (2nd Order Trigonometric Polynomial)</b>
3 Ply Woven E-glass	0.351	0.240	0.39
5 Ply Woven E-glass	0.879	1.03	1.20
Laminate 1	0.433	0.494	0.71
Laminate 2	0.464	0.551	0.80

From Table 17, the impact based bending stiffness values from the third order polynomial are closer in magnitude to the load cell based impact based bending stiffness values than the second order trigonometric polynomials. Curve fitting through the use of a third order polynomial offers better consistency in calculating the impact based bending stiffness from DWIT data. An observation made from the force displacement plot from fringe projection data is that as a result of the curve fitting, zero displacement does not necessarily correspond with zero force. This notion is contrary to what the physical events dictate for this application and is a result of curve fitting.

### **3. Gas Assisted Horizontal Impactor (GAHI) Test Data**

#### **3.1 Gas Assisted Horizontal Impactor (GAHI) Test Data**

Displacement histories from testing of 5 ply, 12.7 cm (5") specimens at projectile velocities of 50, 65, 80, 95, and 110 m/s were first considered in efforts to calculate the impact based bending stiffness. Impact based bending stiffness values were subsequently calculated for the 3 ply, 7.62 cm (3") and 10 ply, 25.4cm (10") data sets using the method that produced the most realistic force displacement relations from the 5 ply data sets.

### 3.2 Finite Difference

In addition to the curve fitting methods described in relation to DWIT, the impact based bending stiffness was also calculated using the formal definition of the derivative applied to the raw results from fringe projection. For example, the derivative of the displacement points was taken by dividing the change in displacement between points by the time between the points.

Table 18. Velocity, acceleration, and force data calculated using the finite difference method for a 50 m/s impact on a 5 ply specimen.

Time (ms)	Displacement (mm)	Velocity (m/s)	Acceleration (m/s <sup>2</sup> )	Force (kN)
0	0	38.6	-757.9	3.1
0.0114	0.439	30.0	-849.7	3.5
0.0227	0.780	20.4	1564.1	-6.4
0.0341	1.012	38.2	-2401.2	9.9
0.0454	1.445	10.9	1084.4	-4.5
0.0568	1.568	23.2	-1696.4	7.0
0.0681	1.832	3.9	-183.1	0.8
0.0795	1.876	1.8	-18.4	0.1
0.0909	1.897	1.6	-14999.4	61.7
0.1022	1.916	-168.7	14855.0	-61.1

Table 18 shows that the force history significantly changes between positive and negative values as the displacement values consistently increases. This indicates that numerically evaluating the derivative is a poor method to use to calculate the impact based bending stiffness

### 3.3 Curve Fitting

The displacement histories from GAHI testing contain fewer data points than the histories from DWIT. For the initial loading of the specimen during GAHI testing, having fewer than 10 data points is common. One issue with having poor data resolution is that there can be a significant discrepancy between when the first data point indicating deformation was collected and the actual onset of deformation. Consequently, a zero displacement at zero time data point

should logically, not be included in curve fit attempts. The first data point to include in the analysis should be the first data point registering displacement.

### ***3.3.1 Trigonometric Polynomials***

Trigonometric polynomials of first, second and third order were used as curve fitting functions for the initial loading. The second order trigonometric polynomials offered the most realistic curve fits given the segment of the displacement histories considered. However results for the impact based bending stiffness, even for second order trigonometric polynomials, were scattered as seen in Table 19.

Table 19. Impact based bending stiffness (IBBS) values from GAHI test results using curve fit second order trigonometric polynomials.

Projectile Velocity (m/s)	IBBS (kN/mm)
50	1.76
65	5.79
80	2.89
95	Negative Value
110	0.75

### ***3.3.2 Third Order Polynomials***

For the DWIT data previously presented, calculating the impact based bending stiffness by curve fitting third order polynomials to fringe projection data resulted in impact based bending stiffness values that were consistently close to the values resulting from the load cell data. As a result, curve fitting using third order polynomials offers the best chance for consistent and accurate results. Curve fitting the displacement histories from fringe projection is easier to perform on DWIT data sets than on GAHI data sets due to the increased availability of data points from DWIT results. Several methods for curve fitting the GAHI results with a third order polynomial were considered.

From DWIT testing, the acceleration history should be near zero at the onset of loading and gradually increase in absolute magnitude. The acceleration values should be negative assuming the initial velocity is positive as the acceleration is acting in the opposite direction of the velocity upon impact. Often times the polynomial resulting from curve fitting is of a form where its second derivative produces an acceleration history that has a large initial magnitude and decreases as loading continues. This is not what happens physically as illustrated by DWIT test results. The data sampling rate for fringe projection was relatively slow compared to the rate of the impact event. This resulted in only a few points representing the loading phase of the impact. Also, the exact point in time at which the specimen began to experience displacement is difficult to pinpoint. This can be a concern in dynamic testing, but in this case, the potential for concern was elevated into a problem as the data sampling rate relative to the loading rate is poor. As such, a significant and varying amount of displacement can occur in the initial data point between tests. This has an effect on the values of the coefficients of the fitted polynomials. In cases where the initial curve fit is not of the proper form, (a form where the second derivative produces an unrealistic acceleration history) a zero time, zero displacement point was inserted. This most often allowed for a better form of the third order polynomial to be achieved, but at the expense of accuracy. Without the introduction of such a point, the calculated impact based bending stiffness would be a negative value.

### **3.4 Curve Fitting with Third Order Polynomials**

#### ***3.4.1 Method A***

In the systematic consideration of the 5 ply test results, the number of points included in the displacement history curve fit was varied. A third-order polynomial was used in curve fitting. The variation was created by first including all of the points, from an “inserted zero” to

the peak of the displacement history. An “inserted zero” is a data point added to the data set at zero time, zero displacement. The exact location of such a point in time relative to the data points collected that indicate displacement is not known. The inserted point does not necessarily indicate the final point in time prior to deformation. Following the curve fit of the full set of data points, points were subtracted or not included in the curve fit. For each variation, a force displacement curve was generated and the impact based bending stiffness as well as the predicted initial velocity of the plate surface was evaluated.

Table 20. Description of the points included from the displacement histories when generating a curve-fit polynomial.

Set #	Description
1	All points included from induced zero to Peak displacement
2	The inserted zero was not included
3	Inserted zero was not included and one point from the peak displacement end of the data set was not included
4	Inserted zero was not included and two points from the peak displacement end of the data set was not included
5	Inserted zero was not included and three points from the peak displacement end of the data set was not included
6	Inserted zero was included with one point removed from the peak displacement end of the data set
7	Inserted zero was included with two points removed from the peak displacement end of the data set
8	Inserted zero was included with three points removed from the peak displacement end of the data set
9	Inserted zero was included with four points removed from the peak displacement end of the data set

Table 21 shows the initial velocities and the impact based bending stiffness values from the curve fitting methodology applied to raw displacement data from 50, 65, 80, 95 and 110 m/s testing of 5 ply specimens. The displacement history was not regenerated and the raw displacement history was used in the force displacement plots for Method A.

Table 21. Initial velocities ( $V_o$ (m/s)) and the impact based bending stiffness (IBBS(kN/mm)) resulting from curve fitting of the raw displacement histories for 5 ply GAHI tests.

Set #	50 m/s Test		65 m/s Test		80 m/s Test		95 m/s Test		110 m/s Test	
	$V_o$	IBBS	$V_o$	IBBS	$V_o$	IBBS	$V_o$	IBBS	$V_o$	IBBS
1	36.1	0.59	48.96	1.33	40.58	1.63	87.61	-0.61	69.13	0.46
2	32.2	0.91	68.28	-0.20	81.15	-0.31	107.8	-1.35	100.3	-0.67
3	24.9	0.68	57.1	0.85	68.37	0.80	105.8	-1.22	112.38	-1.59
4	21.1	2.76	49.3	2.78	63.8	1.28	112.1	-1.74	142.6	-4.42
5	26.2	1.55	-6.64	16.57	46.81	3.53	118.54	-2.41	204.73	-11.77
6	34.1	1.07	42.7	2.88	29.6	3.08	83.7	-0.2	68.51	0.72
7	34.43	0.32	38.48	4.36	21.6	4.47	87.87	0.048	70.23	0.45
8	38.13	0.61	31.07	8.38	9.71	7.25	77.85	0.79	71.93	0.086
9	36	0.68	39.8	0.2	5.51	8.65	72.1	2.3	50.62	6.45

### 3.4.2 Method B

Another approach to computing the impact based bending stiffness using a curve fitting scheme, is to apply a curve fit to the raw displacement history data and regenerate the displacement history for a test using the same number of points that were produced from the experimental test. The data points included in the curve fit to regenerate the data included the point first indicating deformation to the peak displacement point. The displacement histories were regenerated for all tests and the new data sets were curve fit using the systematic scheme outlined in Table 20 for Method A. The resulting initial velocities and impact based bending stiffness values can be found in Table 22.

Table 22. Initial Velocities ( $V_o$ (m/s)) and the impact based bending stiffness (IBBS(kN/mm)) resulting from curve fitting of curve fit displacement histories for 5 ply GAHI tests.

Set #	50 m/s Test		65 m/s Test		80 m/s Test		95 m/s Test		110 m/s Test	
	$V_o$	IBBS	$V_o$	IBBS	$V_o$	IBBS	$V_o$	IBBS	$V_o$	IBBS
1	36.83	2.05	42.7	2.96	21.61	4.25	78.7	0.24	63	0.87
2	36.1	0.56	57.1	1.4	63.8	1.22	81.9	0.048	68.5	0.64
3	36.1	0.56	57.1	1.4	63.8	1.22	81.9	0.048	68.5	0.64
4	36.1	0.56	57.1	1.4	63.8	1.22	81.9	-0.048	68.5	0.64
5	36.1	0.56	61	0	63.8	1.22	81.9	-0.048	68.5	0.64
6	37	0.447	39.9	4	13.84	5.99	78	-0.2	62.3	0.98
7	37.13	0.1265	36	6	3.86	30.54	77.3	0.54	61.2	1.44
8	37.35	-0.579	31.2	10.8	-9.11	15.5	76.3	0.94	59.8	1.43
9	37.63	0.0089	36.6	0	-26	29.8	75	-1.84	58.2	1.95

### 3.4.3 Method C

While performing the curve-fitting of the raw displacement histories for Method B, it was observed that polynomials of a certain form seemed to produce more plausible results in the form of initial velocities and impact based bending stiffness values. For Method C, the same procedure was followed for Method B with the difference being in the generation of the initial polynomial from the raw data set. The initial polynomial of differing form from the one used for Method B was used to generate the same number of displacement history data points as in the test results. The initial velocities and impact based bending stiffness values were recalculated and are presented in Table 23.

Table 23. Initial velocities ( $V_o$ (m/s)) and the impact based bending stiffness (IBBS(kN/mm)) resulting from curve fitting of curve fit displacement histories for testing conducted with 5ply specimens.

Set #	50 m/s Test		65 m/s Test		80 m/s Test		95 m/s Test		110 m/s Test	
	$V_o$	IBBS	$V_o$	IBBS	$V_o$	IBBS	$V_o$	IBBS	$V_o$	IBBS
1	35.1	0.84	46.9	1.67	29.6	4.23	79	0.28	63	0.71
2	34.43	0.91	48.96	1.49	68.4	0.76	81.9	0.059	68.5	0.71
3	34.43	0.91	48.96	1.49	68.4	0.76	81.9	0.059	68.5	0.71
4	34.43	0.91	48.96	1.49	68.4	0.76	81.9	0.059	68.5	0.71
5	34.43	0.91	48.96	1.49	68.4	0.76	81.9	0.059	68.5	0.71
6	35.19	0.81	46.5	1.77	23	4	78	0.41	62.3	1.04
7	35.3	0.25	46	1.96	14.7	1.95	77.3	0.64	61.2	1.2
8	35.5	0.65	45.42	2.34	-3.91	9.26	76.3	1.1	59.8	1.48
9	35.7	0.45	44.6	3.2	-10	16.1	75	2.15	58.2	2

Review of the data in Tables 21-23 does not demonstrate consistent trends in the impact based bending stiffness values across test velocities for any of the sets considered in curve fitting. The repeated values in sets 2-5 in Tables 22 and 23 are the result of curve fitting curve fit generated data and should not be taken as a sign of data consistency nor validity. Tables 21-23 do indicate that the results produced from attempting to evaluate the impact based bending stiffness values from the available data using the least squares method to generate a third order polynomial should be approached with skepticism.

### 3.5 Consistency with the Application of Curve Fitting (Methods A, B and C)

Data trends in Tables 21, 22, and 23 for the impact based bending stiffness were not as consistent as desired. To investigate the consistency of using a curve fitting method to arrive at the impact based bending stiffness from the available data, multiple tests at two test velocities were considered. Two tests were conducted at 50 m/s and at 65 m/s with 5 ply, 5" diameter specimens. The displacement histories captured using fringe projection for the 50 m/s tests are in Figure 21.

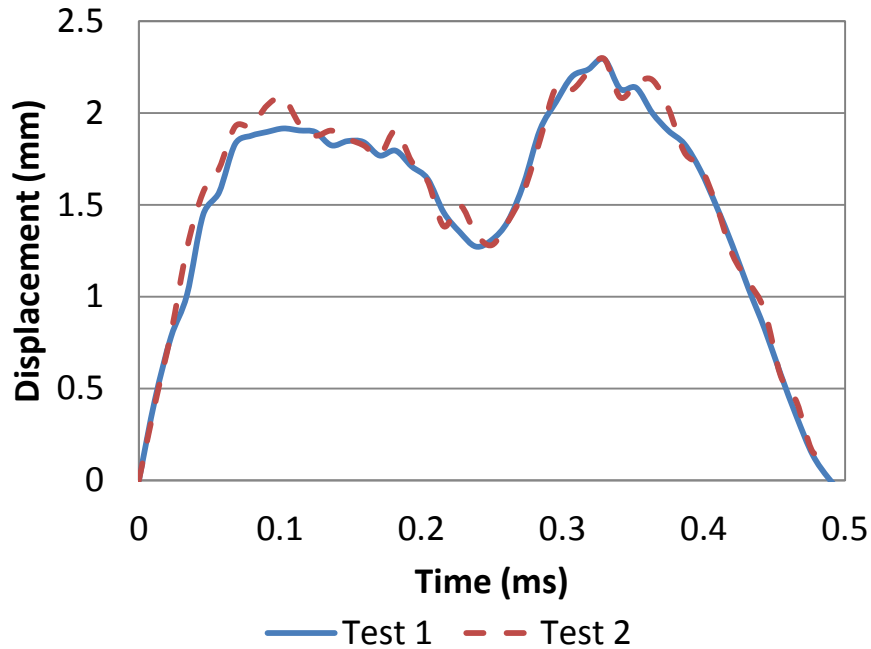


Figure 24. Displacement histories from two GAHI tests at 50 m/s involving the 0.25” projectile and 5 ply specimens.

The percentage difference in the magnitudes at three points in the displacement histories in Figure 24 can be found in Table 24. It should be noted that only data points up to the initial peak (around 0.1 ms) in Figure 21 were included in the curve fitting schemes.

Table 24. Percentage variation in magnitude of select points between Tests 1 and 2 of Figure 24.

Initial Peak	8.39
Trough	0.62
Second Peak	0.093

Methods A and C were applied to the initial loading for the tests in Figure 24 so that the impact based bending stiffness could be evaluated. The results are in Table 25.

Table 25. Impact based bending stiffness (kN/mm) for two 50 m/s impacts of 5 ply specimens.

Set #	Method A		Method C	
	Test 1	Test 2	Test 1	Test 2
1	0.59	-0.27	0.84	1.53
2	0.91	-1.05	0.91	1.53
3	0.68	-0.27	0.91	1.53
4	2.76	0.59	0.91	1.53
5	1.55	-0.21	0.91	1.53
6	1.07	0.22	0.81	1.53
7	0.32	0.47	0.25	1.53
8	0.61	1.56	0.65	1.53
9	0.68	6	0.45	1.53

For method C in Table 25, the closest values for the impact based bending stiffness appear to be 0.91 and 1.53, a difference of 0.62, which is significant in this case, especially considering the 8.39% difference between initial peaks as seen in Table 23. The same analysis was repeated for two tests conducted with a projectile impact velocity of 65 m/s. The results are in Figure 25 and Tables 26 and 27.

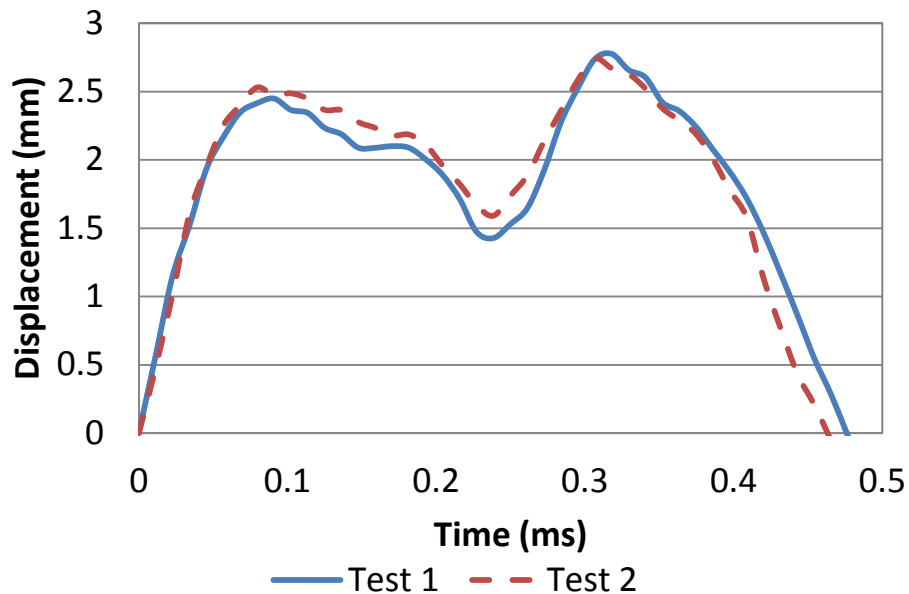


Figure 25. Displacement histories from two GAHI tests at 65 m/s involving the 0.25'' projectile and 5 ply specimens.

Table 26. Percentage variation in magnitude of select points between Tests 1 and 2 of Figure 22.

Initial Peak	4.83
Trough	14.19
Second Peak	1.64

Table 27. Impact based bending stiffness (kN/mm) for two 65 m/s impacts of 5 ply specimens.

Set #	Method A		Method C	
	Test 1	Test 2	Test 1	Test 2
1	1.33	-0.0007	1.67	0.37
2	-0.198	-0.35	1.49	0.33
3	0.845	-0.034	1.49	0.33
4	2.78	-0.48	1.49	0.33
5	16.6	-1.11	1.49	0.33
6	2.88	0.35	1.77	0.39
7	4.36	0.35	1.96	0.43
8	8.38	0.69	2.34	0.51
9	0.2	-1.12	3.2	0.695

For the 65 m/s data (Table 27), ignoring the negative values for the impact based bending stiffness, the smallest difference between the impact based bending stiffness values for each case occur for Method C when considering Set # 1, where the percentage difference between Test 2 and Test 1 is 351%. Considering Figure 25, and the 4.83% difference between initial peaks as shown in Table 26, the differences in the impact based bending stiffness values between Tests 1 and 2 is unreasonable.

### 3.6 Curve Fitting Third Order Polynomials: Method D

A curve fitting scheme very similar to Method C was employed to evaluate the impact based bending stiffness. In order for curve fitting to be successful with third order polynomials, the leading coefficient of the third order term must be negative. This is fundamental for the success of the method. There are two primary differences between Method C and this method. The first is that the form of the third order polynomial had to have a negative coefficient

associated with the third order term and a positive coefficient associated with the first order term (the initial velocity). To achieve a curve fit polynomial of the desired form when regenerating the displacement history when the raw data did not support such a polynomial, a zero time, zero displacement data point was added. The second difference occurs during the regeneration of the displacement history from the curve fit polynomial. Instead of regenerating the data with the same number of data points as the test results, the displacement results were regenerated with 100 points. This results in more data points available for the subsequent force displacement plot that plots the regenerated displacement data against the resulting force data.

Using Method D, the impact based bending stiffness values from experimental tests on 3, 5, and 10 ply specimens impacted at 50, 65, 80, 95, and 110 m/s were calculated. Recall that the acceleration history should increase in the negative direction as the projectile applies a load to the specimen during impact as demonstrated by load cell data from DWIT testing. To accommodate this notion, the third order polynomial from curve fitting the displacement histories needs to have a negative coefficient associated with the third order term. The steps used to calculate the impact based bending stiffness are as follows:

- 1) Identify the onset of loading from the fringe projection displacement history and the peak displacement point of the initial loading.
- 2) Curve fit a third order polynomial to the data set. If the coefficient associated with the third order term is negative, proceed. If the coefficient associated with the third order term is positive, add a zero time, zero displacement data point to the data set (inserted zero) and reattempt the curve fit. In most cases the next curve fitting attempt will create a polynomial of the desired form.

- 3) Regenerate the displacement history using the curve fit derived polynomial over the time interval in question with at least 100 data points.
- 4) Evaluate the second derivative of the displacement history polynomial and convert the acceleration history into the force history with at least 100 data points.
- 5) Plot the force-displacement curve and evaluate the slope of the first 50-60 data points.  
This slope is the impact based bending stiffness value.

Table 28. Impact based bending stiffness values from 3 ply GAHI test specimens.

Projectile Velocity (m/s)	IBBS (kN/mm) Inserted Zero	IBBS (kN/mm) No Inserted Zero
50	0.218	Negative
65	0.067	Negative
80	0.94	Negative
95	0.148	Negative
110	0.598	0.128

Table 29. Impact based bending stiffness values from 5 ply GAHI test specimens.

Projectile Velocity (m/s)	IBBS (kN/mm) Inserted Zero	IBBS (kN/mm) No Inserted Zero
50	0.547	0.875
65	0.359	Negative
80	3.3	0.745
95	0.434	Negative
110	0.65	Negative

Table 30. Impact based bending stiffness values from 10 ply GAHI test specimens.

Projectile Velocity (m/s)	IBBS (kN/mm) Inserted Zero	IBBS (kN/mm) No Inserted Zero
50	2.63	-0.3
65	2.51	-0.15
80	2.074	-0.87
95	3.63	0.34
110	3.70	0.44

Tables 28-30 provide results from the application of Method D. Since the insertion of a zero point adds error into the curve fit, the impact based bending stiffness attained should ideally be more accurate than those with an inserted zero. In many cases, the only non-negative impact based bending stiffness values available are from inserted zero data sets. Consequently the resulting impact based bending stiffness values will be from a mixture of inserted zero and non-inserted zero data sets since the non-inserted data sets are more representative of the test results. Using this logic the impact based bending stiffness values are presented in Table 31.

Table 31. Unscaled Impact based bending stiffness (kN/mm) from GAHI Testing.

Projectile Velocity (m/s)	3 Ply	5 Ply	10 Ply
50	0.218	0.875	2.63
65	0.067	0.359	2.51
80	0.94	0.745	2.074
95	0.148	0.434	0.34
110	0.128	0.65	0.44

The two parameters of interest when considering Table 31 are data consistency and data accuracy. The variation in test results for each specimen size does not follow a pattern and the variation is significant (with significant being >30%). Considering the consistency in overall displacement histories as seen in Figures 24 and 25, the variation in Table 31 does not follow suit. The variation stems from a combination of a low data sampling rate relative to the rate of initial loading and the methodology used to arrive at the impact based bending stiffness from displacement histories.

Evaluating the second parameter, accuracy, of the impact based bending stiffness values in Table 31 is not a precise task. The impact based bending stiffness values from DWIT testing on 3 ply, 7.62 cm (3") diameter specimens could be used as a basis for comparison for the 3 ply, 7.62 cm (3") diameter specimens from GAHI testing, ignoring the potential for strain rate

effects. From Table 17, the DWIT test results indicate the impact based bending stiffness is around 0.35 kN/mm for 3 ply specimens. The 3 ply column in Table 31 places impact based bending stiffness value between 0.067 and 0.218 kN/mm if the 0.94 value is considered an outlier.

An observation made during data evaluation is that the impact based bending stiffness values from curve fitting small data sets can be significantly influenced by the exclusion of data points. Consider the impact based bending stiffness values presented in Figure 23 of 0.434 and 1.39 kN/mm respectively. One of the impact based bending stiffness values comes from a displacement history consisting of all the points up to the peak displacement with an induced zero point and the second impact based bending stiffness value comes from a data set that is the same as the first except that a data point was removed from the initial peak end of the data set. This is not a trivial distinction as the inclusion/exclusion of data points near the peak displacement point can be subjective. It is not uncommon to encounter multiple data points of oscillating magnitude near the initial peak of a given displacement history.

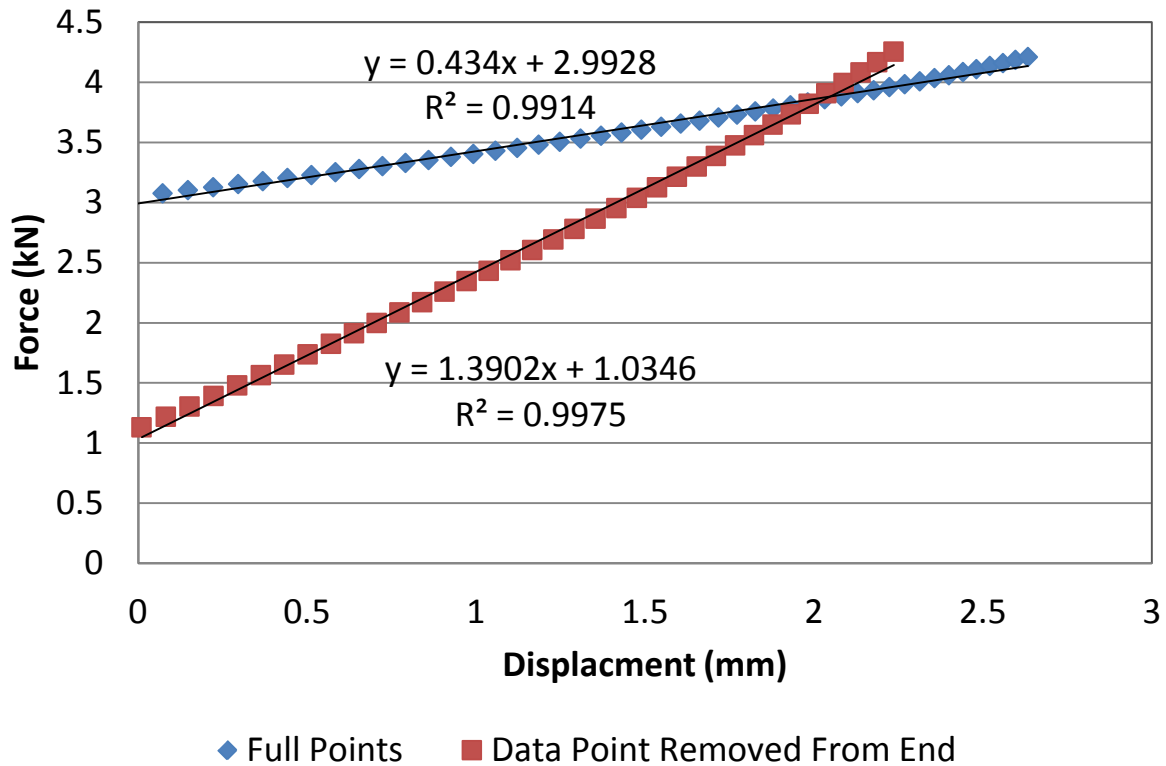


Figure 26. Force displacement relations from Method D for the 95 m/s test case generated from consideration of the “full” initial displacement history and the “full” initial displacement history with a point removed.

#### 4. Conclusion

Impact based bending stiffness values were desired from the displacement histories from the application of fringe projection to the GAHI. From DWIT testing, the acceleration history should increase continuously in negative magnitude assuming a positive impact velocity. With this in mind, curve fitting a third order polynomial to the displacement history region of interest was selected as the best means to calculate the impact based bending stiffness. The procedure outlined for Method D provides a means for generating the necessary force displacement curves. Nevertheless, the calculated values for the impact based bending stiffness from GAHI test results lack the desired consistency.